DATA-DRIVEN BIOMEDICAL ANALYSIS, MODELLING AND VALIDATION

by

Qi Xing

A Dissertation
Submitted to the
Graduate Faculty
of
George Mason University
In Partial fulfillment of
The Requirements for the Degree
of
Doctor of Philosophy
Computer Science

Committee:

_____	Dr. Qi Wei, Dissertation Director
_____	Dr. Jim X. Chen, Committee Member
_____	Dr. Yotam Gingold, Committee Member
_____	Dr. Harry Wechsler, Committee Member
_____	Dr. Sanjeev Setia, Department Chair
_____	Dr. Kenneth S. Ball, Dean, Volgenau School of Engineering

Date: _____ Spring Semester 2019
George Mason University
Fairfax, VA

Data-Driven Biomedical Analysis, Modelling and Validation

A dissertation submitted in partial fulfillment of the requirements for the degree of Doctor of Philosophy at George Mason University

By

Qi Xing
Master of Science
Southwest Jiaotong University, 2007
Bachelor of Engineering
Southwest Jiaotong University, 2004

Director: Dr. Qi Wei, Professor
Department of Department of Computer Science

Spring Semester 2019
George Mason University
Fairfax, VA

Dedication

I dedicate this dissertation to my parents for their unconditional love, encouragement and support. I dedicate this dissertation to my wife, Li, who has been a constant source of encouragement and support during the PhD study and life. You are and always will be my perfect wife and mother to our children. I also dedicate this dissertation to my children, James and Ethan, You have made me stronger, better and more fulfilled than I could have ever imagined. I dedicate this dissertation to all my friends in my life who encourage me and touch my heart.

Acknowledgments

I would like to thank my committee members: Dr. Qi Wei, Dr. Jim X. Chen, Dr. Yotam Gingold and Dr. Harry Wechsler for giving me a lot of insightful comments. In particular, my special thanks to my research advisor, Dr. Qi Wei, whose kind encouragement, patience, advices and believe made this dissertation a possibility. I want to express my gratitude to thank my co-authors: Dr. Parag Chitnis, Dr. Joseph L. Demer, Dr. Jihui Li, Dr. Claudia Vianna Maurer-Morelli, Dr. Nathalia Peixoto, Dr. Seyed Shobeiri MD, Dr. Siddhartha Sikdar Dr. Wilssan Joiner and Dr. Weiwei Zhou for their expert knowledge that went into this dissertation.

Thanks to several undergraduate and graduate students for their support in this process: Victor Huynh, Thales Guimaraes Parolari. I would also like to thank all my friends at GMU for the accompanying and support, including Guilin Liu, Huangxing Wang, Zhonghua Xi, Jianchao Tan, Songrui Liu, Li Liu, Mengbai Xiao, Yue Hao and so on.

Finally, I would like to thank my family for their unbelievable amount of support and love through my PhD journey.

Table of Contents

List of Tables

List of Figures

Abstract

DATA-DRIVEN BIOMEDICAL ANALYSIS, MODELLING AND VALIDATION

Qi Xing, PhD

George Mason University, 2019

Dissertation Director: Dr. Qi Wei

Modern medical imaging techniques including Computed Tomography (CT), Magnetic Resonance Imaging (MRI), Ultrasound (US) and Microscope Imaging provide numerous images containing sufficient information. However, the clinical information is sealed under the pixels, textures and voxels and generally is not easy to be accessed. By integrating clinical observations and experiment data, biomedical image analysis and modeling approach can assist clinical application for disease diagnoses and treatment. The main objective of this dissertation is to develop quantitative tools that can assist clinicians in the diagnosis and treatment of patients. I investigate several computational approaches in addressing five biomedical problems. I make five main contributions through these biomedical problems: 1) Develop an automatic and objective method to segment extraocular muscles from magnetic resonance images and measure extraocular muscles deformation from ultrasound images; 2) Design quantitative method to reconstruct and evaluate 3D human eyeballs; 3) Implement and validate novel method that combines different similarity measurements to optimally register volumetric ultrasound image data containing significant and local anatomical differences. I apply the method on 3D endovaginal ultrasound data acquired from patients during the biopsy procedure of the levator ani muscle; 4) Propose automatic heartbeat

detection method to detect the heartbeat rate from body deformation in low resolution and low frequency video. The method is applied to track the heartbeats of immobilized, ventrally-positioned zebrafish larvae without direct larva heart observation; 5) Present a real time haptic spine surgical simulator that will be used to simulate spine surgeries with the advantages of being interactive, low-cost and representative.

Chapter 1: Introduction

Image-based biomedical modeling and analysis is a multidisciplinary field, which builds on top of knowledge in different areas such as biomedical engineering, computer science, and biology. In the past decades, its techniques and applications have experienced dramatically expansion for solving important clinical problems using medical imaging modalities including Computed Tomography (CT), Magnetic Resonance Imaging (MRI), Ultrasound (US) and Microscope Imaging. In this dissertation, I investigated several computational approaches in addressing five biomedical applications involving medical imaging. The main objective is to develop robust, accurate and quantitative tools that can assist clinicians in the diagnosis and treatment of patients. In the following, I summarize the projects that have been completed.

- The extraocular muscles (EOMs) implement eye movements. Through MRI, it has been found that many forms of binocular alignment (strabismus) are associated with anatomical abnormalities of EOMs [2]. In clinical practice, EOM enlargement is a key quantity to examine in diagnosing several complex strabismus [3] including thyroid eye disease [4, 5]. Therefore, how to reliably and efficiently outline the EOM boundaries from clinical MRI becomes an important practical and research question. Medical image segmentation is the process of semi-automatically or automatically outlining the boundaries of structures of interests in two dimensional (2D) or three-dimensional (3D) image. It is usually the first step in analyzing the anatomical structures from medical images. I develop a method to automatically segment extraocular muscles from MR images, which can help ophthamologists in examining abnormalities of the eye muscles (Chapter 2).

- Extraocular muscle controls the movement of the eye. Examining the extraocular muscle mechanics can help us understand the functions of the extraocular muscles in generating different kinds of eye movement. However, measuring human extraocular muscle mechanics in vivo is challenging for obvious reasons. I propose to use ocular ultrasound imaging to quantify extraocular muscle deformation. Ocular ultrasound is the most common imaging modality used by ophthalmologists to examine ocular anatomy and diseases. Its interactive and rapid imaging capabilities make it suitable to look at eye muscle dynamics. I describe the experimental setup in acquiring high resolution ultrasound images and eye movement data. I also present the results on estimating the extraocular muscle motion. The long-term goal is to examine whether there exists differential movement between the two layers in each rectus muscle. Answer to such question can advance our understanding on the role of the ocular mechanics in the coordination of eye movement (Chapter 2).

- Medical image reconstruction plays an important role in analyzing 3D anatomical structures and building models for biomechanical simulation. I develop a method to reconstruct 3D models of the eyeball from MR images. Several shape descriptors are extracted from these models (Chapter 3). These shape descriptors could be used to correlate with vision acuity of the patients and eye rotation.

- Heterogeneity of echo-texture and lack of sharply delineated tissue boundaries in diagnostic ultrasound images makes three-dimensional (3D) registration challenging, especially when the volumes to be registered are considerably locally different. I implement a novel method that combines different similarity measurements to optimally register volumetric ultrasound image data containing significant and local anatomical differences. Multiple sub-volumes of interest can be selected as target alignment regions with confident consistency. A multi-resolution rigid registration is then performed on these sub-volumes associated with different weights in the cost function. A single region registration is optimized first for a close initial alignment to avoid convergence to a locally optimal solution. I apply the method on 3D endovaginal

ultrasound data acquired from patients during the biopsy procedure of the levator ani muscle. Systematic assessment of the proposed method through cross validation demonstrated the accuracy and robustness of the method. The algorithm can also be applied on medical imaging data of other modalities for which the traditional rigid registration methods would fail (Chapter 4).

- Zebrafish (Danio rerio) is a powerful animal model used in many areas of genetics and disease research. Despite its advantages for cardiac research, the heartbeat pattern of zebrafish larvae under different stress conditions is not well documented quantitatively. Several effective automated heartbeat detection methods have been developed to reduce the workload for larva heartbeat analysis. However, most require complex experimental setups and necessitate direct observation of the larva heart. In this chapter, I propose the Zebrafish Heart Rate Automatic Method (Z-HRAM), which detects and tracks the heartbeats of immobilized, ventrally-positioned zebrafish larvae without direct larva heart observation. Z-HRAM tracks localized larva body deformation that is highly correlated with heart movement. Multi-resolution dense optical flow-based motion tracking and principal component analysis are used to identify heartbeats. Here I present results of Z-HRAM on estimating heart rate from video recordings of seizure-induced larvae, which are of low resolution (1024 x 760) and low frame rate (3 to 4 fps). Heartbeats detected from Z-HRAM are shown to correlate reliably with those determined through corresponding electrocardiogram and manual video inspection (Chapter 5).

- Spine surgeries are high risk operations which require the surgeons to have extensive experiences. For young surgeons, effective and extensive training is critical. This paper presents a real time haptic spine surgical simulator that will be used to train residents, fellows and spine surgeons in a hospital training program. It provides a realistic environment for the trainees to practice spine surgeries and has the advantages of being interactive, low-cost, representative, and repeatable over conventional training

approaches. Haptic Phantom offers the users force feedback, differentiating the proposed system from other screen-based training systems. Computational efficiency was achieved by developing advanced graphical rendering methods. The volumetric data was classified into surface voxel cloud and inner voxel cloud by the adjacency graph which stored the relationship among voxels. To speed up the collision detection and real time rendering between the virtual surgical tools and the lumbar model, Octree-based algorithms and GPU technique were applied. To enhance the physical realism, three dimensional lumbar vertebrae models were reconstructed from CT images and associated with non-homogeneous bone density such that the rendered model best represents the spine anatomy and mechanics (Chapter 6).

Chapter 2: Extraocular Muscles Segmentation and Deformation Measurement

The work presented in this chapter has been published in [6, 7].

2.1 Extraocular Muscles Segmentation

2.1.1 Introduction

The extraocular muscles (EOMs) or eye muscles control movement of eye. Through Magnetic Resonance Imaging (MRI) studies, it has been found that many vision deficits are associated with anatomical abnormalities of EOMs [2]. In clinical practice, eye muscle enlargement is a key quantity to examine in diagnosing several vision disorders [3] and thyroid eye disease [4, 5]. Therefore, how to reliably and efficiently outline the EOM boundaries from clinical medical images becomes an important research question. In clinical studies, ophthalmologists usually segment EOM boundaries manually [2, 8, 9], which were labor expensive and may introduce user dependent artifacts.

Several computer-aided semi-automatic [10–12] and automatic segmentation [13, 14] methods have been developed. They provided an more efficient quantitative analysis of EOM anatomy. However, all of these methods used image pixels as the underlying representation primitive. It is known that pixels are not the most natural representation of visual scenes, since they do not take into account the local patterns among the neighboring pixels and are subjected to noise. It would be more natural and more efficient to process the image with perceptually meaningful patches that contains many pixels which share similar features.

I propose a fully automatic eye muscle segmentation method based on superpixel, region adjacency graph and Normalized Cut while integrating the prior information of shapes. Rather than using the pixel-level image processing techniques, the approach builds upon local feature of the extraocular muscles. I consider small image patches obtained from superpixel over-segmentation [15–18] as the basic unit of any further image processing procedures, such as filtering, detection and segmentation. I show that by building region adjacency graph of the superpixels, I can develop a robust method to outline the eye socket boundary and the EOMs within. The performance of the proposed automatic segmentation method was evaluated by comparing the proposed results to manual segmentation which showed high accuracy.

2.1.2 Related Work

Firbank et al. [11] have shown that it is feasible to segment the EOMs using the active contours. An energy function was minimized and updated for an outline at each iteration. Computed boundary in one slice can be used to search the next image in spatial dimensions. However, this approach is sensitive to the initial boundary, since it can be easily trapped in the local minima [19]. The accuracy is influenced by the convergence criteria — higher accuracy requires tighter convergence criteria and longer computation time [20]. Souza et al. proposed a mathematical morphology method to semi-automatically segment EOMs [21, 22]. They performed an iterative grayscale closing operations to segment the orbital wall which was then used as the region of interest. The EOMs were outlined in the region of interest through Laplacian of Gaussian detector and opening operations. However, the size of flat disk used for the morphology operation was fixed and only worked on pixel level. The number of iterations had to be carefully supervised. A more recent semi-automatic approach deformed 3D geometric template models of the EOMs to the MR images of individual patients [23]. Image features of the extraocular muscles were detected and filtered to guide fitting of the generic anatomical template. However, the template model has to be built by considering the prior knowledge of topology of the EOMs. In

addition, a global registration between the image sequence and the template model had to be performed at the beginning. To overcome the limitations of existing approaches on EOM segmentation, I develop a novel method to automatically segment the muscle boundaries through superpixel, region adjacency graph and Normalized Cut scheme. The proposed method doesn't require interactively initialize an outline.

2.1.3 Method

Superpixel Over-segmentation

The image segmentation algorithm Superpixel [16] groups pixels with coherent intensities and spatial locations into patches of pixels. These superpixels provide a high level representation of the original image which can be used for further processing. The geometric shapes of superpixels are not restricted to rectangular. Such flexibility enables representation of features more naturally by maintaining the boundaries of the objects in the image. Accurate segmentation can then be performed by merging the local superpixels which have similar features.

I applied the k-means algorithm to group nearby pixels into superpixels in uniform sizes [15]. Unlike other superpixellization methods [24, 25], the k-means method produces a more regularized grid of superpixels, which is important for building the region adjacency graph. Fig. 2.1(a) shows a T-1 weighted quasi-coronal MRI image perpendicular to the long axis of the orbit with 256 micron pixels and 2 mm plane thickness. Fig. 2.1(b) illustrates the result of the superpixel over-segmentation. The boundaries of the superpixels preserve the true structure boundaries. More importantly, the shape and area characteristics of the EOMs and the eye socket are relatively consistent [12]. As the algorithm restricts, the number of pixels in each superpixel is nearly constant across the image.

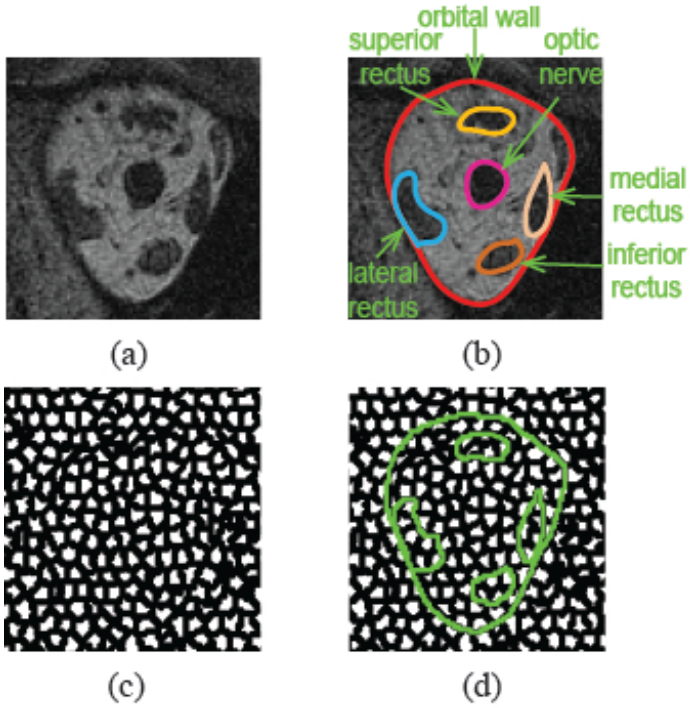

Figure 2.1: EOM anatomy in MR imaging and superpixel. (a) A representative coronal MRI image of the eyeball and EOMs; (b) Labeled ocular structures to segment, including orbital wall (red), superior rectus muscle (orange), lateral rectus muscle (sky blue), inferior rectus muscle (bright yellow), medial rectus muscle (pink), optic nerve (purple); (c) Superpixel over-segmentation; (d) Manually segmented structured overlaid on the superpixels.

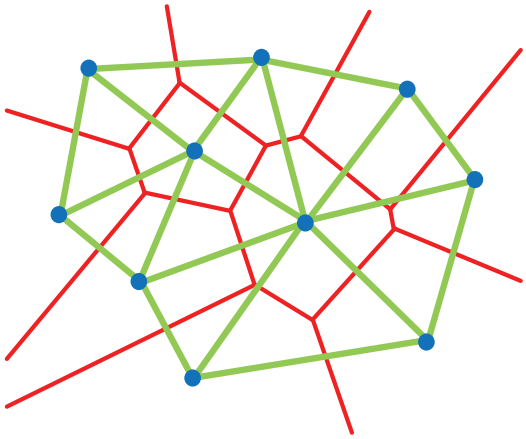

Figure 2.2: Region adjacency graph build from superpixels.

Region Adjacency Graph Construction

Human visual perception is good at recognizing individual objects even with varying intensities or textures. As an algorithm with no priors, superpixel segmentation algorithms [15, 16, 26, 27] have the tendency to over-segment the image (Fig. 2.1(c)(d)). Region adjacency graph (RAG) is a data structure common for many segmentation algorithms [28]. I used RAG to specify spatial connection of neighboring superpixels. Each superpixel was defined as a node in a graph (Fig. 2.2). Each superpixel was connected through the edges to all its neighbors. The RAG was used to merge adjacent regions provided that these regions have similar intensity distributions. Denote n_i to be a node in RAG with mean intensity I_i and n_j to be one of its neighbors. The edge weight between n_i and n_j is defined as $w_{ij} = \exp\big(\frac{-\|I_\mathrm{i}-I_\mathrm{j}\|^2}{\sigma^2}\big)$, where σ^2 is overall image variance. w_{ij} measures the intensity similarity between n_i and n_j.

Normalized Cuts Segmentation

Superpixel segmentation is a bottom-up approach as it merges individual pixels together. Once I have the superpixels represented by the RAG, I applied the Normalized Cuts algorithm (Ncut) [29], a top-down approach to partition the graph recursively until finding the ocular structures. Applying the Normalized Cuts on superpixels other than pixels is more robust to image noise. In addition, it has an obvious advantage of being computationally efficient, as the size of the affinity matrix and the complexity of the RAG employed for image representation are significantly reduced.

In each division, the Ncut algorithm optimally divides one region into two subregions N_1 and N_2 by removing edges connecting them in RAG:

$$Ncut(N_1, N_2) = \frac{cut(N_1, N_2)}{assoc(N_1, N)} + \frac{cut(N_1, N_2)}{assoc(N_2, N)}. \tag{2.1}$$

$cut(N_1, N_2) = \sum_{n_i \in N_1 \& n_j \in N_2} w_{ij}$ computes the degree of dissimilarity between N_1 and

N_2 as summed weight of all the removed edges. $assoc(N_1, N)$ defines the total edge weight from nodes in N_1 to all nodes in the current region.

Figure 2.3: Normalized Cuts segmentation produced regions labeled in different gray scales.

Fig. 2.3 shows the segmentation results after applying Normalized Cuts. The final nodes after Normalized Cuts contain many superpixels and are colored in grayscale. The Normalized Cuts segmentation can successfully highlight some of the ocular structures such as the superior rectus muscle, the oblique rectus muscle and the optic nerve. However, the lateral and medial rectus muscles had incomplete boundaries and their boundaries are connected with the orbital wall, making them difficult to segment. Further automatic operations are needed to solve discontinuity issues and label each structure.

Orbital Wall and Extraocular Muscle Segmentation

Segmenting the orbital wall was studied previously. Souza et al. [12] applied an iterative grayscale mathematical morphology operation to segment the orbits. But their method required the user to specify a flat disk template and number of recursive iterations of erosions. Firbank et al. [11] manually outlined the boundary around the eye socket. I proposed an automatic method to extract the orbital wall with shape prior knowledge. The Laplacian of the Gaussian [30] and connected components labeling methods are applied to detect the connected boundaries of the orbital wall, rectus muscles and optic nerve from

the segmented Normalized Cuts image shown in Fig. 2.4(a).

To extract the orbital wall, I considered the prior knowledge that the eye socket was always located near the image center. The center of each region produced by Normalized Cuts was calculated and shown in Fig. 2.4(b). The centers of the optic nerve and the orbital wall were the two closest centers near the image center. Using the k-nearest algorithm, the regions of the optic nerve and the orbital wall can be identified from the boundary map. Any region outside the orbital wall were removed (Fig. 2.4(c)). Two of the closed boundaries inside the orbital wall were identified as the superior and inferior rectus muscles (Fig. 2.4(c)). To segment the lateral rectus muscle and medial rectus muscle with incomplete boundaries, the convex hull around the orbital wall was calculated and shown as the red closed curve in Fig. 2.4(d). The generated closed orbital wall completed the initial discontinuous boundaries of the lateral and medial rectus muscles which are in contact with the orbital wall. The convex hull served as the region of interests and reserves the natural boundary of the eye socket in the original image (Fig. 2.4(e)) and the superpxiel image (Fig. 2.4(f)). Finally, image region and hole filling algorithms were used to complete the EOM segmentation (Fig. 2.5(a)). Fig. 2.5(b) shows the segmented boundaries overlaid with the MRI and superpixel images.

2.1.4 Experiments and Results

Materials

The T1-weighted MRI images of both eyes were acquired from 5 health subjects and provided by Dr. Joseph Demer at UCLA. Eight coronal images at the slice thickness of 2mm for each eye were segmented. All images were digitized with 256×256 pixels and 16 bits gray-level of resolution at voxel size of 0.3mm×0.3mm ×2.0mm. I asked two operators to independently and manually trace the ocular structure boundaries, which were used as ground truth for accuracy assessment.

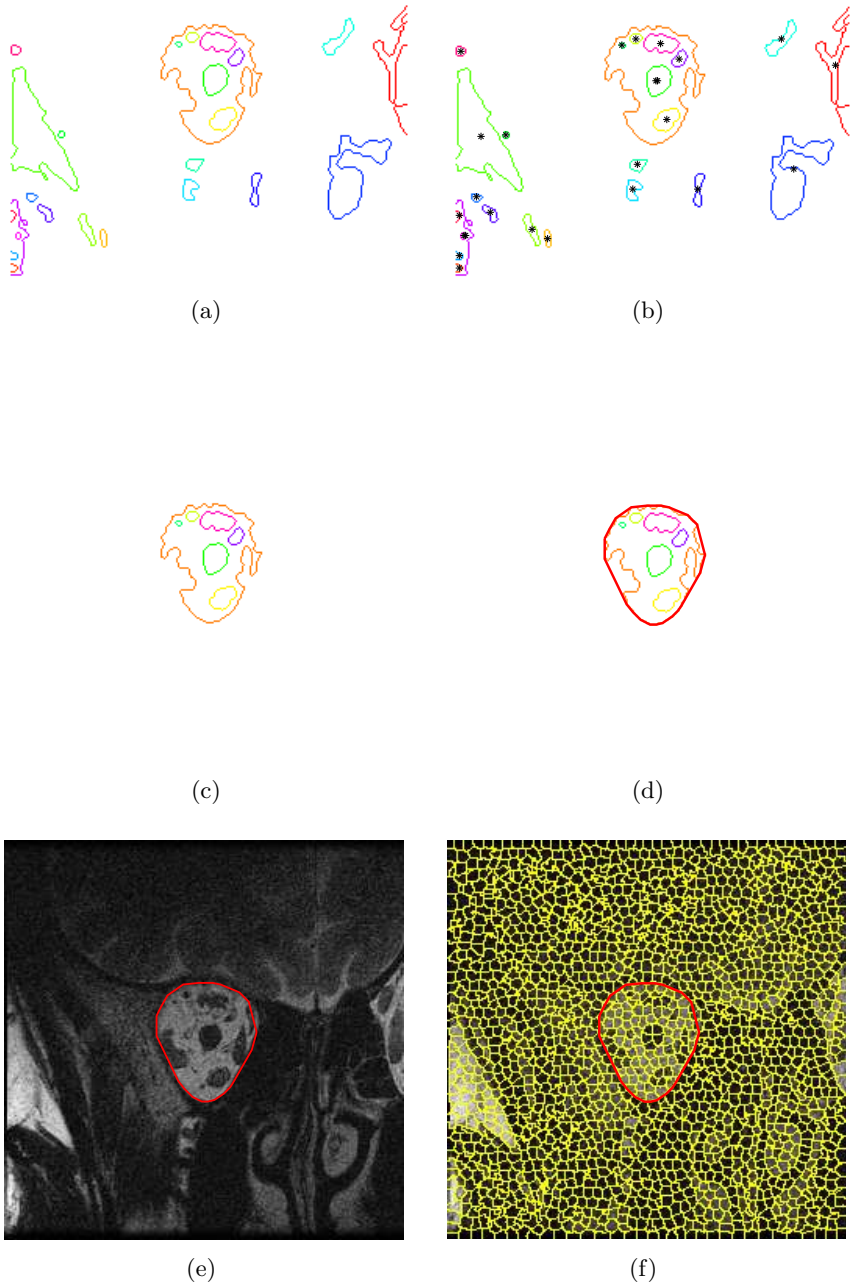

Figure 2.4: Region of interest extraction. (a) Initial boundaries after Ncuts based on Fig. 2.3; (b) Center(*) of each boundary (c) Finding optical never and orbit regions using k-mean cluster; (d) Orbit and EOMs boundaries identified using convex hull; (e) Region of interest in the original image; (f) Region of interest in the superpixel image

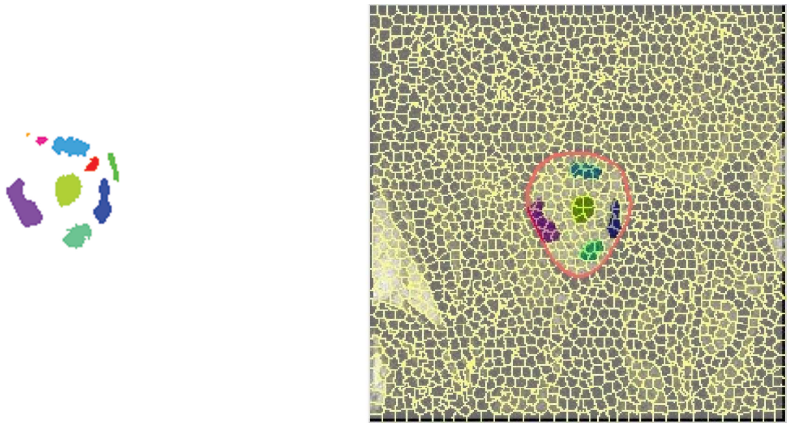

(a) (b)

Figure 2.5: EOM segmentation. (a) Segmented extraocular muscles and optic nerve; (b) Superpixels mapped with the orbital wall and the segmented ocular structures.

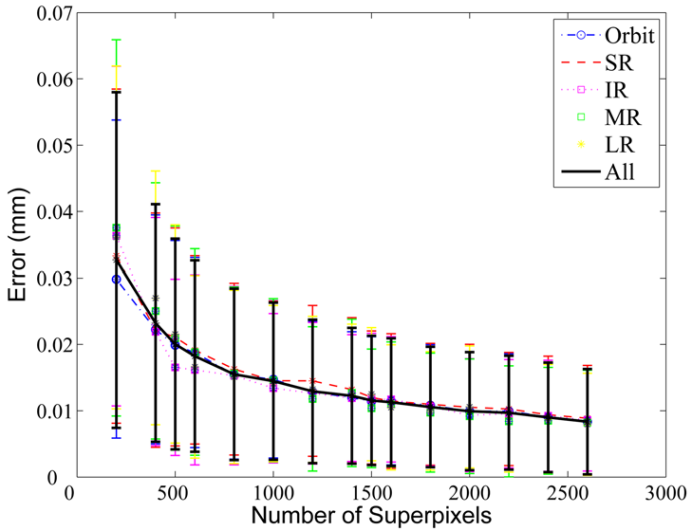

Figure 2.6: The shape error between the manually segmented boundaries and the superpixel over-segmented boundaries decreases as the number of superpixels n increases for orbit, superior rectus(SR), inferior rectus(IR), medial rectus(MR), lateral rectus(LR) and all four rectus(All) muscles

Shape Error Analysis

One critical issue is to determine the number of superpixels n when applying the k-means algorithm. If there are too few superpixels, I may miss out important structures. On the other hand, if there are too many, I lose the superpixel's advantage of being representative, robust and efficient. In order to determine an appropriate n, parameter learning was performed by analyzing the influence of n on the segmentation accuracy. I first manually segmented one set of MRI images by tracing the boundaries of the ocular structures. I applied superpixel over-segmentation on the same set of images while varying $200 < n < 2600$. For each n, I overlapped the manually traced boundaries to the superpixel image (Fig. 2.1(c)(d)). The shape error between the manual and the superpixel segmentations was computed using the boundary-based measurement [16] to quantify how close the superpixel boundaries are to the manual segmentation (approximating ground truth). The shape error was calculated as the mean absolute distance between the superpixel boundaries and the ground truth boundaries. Fig. 2.6 plots the shape error as a function of n for different ocular structures. Unsurprisingly, as the number of superpixels increases, the error drops monotonically to zero when each pixel becomes one superpixel. According to "elbow selection criterion" [31, 32], $n = 1800$ was chosen as the number of superpixels for the MRI dataset in subsequent operations.

Performance Evaluation

Area-based metric [12] and volume-based metric [10, 11] are commonly used to evaluate the accuracy of image segmentation. One drawback is that these two metrics do not consider the overlap between ground truth and computer generated segmentation results. I decided to use the region-based metrics to assess the proposed approach: Variation of Information (VI) [33], Probabilistic Rand Index (RI) [34] and Segmentation Covering Criteria (Covering) [35].

Variation of Information The Variation of Information metric was introduced for the purpose of clustering comparison [33]. It measures the distance between two segmentations in terms of their average conditional entropy defined as

$$VI(S, S') = H(S) + H(S) - 2I(S, S'), \tag{2.2}$$

where H and I represent the entropies and mutual information between two clusters of data S and S'.

Rand Index Rand Index [34] was first proposed for general clustering evaluation. It operates by comparing the compatibility of assignments between pairs of elements in the clusters. The Rand Index between the automatical segmentation and the manual segmentation X and G is given by summing the number of pairs of pixels that have the same label in $X \bigcup G$ and those with different labels in both segmentations, divided by the total number of pairs of pixels.

Segmentation Covering I define the covering of segmentation S by segmentation S' as

$$C(S' \rightarrow S) = 1/N * \sum_{R \in S} |R| * max_{R' \in S'} O(R, R'), \tag{2.3}$$

where N is the total number of pixels in the image and $O(R, R') = \frac{|R \cap R'|}{|R \cup R'|}$ is the overlap between two regions R and R' [35].

Table 2.1 summarized evaluation results using the region-based metrics. The IR, LR, MR and SR muscles of both left and right eyes were analyzed. I computed two scores for the Segmentation Covering for EOMs, which were segmentations at a optimal data set scale(ODS) and a optimal image sacle(OIS). I also examined the Rand Index and Variation of Information quantities compared to the manual segmentation. Lower value of Variation of Information metric indicates greater similarity. The average Variation of Information value

Table 2.1: Computational time (in seconds) of applying three collision detection methods

		VI		**RI**		**Covering**	
		ODS	OIS	ODS	OIS	ODS	OIS
Left	IR	1.25	1.13	0.78	0.81	0.75	0.78
	LR	1.47	1.25	0.81	0.84	0.78	0.82
	MR	1.45	1.35	0.75	0.78	0.72	0.79
	SR	1.86	1.65	0.82	0.83	0.81	0.85
Right	IR	1.75	1.67	0.81	0.84	0.71	0.81
	LR	1.65	1.47	0.85	0.86	0.78	0.83
	MR	1.87	1.58	0.84	0.87	0.73	0.78
	SR	1.47	1.25	0.79	0.82	0.76	0.84

is 1.51 which outperforms other image segmentation outcomes [36]. Rand Index metric is in the range [0 1]. Higher value indicates greater similarity between two segmentations. For different EOMs, The average value for Rand Index metric is greater than 0.82 which shows the excellent performance of the proposed algorithm. The standard deviation of Rand Index is about 0.03 demonstrating that the proposed method can generate consistent results for four different EOMs. With respect to Segmentation Covering, I compute the normalized overlap score in range [0 1]. The larger the value, the more accurate the algorithm. The average value for different EOMs is 0.78, which is consistent to Rand Index result. In summary, as Table 2.1 shows, the proposed automatic segmentation algorithm was able to segment boundaries fairly close to the manual segmented boundaries which illustrates the accuracy and effectiveness of the proposed approach.

2.1.5 Conclusion and Future Work

Extraocular muscles segmentation from MRI is an important and challenging task for clinical diagnosis. This study has demonstrated an automatic method using Superpixel, Region Adjacency Graph and Normalized Cuts. The results were compared to manual segmentations. Region-based segmentation evaluation metrics showed that the proposed method was able to segment boundaries fairly accurately.

Normalized Cuts is most time consuming process, I would like to improve the the efficiency of segmentation on superpixels using Normalized Cuts by using GPU to accelerate the Normalized Cuts. Alternatively, I could employ other more efficient graph cut algorithms to segmentation the images. To improve the reliability for the optic nerve identification, I could consider the shape prior of the optic nerve and locate it by using circle fitting method on the segmented shapes. The method could be applied to automatically reconstruct 3D patient-specific EOM models which will be used in clinical diagnosis and surgical planning.

2.2 Extraocular Muscles Deformation Measurement

2.2.1 Introduction

Examining the extraocular muscle mechanics can help us understand the functions of the extraocular muscles in generating different kinds of eye movement. However, measuring human extraocular muscle mechanics in vivo is challenging for obvious reasons. Medical imaging provides a non-invasive approach to study extraocular muscle kinematics during eye movement. Previously tagged MRI was used to track motion of the horizontal rectus muscles during smooth pursuit eye movement [37–39]. I propose to use ultrasound imaging as an alternative modality to quantify extraocular muscle deformation. Ocular ultrasound is the most common imaging modality used by ophthalmologists to examine ocular anatomy and diseases. Its interactive and rapid imaging capabilities make it suitable to look at eye muscle dynamics. I design and develop dynamic extraocular muscle analysis framework in acquiring high resolution ultrasound images and eye movement data. I also present results on estimating the extraocular muscle motion. The long term goal is to examine whether there exists differential movement between the two layers in each rectus muscle [40]. Answer to such question can advance our understanding on the role of the ocular mechanics in the coordination of eye movement.

2.2.2 Material and Method

Ultrasound images of the eye during smooth pursuit eye movement were collected together with eye movement data from an eye tracker. The data acquisition procedure was reviewed and approved by the institutional review board (IRB) of George Mason University. Ultrasound images were then processed offline to calculate the extraocular muscle deformation.

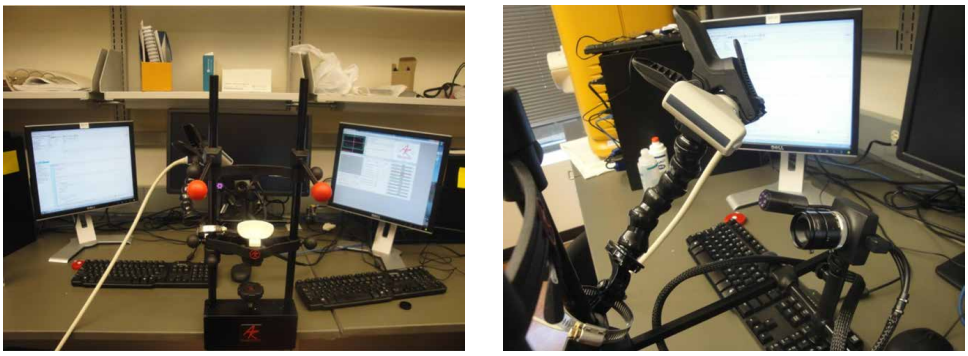

(a) (b)

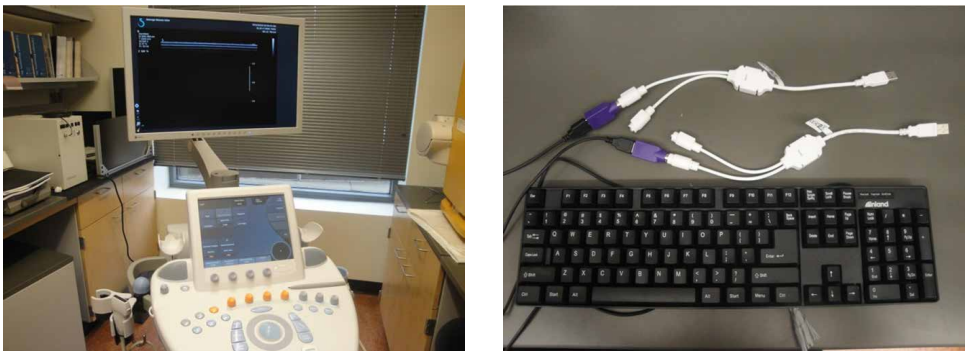

(c) (d)

Figure 2.7: System setup and configuration. (a) Setup for a subject to perform head-fixed, visually-guided smooth pursuit eye movement; (b) The ultrasound probe was clamped for acquiring stable images; (c) The ultrasound imaging system used to collect data; (d) Double cabled keyboard to synchronize the ultrasound system and the eye tracker

The subject was asked to sit up right on a chair with the head fixed by chinrest and forehead support (Fig. 2.7(a)). The subject was then asked to use one eye to track a moving target on a screen. A green circle stimulus with horizontal movement amplitude of 40 degrees in 2 seconds was presented on a black background to guide sinusoidal smooth pursuit eye movement (Fig. 2.7(a)). Presentation system (Neurobehavioral Systems Inc.) was used to display the stimulus on the monitor with resolution 1024 x 768 and frequency 75 Hz. An eye tracking system (Arrington Research) was used to track the eye position at 220 Hz (Fig. 2.7(b)). The other eye was closed with an ultrasound probe placed gently against the

front of the eye. B-mode ultrasound images (Aixplorer, Supersonic Imagine) were acquired during eye movement at 60 Hz (Fig. 2.7(c)). The eye tracking system and the ultrasound imaging system were synchronized through a keyboard trigger setup (Fig. 2.7(d)). In this pilot study, I examined the lateral rectus muscle deformation during a 10 second smooth pursuit eye movement guided by the sinusoidal visual stimulus. In order to identify local features and estimate muscle deformation, the SIFT algorithm was used to detect the correspondent local features [41]. The SIFT descriptor detects points of interests with invariance to scale, rotation and translation. The correspondences of paired features were determined by comparing the distance between the two paired descriptors. Those features that can be tracked continuously in most of the frames were identified manually for further analysis. Automatic feature selection approaches are being researched.

2.2.3 Result

Fig. 2.8 shows the representative B-model ultrasound images (pixel resolution of 0.53 mm) in different gazes. The EOM image (Fig. 2.8(d)) is extracted from whole image (Fig. 2.8(b)) as region of interest (ROI) for post-processing. Fig. 2.9 shows ultrasound images in ROI at multiple different eye positions. Contraction and elongation of the lateral rectus muscle were clearly seen. The SIFT features detected in yellow. One of the corresponding features detected in the continous time frame was overdisplaid in green which showed local muscle motion to the up right direction along the muscle long axis. A displacement vector can be determined from the center locations of this feature in mutiple successive frames. Given the frequency of the ultrasound image acquisition, muscle velocity at this local feature can be computed. sinusoidal smooth pursuit eye movemen Fig. 2.10 demonstrated muscle velocity (green) at detected feature (green in Fig. 2.9). The stimulus (red) did a sinusoidal smooth pursuit movement in horizontal direction in period of 2s. The eyeball velocity (blue) is tracked and calculated through eye tracking. The data showed that at this specific location the muscle deformed at a lower velocity than the eyeball velocity, consistent with previous studies using dynamic MRI which demonstrated the nonuniform contraction of skeletal

muscles [42].

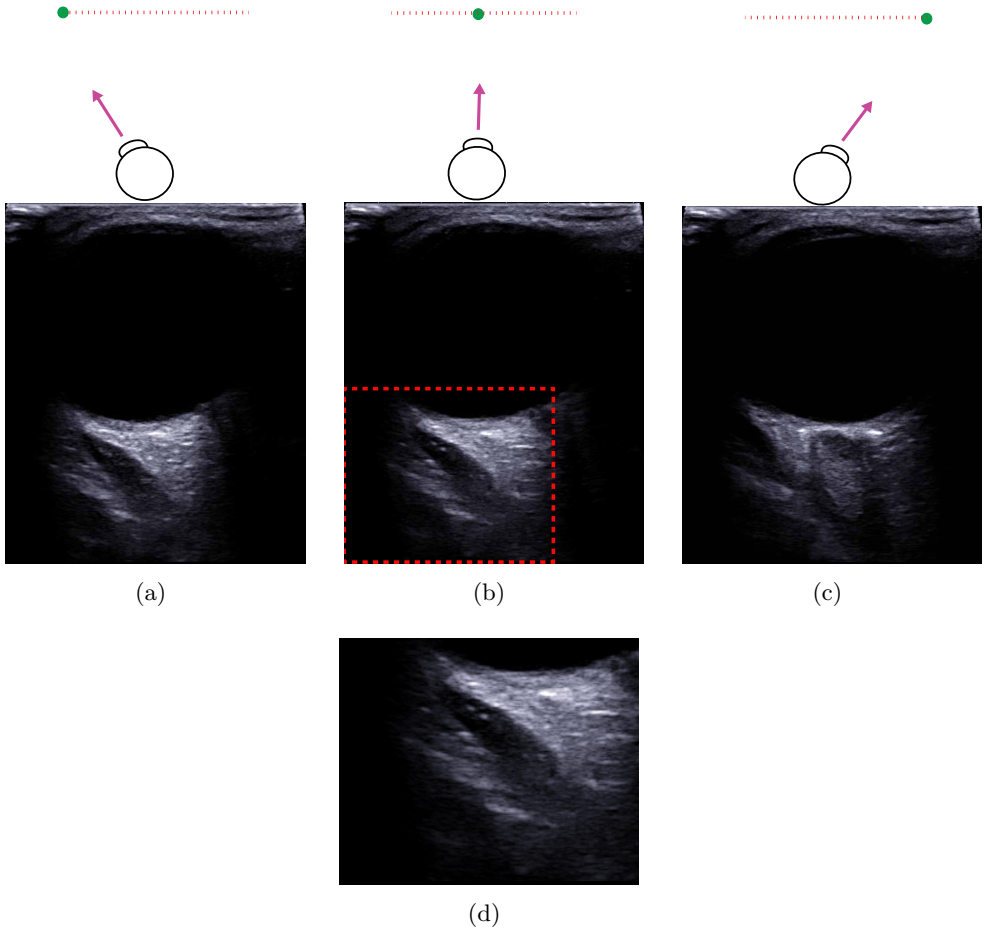

Figure 2.8: Ultrasound image of the eyeball and lateral rectus muscle different gazes. The ROI of lateral rectus muscle (d) is extracted from whole image (b). Lateral rectus muscle moves to control horizontal eyeball movement from left (a) to right (c)

2.2.4 Conclusion and Future Work

The analysis demonstrated the feasibility of using ultrasound imaging to study the extraocular muscle deformation in vivo. One lesson I learned is the sensitivity of the detectable features to the imaging parameters and the imaging plane location which need to be systematically examined. To improve the accuracy and robust, I need to locate a optimal imaging plane during the data collection, and thus the best feature could be easily identified and

tracked. Moreover, I will develop mesh-based deformation tracking algorithm to quantify muscle deformation at various locations. I would like to collect more data from normal subjects in different eye motion pattern to analyze the two layers biomechanical functions for each extraocular muscle.

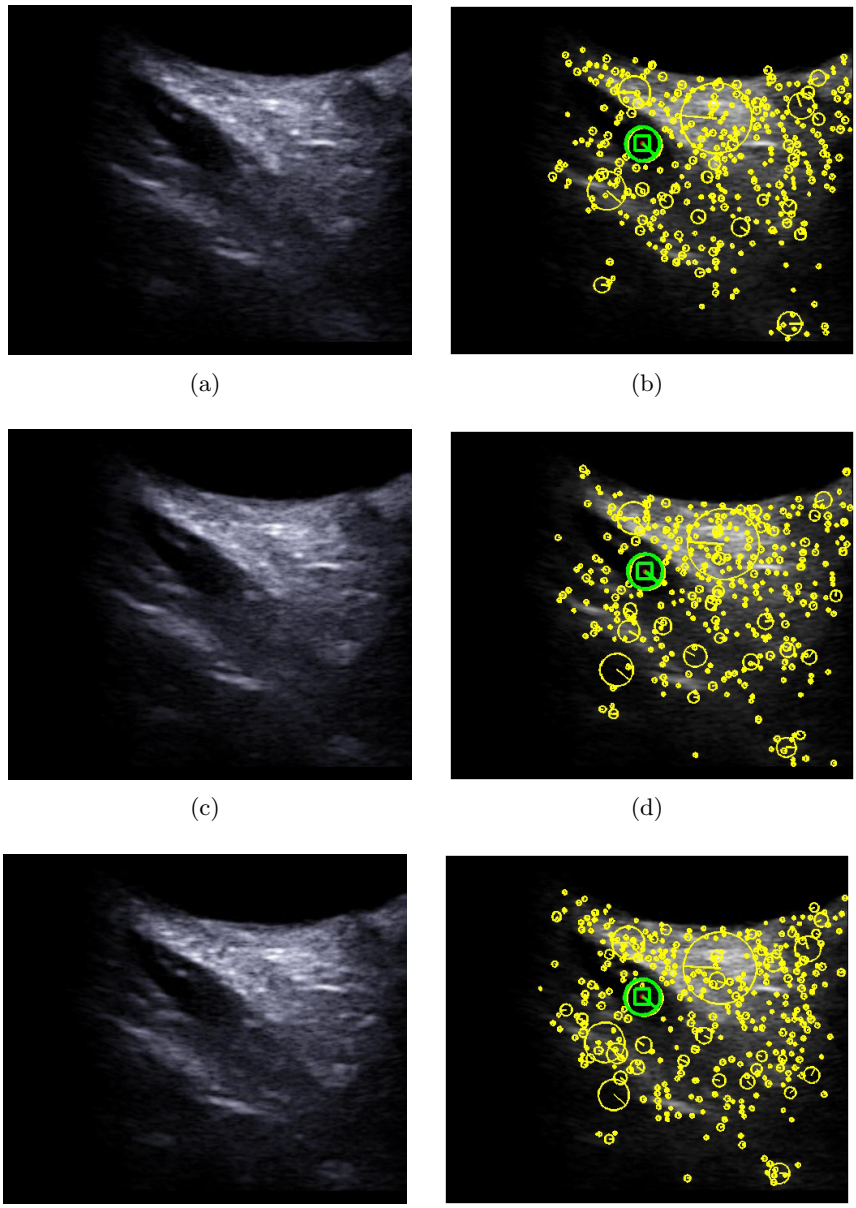

Figure 2.9: Ultrasound image of the lateral rectus muscle in multiple frames. Left - raw image; Right - motion tracking through SIFT feature, One of the corresponding features detected in the continous time frame was overdisplaid in green which showed local muscle motion to the up right direction along the muscle long axis

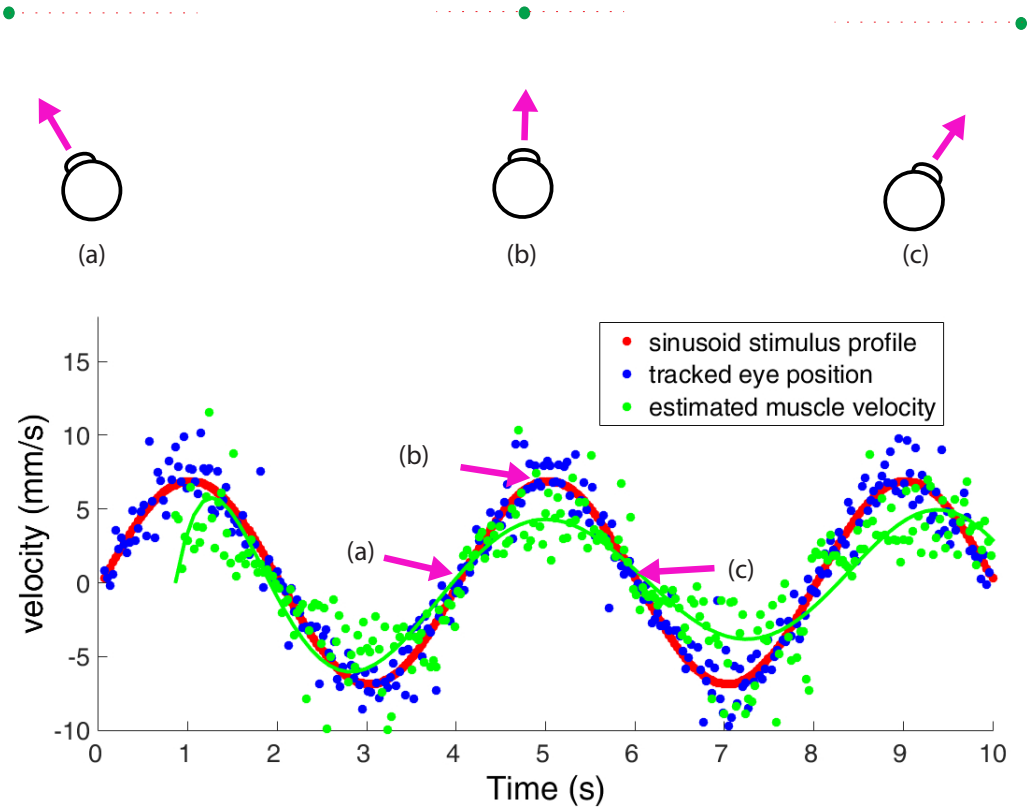

Figure 2.10: Preliminary results on the estimated muscle velocity by tracking one feature point. The red curve was the sinusoidal smooth pursuit stimulus. The blue dots were the tracked eye velocities. The green dots were the estimated muscle velocity in every frame and the green curve was the fitted polynomial curve. Within 2s period, the velocity lateral rectus muscle initialized with 0 mm/s at gaze direction (a), reached maximum speed at gaze position (b), then reduced to 0 mm/s at gaze position (c). The large discrepancy at the beginning of the movement was because the first second of images were missing.

Chapter 3: Human Eyeball Model Reconstruction and Quantitative Analysis

The work presented in this chapter has been published in [43].

3.1 Introduction

Eyeball size and geometric features provide valuable information on certain type of vision disorders. For instance, positive correlation between the axial length of the eyeball and the degree of myopia has been found through quantitative analysis [44, 45]. Various eyeball geometric characteristics have been represented by different methods in both two dimensions (2D) [46–48] and more recently in three dimensions (3D) [49–51]. Previous analysis required manual effort on image processing and model reconstruction, which were labor expensive and may introduce user dependent artifacts. In addition, there are many other clinically important questions regarding the eyeball surface features that have not been investigated, such as the statistical variations of the eye shape of a large population and the possible gaze-dependent eye shape changes of normal subjects. These questions demand accurate, robust and efficient computational algorithms to build 3D models from medical images.

To address the limitation of existing approaches that measure the geometric characteristics of eyeball, I develop a new method to reconstruct detailed 3D models of the eyeballs from T2-weighted MR images. The goal is that this automatic modeling framework can be used on analyzing large datasets and generalized to data with different kinds of pathologies. The generated models can help to understand scientific questions such as whether eyeball deforms as a function of gaze and assist clinicians for diagnosis.

Parametric geometric representation is used, which has the advantage of continuity and

smoothness. I propose to characterize eyeball shape by ten characteristic metrics. The reconstruction approach and quantitative methods will be useful for eye disease diagnosis benefiting by the accurate eyeball shape representation and comprehensive description by the ten metrics.

3.2 Related Work

Previous studies have used MRI to quantify the size and shape of eyeball. Curvatures of the retinal surfaces were analyzed, and 3D eyeball models were built [50, 51]. Firbank et al. [11] showed the feasibility to segment EOMs using the active contours. However, this approach is sensitive to the boundary initialization, since it can be easily trapped in local minima [19]. In addition, the accuracy is influenced by the convergence criteria — higher accuracy requires tighter convergence criteria and longer computation time [20]. Souza et al. proposed a mathematical morphology method to semi-automatically segment EOMs [12,22]. They performed an iterative grayscale closing operations to segment the orbital wall which was then used as the region of interest. The EOMs were outlined in the region of interest through Laplacian or Gaussian detector and opening operations. However, the size of flat disk used for the morphology operation was fixed and only worked on the pixel level. The number of iterations had to be carefully supervised. A more recent semi-automatic approach deformed 3D geometric template models of the EOMs to the MRI images of individual patients [52]. Image features of the EOMs were detected and filtered to guide fitting of the generic anatomical template. However, the template model has to be built by considering anatomical characteristics of the EOMs. In addition, a global registration between the image sequence and the template model had to be performed at the beginning.

3.3 Method

The template-based eyeball shape reconstruction approach is outlined in Algorithm 1, the details of which are presented in the following.

Algorithm 1 Template-based eyeball Reconstruction

1: Eyeball boundaries B_s segmentation from sagittal MR images
2: Eyeball boundaries B_c segmentation from coronal MR images
3: Boundary points 3D alignment using ICP algorithm
4: B-Spline eyeball surface fitting $S_{BSpline}$ using $B_c \cap B_s$
5: Surface subdivision S_{subdiv} to generate to intensive vertices P from $S_{BSpline}$

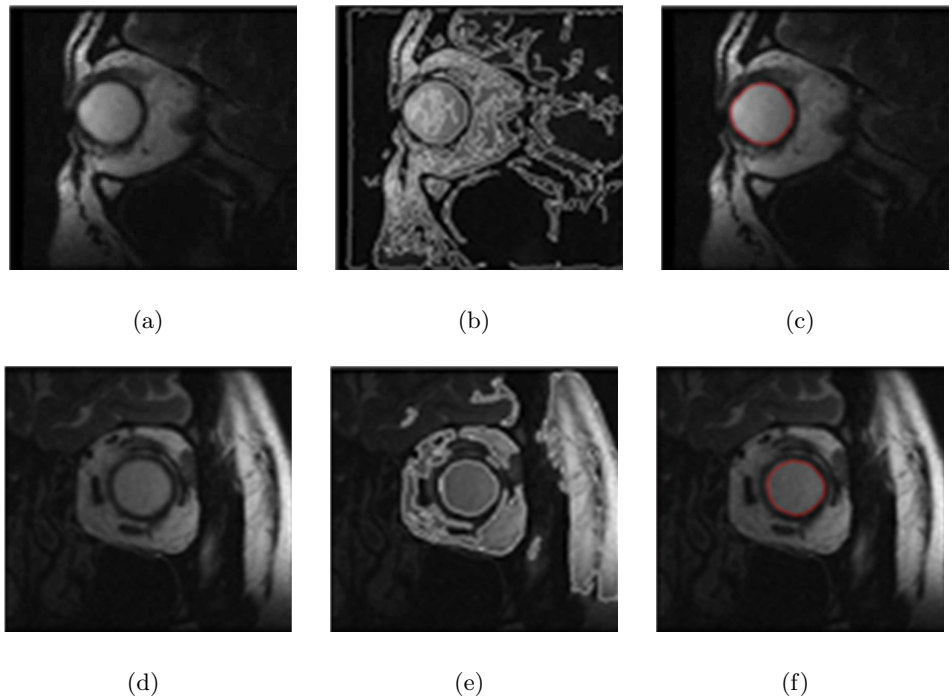

(a) (b) (c)

(d) (e) (f)

Figure 3.1: MRI image segmentation. (a)(c) Images resulted from application of Gaussian filter; (b)(d) Canny edge detection was applied to all images to extract landmarks; (e)(f) Eyeball boundaries were determined from Deformable Snake method

3.3.1 Image Segmentation

Compared to T1-weighted MRI, T2-weighted MRI provides excellent contrast between the eyeball and its surrounding tissues and hence enables automated boundary segmentation. The segmentation method is described in Fig. 3.1. The original images in the sagittal view

(Fig. 3.1(a)) and coronal view (Fig. 3.1(d)) were first preprocessed by a Gaussian filter. The Canny edge detection method [53] was then applied to extract the structure boundaries with the specified Canny sensitivity thresholds [0.06 0.15] (Fig. 3.1(b) and Fig. 3.1(e)). As can be seen from Fig. 3.1(b), edge detection outputted undesired landmarks inside the eyeball. Therefore, I used Deformable Snake to determine the eyeball boundaries, the points on which were denoted by B_s and B_c respectively, from coronal and sagittal MR images (Fig. 3.1(e) and Fig. 3.1(f)).

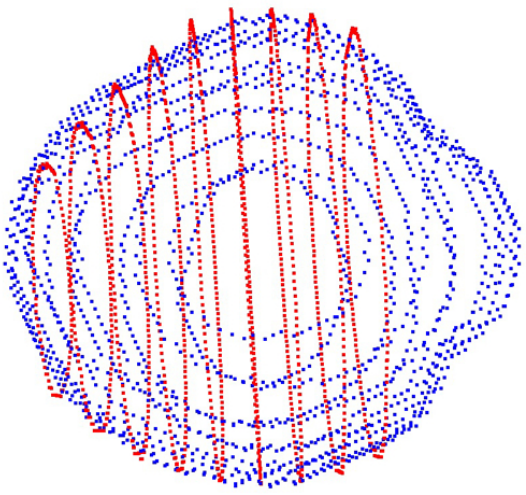

Figure 3.2: Boundaries of the eyeball in two scans were registered to correct displacement between scans

3.3.2 Boundary Registration

Registration between the two boundary sets, B_s and B_c, was performed to correct movement of the subject between acquisition of the sagittal images and the coronal images. I used a variant of the iterative closet point (ICP) [54] algorithm to find the best alignment between B_s and B_c (Fig. 3.1(c) and Fig. 3.1(f)). Neither B_c nor B_s completely sampled the whole eyeball geometry because of the difficulty in accurately segmenting images near the poles of the eyeball. In addition, B_s and B_c are from a nearly spherical structure which

may lead to ambiguous registration. To avoid such false correspondence, for each data point on one boundary, I only searched for its closest point on the other boundary that was within a predetermined distance. This was a fair constraint applied since movement of the subject between scans was expected to be small. A rigid transformation was computed which translated and rotated one set of boundary points to the other set. Fig. 3.2 shows registration results. ICP algorithm was applied to B_s (blue) and B_c (red). Subject movement was optimally eliminated which transformed the coronal boundaries to the new locations B_c (showed by the magenta points), providing a more accurate representation of the eyeball shape.

3.3.3 Eyeball Reconstruction

A two-step surface fitting process was developed to realistically model the complete shape of the eyeball from the extracted boundaries. First, a B-Spline surface [55] was fitted to all the boundaries points using an approach previously developed [56]. The fitted B-Spline surface closely modeled the overall geometry of the eyeball (Fig. 3.3(a)). However, since I used a B-Spline surface with opening endings, artifacts occurred at two ends. Achieving mesh uniformness on B-spline surfaces is important for shape analysis and is not straightforward. Therefore, I employed the Loops subdivision surface to refine the B-Spline surface. Algorithm 2 describes the approach on fitting a subdivision surface S_{subdiv} to the vertices p on the B-Spline surface.

Algorithm 2 Surface Subdivision

```
for iteration do
    for vertex p_i in S_subdiv do
        find p_i' projection p_j on the plane formed by p_1, p_2 and p_3
        p_i ← p_j
    end for
    S_subdiv surface smoothing
end for
```

Fig. 3.3(b) and Fig. 3.3(c) shows the reconstructed and refined eyeball geometry fitted

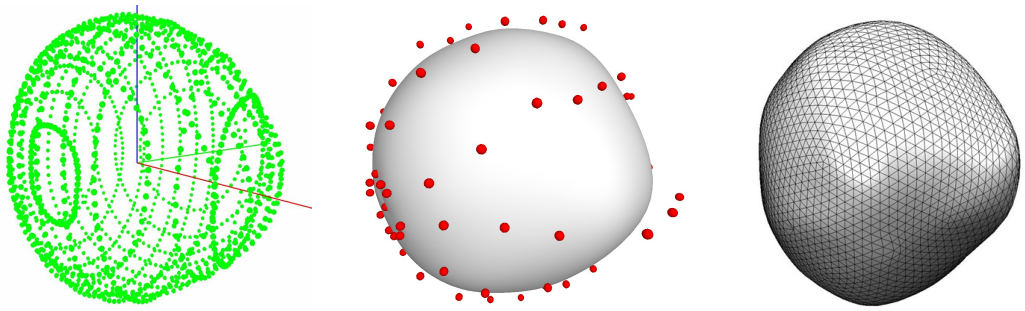

(a) (b) (c)

Figure 3.3: B-Spline surface fitting. (b) A B-Spline surface was fitted to (a) the original boundary points which were segmented from the MRI images in Fig. 3.1; (c) A subdivision surface was fitted to (b) the B-Spline surface

to the boundary points in Fig. 3.3(a). The fitting error of this example, defined as the mean distance from the boundary points to the resultant B-Spline surface, was 0.0007 mm. The subdivision fitting error, defined as the mean distance from the vertices on the subdivision surface to the B-Spline surface, was 0.05mm. Both fitting errors were reasonably small, which demonstrates that the resultant subdivision surface closely represent the geometric shape of the eyeball.

3.4 Eyeball Quantitative and Evaluation

Based on the reconstructed eyeball surfaces, for the first time, I apply Gaussian curvature [57] as a new metric to analyze shape of the cornea surface. Using Gaussian curvature and geometric relationship between the left and right eyeballs, the local coordinate system (LCS) for each eyeball can be created as the standardized coordinate system to better describe the topology features of the eyeball. With subject-specific LCS established, eight other metrics (surface area, volume, LCS axial length (Axial L), LCS horizontal length (Horiz L), LCS vertical length (Vert L), ellipsoid axial length (Axial L), ellipsoid horizontal length (Horiz L), and ellipsoid vertical length (Vert L) can be computed to parameterize and quantify the geometric features of the eyeball in 3D. Some of these metrics have been

used in previous work [50,51] and here I propose a more comprehensive set of features. The tenth metric is the eyeball Sphere Distance Deviation (SDD), measuring the deviation of the eyeball to the sphere that best approximate it. I will introduce how these metrics were calculated from the 3D models.

3.4.1 Cornea Feature Analysis using Gaussian Curvature

In computational geometry, the Gaussian curvature of a point on the surface is the product of the principal curvatures at that point [57]. The principal curvatures are the normal curvatures, which measure the maximum and minimum blending of the surface at each point. The tangent plane of a point with positive Gaussian curvature intersects the surface at a single point, whereas the tangent plane of a point with negative Gaussian curvature cuts through the surface [58]. Therefore, the Gaussian curvature determines whether a surface is locally convex or locally concave. If the Gaussian curvature is positive (negative), then the surface at that point is convex (concave). The actual curvature value other than the sign quantitatively implies the degree of convexity (concavity) at any point on a surface. Fig. 3.4(a) illustrates the Gaussian curvature on the two eyeball surface of one subject. The Gaussian curvature is relatively high near the cornea (red) and low near the ciliary body (blue). This metric can be used to show the shape characteristics of myopia and highly myopia, since it has been suggested that myopia is associated with deformation of the cornea [51]. Such deformation might stretch the cornea along the axial direction which leads to more extrusive cornea shape accompanied by a more concave transition between cornea and sclera.

3.4.2 Local Coordinate System (LCS)

As stated above, forming a local coordinate system is the key to better parameterize features of the eyeball surface. In this section, I describe how the LCS can be established for each eyeball. First, geometric center o of the eyeball surface (shown as the cyan ball in Fig. 3.4(b)) was calculated, and the global coordinate system (o:X,Y,Z) was initialized at o.

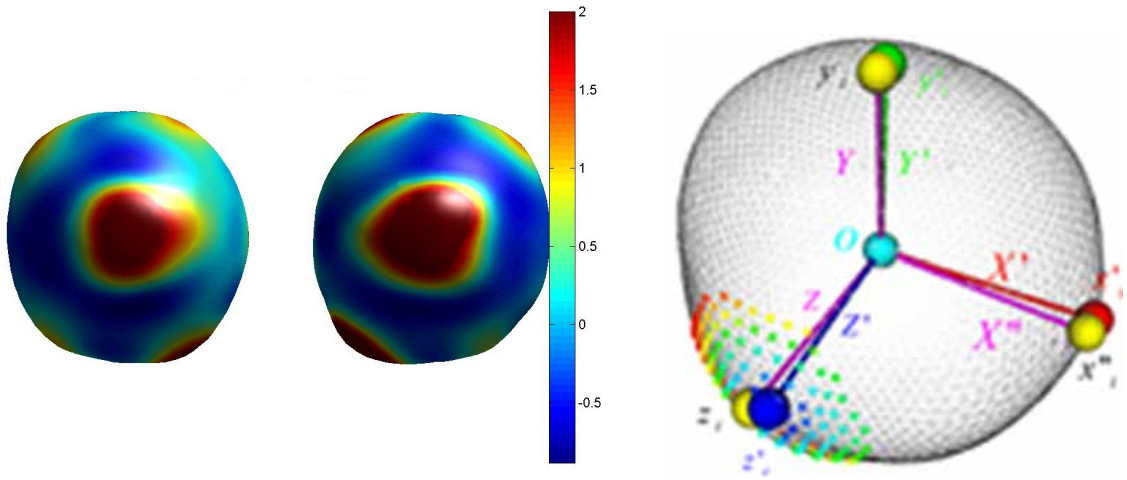

(a) (b)

Figure 3.4: Cornea Feature Analysis using Gaussian Curvature. (a) Gaussian Curvature; (b) LCS of an eyeball.

The intersection point Z_i (yellow ball) of the Z-axis (magenta axis) and the eyeball surface was close to the center of the cornea because of how the MRI scan was oriented. Since the calculated Gaussian curvature quantifies local geometric characteristics of the cornea surface, I applied k-nearest search algorithm [59] at point Z_i to find the region on cornea surface that had the highest Gaussian curvature (see small blue dots on eyeball surface in Fig. 3.4(b)). Then arithmetic mean of the region was computed to obtain a new center of cornea $Z_i{}'$ (blue ball). By connecting o and $Z_i{}'$, a new Z' axis was generated (blue axis in Fig. 3.4(b)).

Second, I followed Singh et al.s method [50] to create the initial X"-axis (magenta axis) by forming a line that goes through the left and right eyeballs geometric center. Notice that I could not guarantee that X" is perpendicular to Z', so further adjustment was needed.

Finally, the cross product between Z' and X" formed the new axis Y' (green axis). The new X' axis (red axis) was calculated through the cross product of the Y' and Z'. The resultant LCS (o:X',Y',Z') was shown in Fig. 3.4(b).

3.4.3 Sphere Fitting of the Eyeball

The geometric shape of an emmetropic eye is close to being spherical in 3D whereas an abnormal eye such as myopia and highly myopia shows deformation or distortion from a sphere [51]. Moriyama et al. introduced a new metric that classified the highly myopic eyes into four basic types on the 3D reconstructed eyeball surface [51]. But this classification procedure can only be performed based on the experienced professionals judgment to manually analyze each eye and their agreement on the classification results. This time-consuming process is subjected to human error. In addition, the topologic features of the eye can hardly be measured using the approach in [51], making it difficult to describe the topologic difference between the emmetropic and abnormal eyes. To overcome this problem, I applied the RANSAC algorithm [60] to fit eyeball surface by a sphere and measure the Sphere Distance Deviation (SSD) between the surface and the sphere. The main steps were outlined in Algorithm 3.

Algorithm 3 Fitting Sphere to the eyeball subdivision surface

1: Sample the eyeball surface and output a point cloud
2: Apply RANSAC algorithm to fit a spherical surface to the point cloud
3: Compute the SSD between the eyeball surface to the sphere surface

Fig. 3.5(a) illustrates the sphere fitting result that closely approximated the eyeball. I define the SSD Δd, which measures distance between the eyeball and the sphere, as: $\Delta d(p_i) = d(p_i) - r,$ for $i = 1, \ldots, n$ where p_i is a vertex on the eyeball surface, $d(p_i)$ is the distance from p_i to the fitted sphere center and r is the radius of the fitted sphere. $\Delta d(p_i)$ is positive if p_i is outside the sphere, and $\Delta d(p_i)$ is negative if p_i is inside the sphere, which means eyeball surface at point p_i intersects with the sphere. When $\Delta d(p_i) = 0$, p_i is on the sphere surface. To better represent the SSD, the $\Delta d(p_i)$ is normalized between 0 and 1. Fig. 3.5(b) shows histogram of the normalized $\Delta d(p_i)$, and Fig. 3.5(c) illustrates the colored sphere that maps $\Delta d(p_i)$ on the fitted sphere surface.

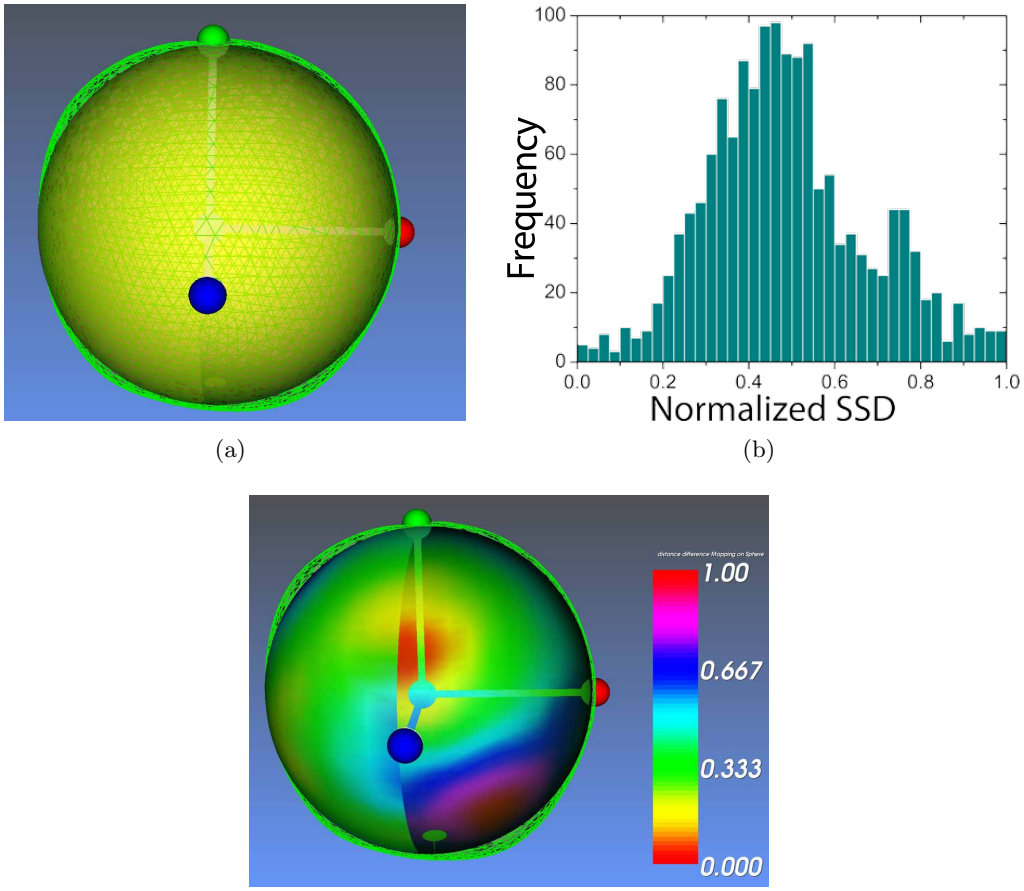

(a) (b)

(c)

Figure 3.5: Analysis of the eyeballs deviation from a sphere. (a) Eyeball and fitted sphere; (b) Histogram of computed SSD; (c) Color mapped SSD.

3.5 Result

Table 3.1 summarizes the quantitative results for twenty eyeballs reconstructed from MRI of ten healthy subjects, who were identified only by their two-letter IDs. Anonymous MRI data was provided by Dr. Joseph Demer at UCLA. According to the table, the mean Axial, Horizontal (Horiz) and Vertical (Vert) Length (L) in the local coordinate system are almost the same. The mean standard deviation of SSD is 0.005 ($\pm$ 0.05) mm, showing that the fitted sphere can closely approximate the eyeball surface and measure spherical deviation.

Table 3.1: Eyeball quantitative results

		Mean	SD
Surface Area (mm^2)		1673.6	151.52
Volume (mm^3)		6395.31	877.62
LCS	**Axial L (mm)**	23.2	1.14
	Horiz L (mm)	23.33	0.93
	Vert L (mm)	23.85	1.24
Ellipsoid	**Axial L (mm)**	21.94	1.06
	Horiz L (mm)	23.12	0.95
	Vert L (mm)	23.56	1.28
SSD (mm)		0.005	0.05

3.6 Conclusion

I have developed a computational framework for building subject-specific eye model from MRI, using parametric surface fitting. 3D eyeball geometric models from difference subjects can be accurately and efficiently reconstructed. Analysis results are consistent with previous studies [49–51]. Moreover, the proposed approach provided comprehensive quantitative analysis of ocular anatomy and morphology by using the eight basic metrics. I proposed two more metrics, the Gaussian curvature and the sphere distance deviation, that have not been utilized previously but could improve the accuracy and efficiency of the diagnosis of the vision disorders. I would like to apply the approach on more datasets and aim to find the correlation between refractive error and shape feature, which can then be used for clinical diagnosis.

Chapter 4: M3VR–A Multi-step, Multi-resolution, and Multi-volumes-of-interest Volume Registration Method Applied to 3D Endovaginal Ultrasound

The work presented in this chapter has been published in [61, 62].

4.1 Introduction

Image registration is the process of aligning two or more radiological images in two or three dimensions [63]. It has been widely applied for radiotherapy treatment planning [64], image segmentation [65], image guided surgery [66], and longitudinal monitoring [67] among many other applications. Automated and semi-automated registration methods seek to determine a transformation between two or more image datasets possibly of different imaging modalities, different subjects, and/or at different times by solving an optimization problem that maximizes the similarity between the transformed datasets. This has been an active area of research [1, 63, 68–73]. Three-dimensional (3D) volume registration is more challenging than 2D due to the increased number of degrees of freedom in the transformation and the difficulty in quantifying volumetric discrepancy.

A common application of 3D image registration is longitudinal monitoring before and after an interventional procedure. Ultrasound imaging is attractive for longitudinal monitoring since it is inexpensive and safe. 3D volumetric registration of ultrasound images is considered more challenging than other modalities such as Computed Tomography and Magnetic Resonance Imaging (MRI) [74] because of the low signal-to-noise ratio, heterogeneity of echo textures, and low ultrasound image contrast due to artifacts and attenuation [75]. In particular, ultrasound imaging of soft tissue can be subject to considerable signal to noise ratio variation [75], frequency-dependent attenuation of the backscattered signals [76],

and tissue deformation. In addition, interventional procedures, such as needle biopsy, often induce tissue deformation and hematoma [77, 78]. As a result, datasets that were acquired from the same patient before and after an intervention can be considerably different.

Existing registration approaches [1, 79–85] are not suitable to produce precise alignment under these challenging conditions. As such, there is a need to develop new automated deformable and volumetric registration methods. Rigid registration will likely fail to find the optimal alignment because the anatomical changes obviously violate the rigidity assumption. Contrarily, non-rigid registration might strive to accommodate those changes but may result in incorrect deformation in other regions due to the many degrees of freedom associated with these methods. In this study, I developed and validated a novel 3D ultrasound registration method that overcomes these challenges.

The proposed method is called M3VR, for Multi-step, Multi-resolution, Multi-volume of interest Volumetric Registration. It is a novel weighted multiple volume-of-interest (VOI) registration method that can be applied on volumetric data of any medical imaging modality where there are rigid non-deformable structures (such as bony landmarks) and also deformable tissue. In the first step, a rigid registration is applied on a single VOI containing rigid structures for an initial alignment. In the second step, multiple VOIs that are distributed across the whole volume and do not include the anatomically different regions are selected to add influence of soft tissue structures. Then a weighted multiple VOI registration is performed to calculate the optimal alignment of all these VOIs in order to refine the alignment obtained from the first step.

I evaluated the M3VR in a 3D Endovaginal Ultrasonography (3DEVUS) application for assessing and monitoring pelvic floor disorders, which affect nearly 24% of US women [86,87]. Pelvic organ prolapse (POP) is a common type of pelvic floor disorder in which the pelvic organs (bladder, uterus and rectum) descend downward due to loss of mechanical integrity of the pelvic floor (Fig. 4.1 (a)), particularly that of the levator ani muscle and associated connective tissues [88]. POP is associated with significant dysfunction and detrimental impact on quality of life. Injury to the levator ani muscle during vaginal birth is a significant

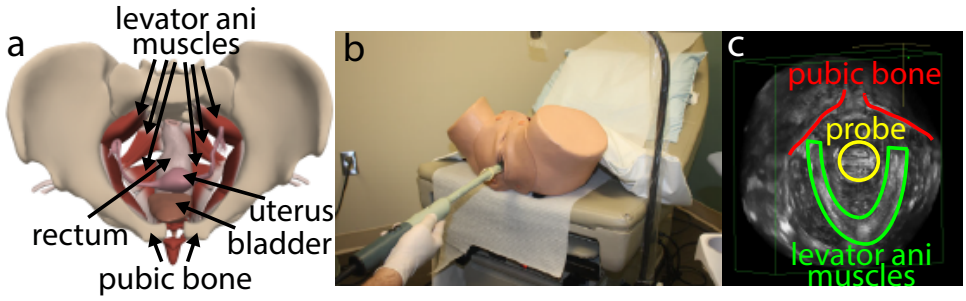

Figure 4.1: The anatomy of the women pelvic floor. (a) Axial view. Pelvic floor muscles are the layer of muscles that support pelvic floor organs, assist in urinary and fecal continence and stabilize connecting joints. (b) Schematic drawing of 3D Endovaginal Ultrasound Imaging with 360° rotational transducer using a BK Ultrasound System (Flex Focus 500) [1]. (c) Pelvic floor muscle appears as a V-shaped structure in 3DEVUS (green boundary). Pubic bone and probe can also be viewed interactively during acquisition and offline.

risk factor for developing POP [89]. The effects of these injuries can be additive with subsequent births and can result in levator ani muscle atrophy and increased risk of POP [89, 90]. Accurate and timely detection of injury to the levator ani muscle is critical to the effective treatment of POP. Modern imaging techniques such as MRI and ultrasonography are currently used clinically in the non-invasive examination of levator muscle injury [86, 89, 91–95].

Compared to MRI, ultrasonography has the advantage of being fast, cost effective, and easily available. 3DEVUS provides a comprehensive overview of the pelvic floor anatomy by performing a 360° field-of-view scanning (Fig. 4.1 (b) and Fig. 4.1 (c)). Quantitative analysis of the progression or repair of muscle injury requires longitudinal monitoring and volumetric registration of the acquired 3DEVUS images [96].

In this chapter, I first review existing ultrasound image registration methods in Section 2. Section 3 describes the pelvic floor data used in this study and the M3VR method. Validation metrics and procedure are also discussed. Section 4 presents the results on the application of M3VR on 3D endovaginal ultrasound data, parameter determination, and validation of the results. In Section 5, I discuss limitations and future directions for this work.

4.2 Related Work

3D volume registration methods can be generally classified into two types: rigid registration using linear transformation and non-rigid registration using nonlinear transformation to compensate for deformation of structures [97, 98]. For example, a rigid transformation that includes translation and rotation can be used to align two volumetric data. When significant differences are known to exist due to natural variations among subjects or changes in physical structures over time due to tumor development or other factors, non-rigid image registration should be applied to allow localized deformation and to optimally align different datasets [99]. For this problem, I chose to solve for a rigid registration because of the overall rigidity of the volume. Non-rigid transformation may introduce too many degrees of freedom. This may potentially overfit the data to heterogeneous ultrasound echo textures and result in undesired muscle deformation.

Existing 3D ultrasound registration methods are either feature-based [100–103], intensity-based [83, 104–107], or integrated of the two [108, 109]. Feature-based methods rely on identifiable features that are extracted from ultrasound image for registration optimization. These features can be anatomical landmarks, structure boundaries, surfaces, or statistical shape features. Many 3D feature-based methods have been developed. A few representative ones include a surface-based, nonlinear registration method to align ultrasound images to histological data in 3D [100], a temporal and spatial registration approach to align pre- and post-stress ultrasound images [101], a novel method based on spatial Gabor texture similarity represented by statistical kernel distributions [102] and registration between an ultrasound volume and a statistical shape model using local phase bone features [103]. 3D scale- and rotation-invariant key points have been used to identify features [79,84]. However, definition and matching of these key points can be difficult.

Compared to the intensity-based methods, feature-based approaches are recognized to be more robust to intensity variation and less susceptible to local minima [108], however require additional steps on feature extraction. Intensity-based methods [83, 85, 104–107, 109, 110]

use raw pixel intensity values to assess similarity between two datasets and do not need additional features. One recently proposed intensity-based registration approach involves block-matching and an outliner rejection method to determine an affine transformation between ultrasound volumes [83]. Mutual information-based methods are commonly used in registering ultrasound volumes [106, 107]. An intensity-based deformable registration method was employed for 3D ultrasound registration through a variational framework [85]. Intensity-based approaches might be computationally extensive and converge to local minima.

I experimented with both feature-based and intensity-based registration. I decided to perform intensity-based registration because it produces good results and requires minimal user input. Anatomical features in the data include the inner boundary of the pubic bone and outer boundary of the levator ani muscle. However, these features were not be clearly visible in all datasets. Even if they were, the features cannot be segmented reliably and automatically. In addition, pixel intensities present more information than what sparse anatomical features present and thus theoretically have the advantage of being robust to noise. Nevertheless, I take advantage of the usefulness of anatomical features in explicitly measuring the correspondence of two datasets and use them to quantitatively validate registration results.

4.3 Methods

4.3.1 Ultrasound Imaging of the Pelvic Floor

As part of a previous study, I collected 3DEVUS data from subjects who had different degrees of levator ani muscle injury and who underwent biopsy [111]. 3DEVUS was performed on each patient once before, twice during, and once after the biopsy (Fig. 4.2). The four datasets (94mm×94mm× 65mm; spatial resolution: 0.118mm/pixel) per patient include: (1) a pre-biopsy ultrasound volume (D1 in Fig. 4.2 (a)) with muscle intact for pre-operative examination, (2) an ultrasound volume with biopsy needle positioned on the left side (D2

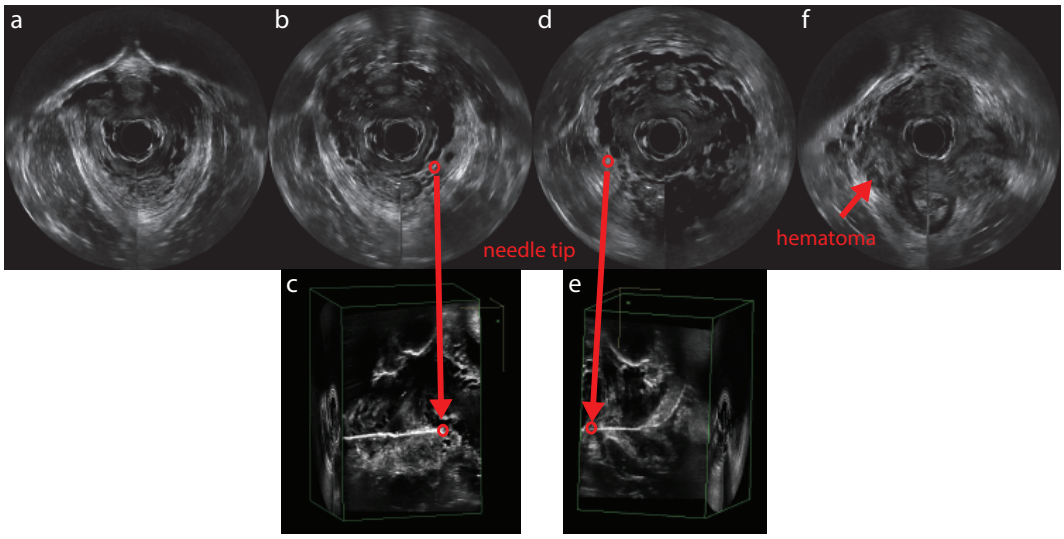

Figure 4.2: Four phrased 3DEVUS data collected from the same subject during biopsy examination. (a) Pre-biopsy 3DEVUS volume. (b) 3DEVUS volume with biopsy needle on the left. (c) Needle inserted on the left is more visible from a different view. (d) 3DEVUS volume with the biopsy needle on the right. (e) Needle inserted on the right viewed from the sagittal view. (f) Post-biopsy 3DEVUS volume. The development of hematoma can clearly be seen as indicated by the arrow, which showed up as a dark region at the biopsy site.

in Fig. 4.2 (b)), (3) an ultrasound volume with biopsy needle positioned on the right side of the pelvis (D3 in Fig. 4.2 (d)), and (4) a post-biopsy ultrasound volume (D4 in Fig. 4.2 (f)). D2 and D3 were obtained during biopsy to guide placement of the J-hook needle in the pelvic floor muscle region with suspected muscle defect. This technique was similar to a previous study by Busacchi et al. [112].

Our long term goal is to apply quantitative ultrasound analysis to assess pelvic floor muscle injury, which correlates muscle characteristics obtained from statistical ultrasound texture analysis at the biopsy location to those obtained from histologic analysis from the needled biopsy sample. The biopsied tissue was not visible in the ultrasound volume obtained during biopsy because of the needle. However, it was completely visible and intact in the pre-biopsy data. In order to establish an accurate correlation, the needle location needs to be determined in the pre-biopsy data such that quantitative ultrasound analysis

can be performed on the exact biopsied tissue. A precise spatial registration method that optimally aligns the ultrasound volumes with needle inside (D2 and D3) to the volume without needle (D1) is required to objectively estimate biopsied tissue location. Although these volumetric data were acquired from the same subject, optimal alignment is not a trivial problem. D1, D2 and D3 were taken at different time during the procedure with ultrasound probe repositioned for each dataset. There would have been unavoidable displacement of the probe by the clinician, which caused tissue deformation near the probe and variable transformation of the imaged volume. These volumetric data were also subject to significant tissue change due to insertion of the needle and development of post-biopsy hematoma.

4.3.2 M3VR Registration Framework

The M3VR framework is shown in Fig. 4.3. D3 is defined as the fixed ultrasound volume. D1 and D2 are defined as the moving ultrasound volumes, which are to be aligned with the fixed volume D3. In the first step, an intensity-based multi-resolution rigid registration method was performed on the pubic bone sub-volume to provide an initial alignment of the moving ultrasound volumes (D1 and D2) to the fixed ultrasound volume (D3).

As shown in Fig. 4.1 (c), the pubic bone is located only in the upper half of the volumetric data. Registering the whole volume based on matching a much smaller sub-volume may be subject to bias because of the heterogeneous characteristics of ultrasound imaging and offset of the sub-volume from the center. The resultant error would have been the most severe at places far from the sub-volume. A related issue is the bias of fit problem that has been examined previously in the computer vision community [113]. However, such locally focused registration can effectively bring the two datasets closer to each other, which facilitates subsequent and more sophisticated registration.

In the second step, spatially weighted, intensity-based, multiple VOIs, and multiple resolution registration was performed to optimize the alignment between transformed D1 and D2. The sub-volume ultrasound data at the biopsy site can be obtained from the transformed needle location for further analysis. I performed extensive validation to ensure

Algorithm : M3VR

Input: Fixed ultrasound volume, V_F
Moving ultrasound volume, V_M
Output: Registered moving ultrasound volume, V_M*
Step 1: Multi-resolution pubic bone volumetric registration
Select pubic bone volume of interest, $V_{F_{PB}}$
Compute multi-resolution pyramid
for $l = L, L-1, ..., 1, 0$ // *iterate multi-resolution levels*
  Solve for optimal rigid transformation between $V_{F_{PB}}$ and V_M at multi-resolution level l
  Propagate $T_{\hat{\theta}}^{l}$ to level l-1
end
Step 2: Multi-resolution and multi-regional volumetric registration
Select pelvic floor muscle volume of interest, $V_{F_{PM1}}$ and $V_{F_{PM2}}$
Compute multi-resolution pyramid
for $l = L, L-1, ..., 1, 0$ // *iterate multi-resolution levels*
  Solve for optimal rigid transformation between $V_{F_{PB}}$+$V_{F_{PM1}}$+$V_{F_{PM2}}$ and V_M at multi-resolution level l
  Progagate $T_{\hat{\theta}}^{l}$ to level l-1
end
Compute V_M* using optimal transformation T_{θ^*}

Figure 4.3: Algorithm of M3VR. Two-step multi-resolution volume registration. Step 1: pubic bone sub-volume registration. Step 2: spatially weighted multiple sub-volumes registration on pubic bone and pelvic floor muscles.

the robustness and accuracy of the proposed method. The whole registration pipeline was implemented in C++ and ITK [114].

The M3VR method optimizes alignment by combining multiple volumes of interest that accommodate different anatomical structures. The main idea is to select multiple sub-volumes that do not contain changed anatomical structures. If these sub-volumes are dispersed over the volume, the bias of fitting is unlikely to occur. The pixel intensity values of different anatomical structures may have different ranges. This needs to be considered in the overall similarity measurement. For instance, bone appears brighter than muscle

in ultrasound images and thus has higher intensity values. To adjust the contributions of different structures in the combined cost function to enforce either fairness or preference of alignment, weights are applied on the selected volumes of interest to influence their significance. I will now describe the methodology in detail.

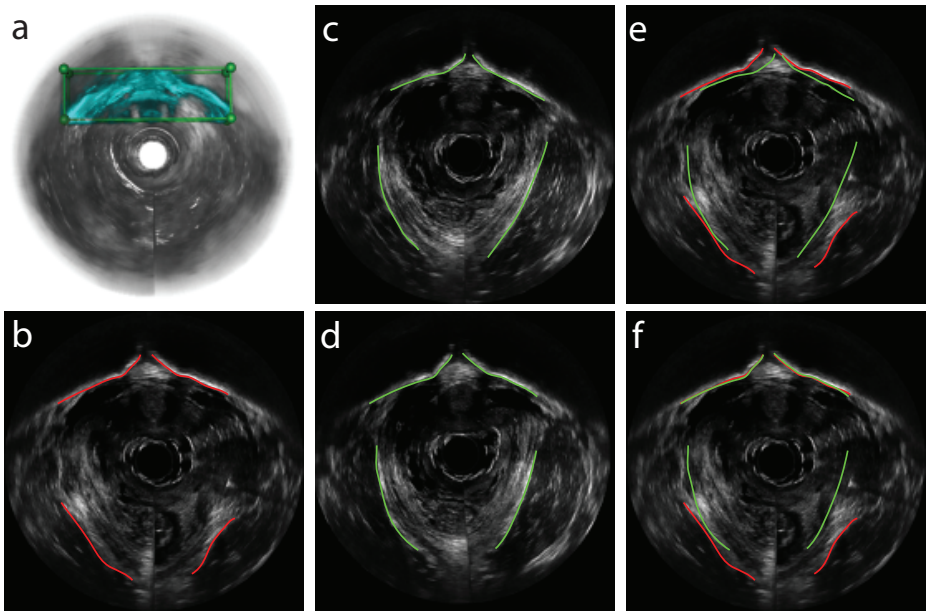

Figure 4.4: Intensity-based volumetric registration on pubic bone VOI. (a) A cubic VOI enclosing the public bone was defined in the fixed image volume (green grid). The pubic bone was rendered in cyan simply to highlight the bone dimensions. (b) One slice image from fixed image volume with pubic bone and muscle boundaries. (c) Corresponding image slice before registration in the moving image volume. (d) Corresponding image slice after registration in the transformed moving image volume. (e) Pubic bone and muscle boundaries comparison before registration, the initial boundaries are not matched between fixed and moving images. (f) Pubic bone and muscle boundaries comparison after registration. The pubic bone boundaries are better aligned demonstrating the effectiveness of first step registration.

4.3.3 Step 1: Multi-resolution Pubic Bone Volumetric Registration

In the first step, I apply the intensity-based volumetric registration method to find the matching homologous regions across the fixed and moving ultrasound volumes demonstrated in Fig. 4.4. Considering the pubic bone region as the most rigid and consistently textured

structure in the imaged region, I first calculate the initial transformation based on a volume of interest containing the pubic bone (Fig. 4.4 (a)). The VOI is first defined by a 3D bounding box of the pubic bone in D3 and is considered fixed (Fig. 4.4 (a)). A 3D rigid transformation T_θ was computed by optimizing the registration cost function (Eq. 4.1) so that another dataset (D1 or D2) is optimally aligned with D3.

$$\hat{\theta} = \underset{\theta}{\operatorname{argmin}}\, \phi(V_F, T_\theta(V_M)) \tag{4.1}$$

The object function ϕ in Eq. 4.1 measures the similarity between the fixed VOI V_F and the moving VOI V_M. Multi-resolution registration is performed to enhance the registration robustness against ultrasound image texture variation [80]. Three intensity-based similarity metrics were examined to compare their effectiveness in aligning the 3DEVUS data.

Mean Square Error (MSE) computes the averaged pixel-wise intensity difference:

$$MSE(V_F, V_R) = \frac{1}{M \times N \times T} \sum_{i=1,j=1,k=1}^{M,N,T} (V_{F(i,j,k)} - V_{R(i,j,k)})^2 \tag{4.2}$$

where $V_{F(i,j,k)}$ and $V_{R(i,j,k)}$ represent voxel intensities at position (i, j, k) in fixed volume V_F and registered volume V_R respectively. $M \times N \times T$ is the total number of voxels in the VOI. MSE is based on the assumption that the pixel intensity of the same homologous point remains constant. Smaller MSE indicates more precise registration.

Normalized Cross Correlation (NCC) computes pixel-wise cross correlation normalized

by the square root of the autocorrelation of the two volumetric images:

$$NCC(V_F, V_R) = \frac{\sum_{i=1,j=1,k=1}^{M,N,T} V_{F(i,j,k)} \times V_{R(i,j,k)}}{\sqrt{\sum_{i=1,j=1,k=1}^{M,N,T} V_{F(i,j,k)} \times \sum_{i=1,j=1,k=1}^{M,N,T} V_{R(i,j,k)}}} \tag{4.3}$$

NCC is between 0 and 1. NCC equal to 1 indicates that the two volumes have identical intensities and thus an optimal alignment. Misalignment leads to smaller NCC value.

Mutual Information (MI) measures how much information that a random variable captures about another random variable. MI is calculated based on the entropy of each random variable. Mutual information between two random intensity variables of two volumetric images I_F and I_R is defined as:

$$MI(I_F, I_R) = H(I_F) + H(I_R) - H(I_F, I_R) \tag{4.4}$$

where $H(I_F)$ and $H(I_R)$ are the entropies of random variables I_F and I_R espectively. $H(I_F, I_R)$ is the joint entropy of I_F and I_R. From experiments, NCC gave the best registration results and was used on all datasets. A quantitative comparison of the three metrics is presented in Results.

Fig. 4.4 demonstrates the step 1 registration results of one dataset. To assist visual comparison, the pubic bone and muscle boundaries were manually outlined at the corresponding imaging plane. Fig. 4.4 (b) and Fig. 4.4 (c) show one image slice in fixed dataset D3 and one in moving dataset D1, respectively, before registration. Misalignment of the two pre-registration volumetric images was obvious because the corresponding bone or muscle boundaries were apart from each other in Fig. 4.4 (e). Note that the manually segmented pubic bone and muscle boundaries were only for the ease of visual comparison. The algorithm itself does not use edge features. Fig. 4.4 (d) shows the resampled image slice in D1 after registration at the same imaging plane as Fig. 4.4 (b). Fig. 4.4 (f) shows that after

registration, alignment of the pubic bone was significantly improved. This was demonstrated by the proximity of the pubic bone boundaries. However, the pelvic floor muscle regions were still misaligned (Fig. 4.4 (f)). The dissimilarity can be explained by the biased registration problem mentioned above. As a result, a rotational error occurred in regions distant from the bone VOI, such as in the muscle band.

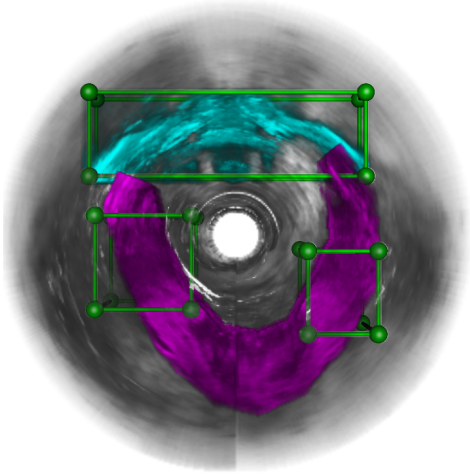

Figure 4.5: Multiple VOIs were defined near the pubic bone and pelvic floor muscle regions. Anatomical structures are colored only to highlight their inclusion in the VOIs.

Even with remaining misalignment, the registration based on the pubic bone region did manage to provide an initial alignment of two datasets to account for the different probe placements. This is necessary for subsequent multi-regional registration.

4.3.4 Step 2: Multi-resolution and Multi-regional Volumetric Registration

I developed a weighted multi-regional registration scheme to refine alignment of the whole volume in the second step to compensate for the registration bias due to the single and local VOI considered. Multiple VOIs that include the pubic bone ($V_{F_{PB}}$) and the pelvic floor muscle ($V_{F_{PM1}}$ and $V_{F_{PM2}}$) in the transferred moving volume D1 (Fig. 4.5) were selected as

the target VOIs. Because these regions are distributed in the volumetric data, they restrain each other from causing overfitting. Transformed D2 is defined as the moving volume and is transformed via registration to optimally align all target VOIs to those in the transferred D1. The weighted multi-regional registration is calculated by optimizing the cost function in Eq. 4.5, which minimizes the weighted sum similarity ϕ between multiple VOIs ($V_{F_{PB}}$,$V_{F_{PM1}}$ and $V_{F_{PM2}}$) in the fixed volume V_F and the registered moving volume $T_\theta(V_M)$:

$$\begin{aligned}\hat{\theta} = \underset{\theta}{\operatorname{argmin}}(&w_1\phi(V_{F_{PB}}, T_\theta(V_M))+ \\ &w_2\phi(V_{F_{PM1}}, T_\theta(V_M)) + w_3\phi(V_{F_{PM2}}, T_\theta(V_M)))\end{aligned} \tag{4.5}$$

w_1, w_2 and w_3 are the weights applied on different VOIs which sum to one. These weights are introduced for two reasons: (1) Ultrasound image pixel intensities of different anatomical structures such as bone and muscle are different, which influences the similarity measurement between two volumes. (2) The calculated similarity is also sensitive to VOI size, which is variable among selected VOIs. In order to manage impact of these factors, weight scalars are multiplied to the corresponding similarity measurements so that their contributions to the overall similarity can be adjusted. Values of the weights and sizes of the VOIs can be determined systematically through trial and error. The values leading to the best registration result are used.

When solving Eq. 4.5, I adopted a multi-resolution implementation in order to overcome the lower ultrasound signal-to-noise ratio, heterogeneous ultrasound echotexture, and local optimum problems [115]. Multi-resolution approach is commonly used in image processing to improve an algorithms robustness against noise. The fixed image data is first resampled at different resolutions and the moving image is resampled at the coarsest level. Starting from the coarsest level, the transformation is optimized for the pair of datasets at this level and applied on the moving image. The resulting transformed moving image is then resampled at the second coarsest level that is used in optimizing registration at this finer level. The procedure is repeated until reaching the original resolution.

4.3.5 Registration Validation

I did cross validation to assess accuracy of M3VR. M3VR is intensity-based rather than feature based. I used identifiable features such as the anatomical structure boundary to cross-validate the results. Because these features were not used explicitly in the algorithm, which utilizes pixel intensity only, I hope such an assessment can be more objective and more powerful to expose any weakness of the proposed method.

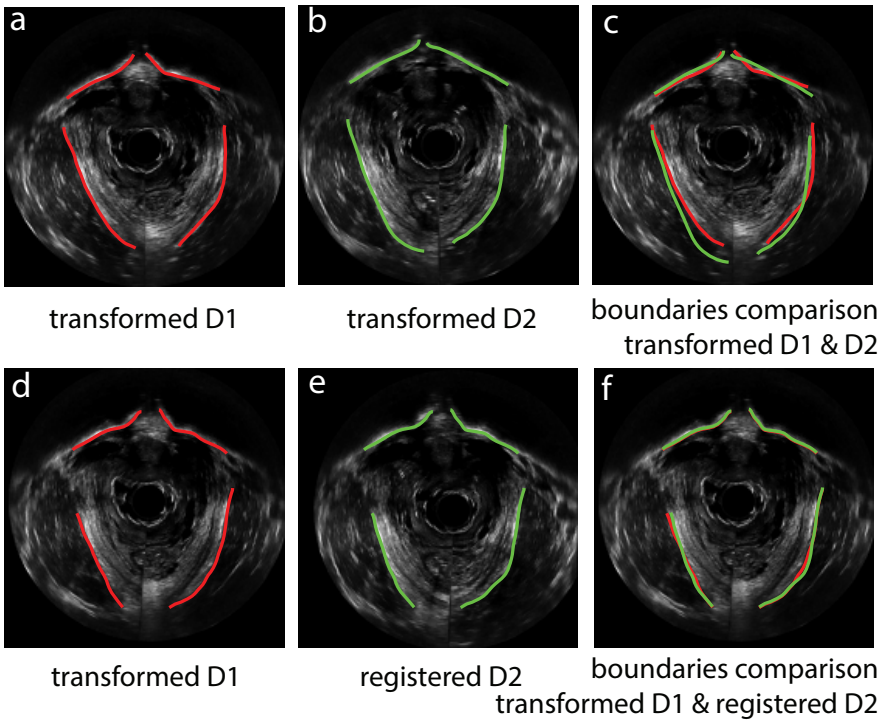

Figure 4.6: Pubic bone and muscle volumetric registration and validation after each step. Before step 2 registration, pubic bone and levator ani muscle boundaries are manually outlined in transformed D1 (a) and transformed D2 (b). The pubic bone boundaries show satisfying spatial proximity but the muscles misaligned (c). After step 2 (d) and (e), bone and muscles boundaries were effectively aligned (f).

Pubic bone and pelvic floor muscle boundaries before and after applying M3VR were manually segmented and compared both visually and quantitatively. Fig. 4.6 demonstrates how the validation was perform, with more results summarized in Results. Fig. 4.6 (a) and Fig. 4.6 (b) show image slices at the same spatial location from transformed D1 and D2 after

the first step registration. Overlaid bone boundaries (Fig. 4.6 (c)) show satisfying spatial proximity but the muscles do not. This indicates overfitting of the bone region. Fig. 4.6 (d) and Fig. 4.6 (e) show image slices from D1 and D2 at the same spatial location after applying the second step registration, which was effective in aligning both bone and muscle regions (Fig. 4.6 (f)). The mean distance between the two sets of curves error is 0.65 mm.

4.4 Results

I applied M3VR on Endovaginal ultrasound data of nine subjects. Registration accuracy evaluation was performed on each subject.

To test sensitivity of registration accuracy to VOI size, I experimented with the following volume sizes for the muscle VOIs: $10\times10\times10mm^3$, $20\times20\times20mm^3$,$20\times30\times20mm^3$,$20\times30\times30mm^3$, $20\times30\times40mm^3$,$20\times30\times50mm^3$,$20\times30\times60mm^3$, and $20\times30\times70mm^3$.The best values of the muscle VOI was 20mm$\times$30mm$\times30mm$. The pubic bone VOI was finalized to be 25mm$\times$37mm$\times12mm$ being a bounding box of the pubic bone. The optimal weight values were determined to be $w_1 = 0.3$, $w_2 = w_3 = 0.35$. These were obtained through systematically altering the weights between 0 and 1 with the constraint $w_1 + w_2 + w_3 = 1$.

In terms of optimization, the adaptive stochastic gradient descent optimizer was used which converged faster for the data compared to other algorithms such as the Levenberg Marquardt optimizer. The optimization was performed for 2000 iterations on each level. Different numbers of multi-resolution levels were tested and three levels was chosen. Increasing the number of levels over three did not significantly improve the performance.

I used checkerboard validation, levator ani muscle boundary proximity measurement, as well as volume intensity similarity to quantitatively evaluate accuracy of the proposed method.

4.4.1 Qualitative Validation

Fig. 4.7 illustrates registration results on one patient using the superimposed checkerboard images, which were used to for visual comparison of two registered images [116–119]. Fig. 4.7

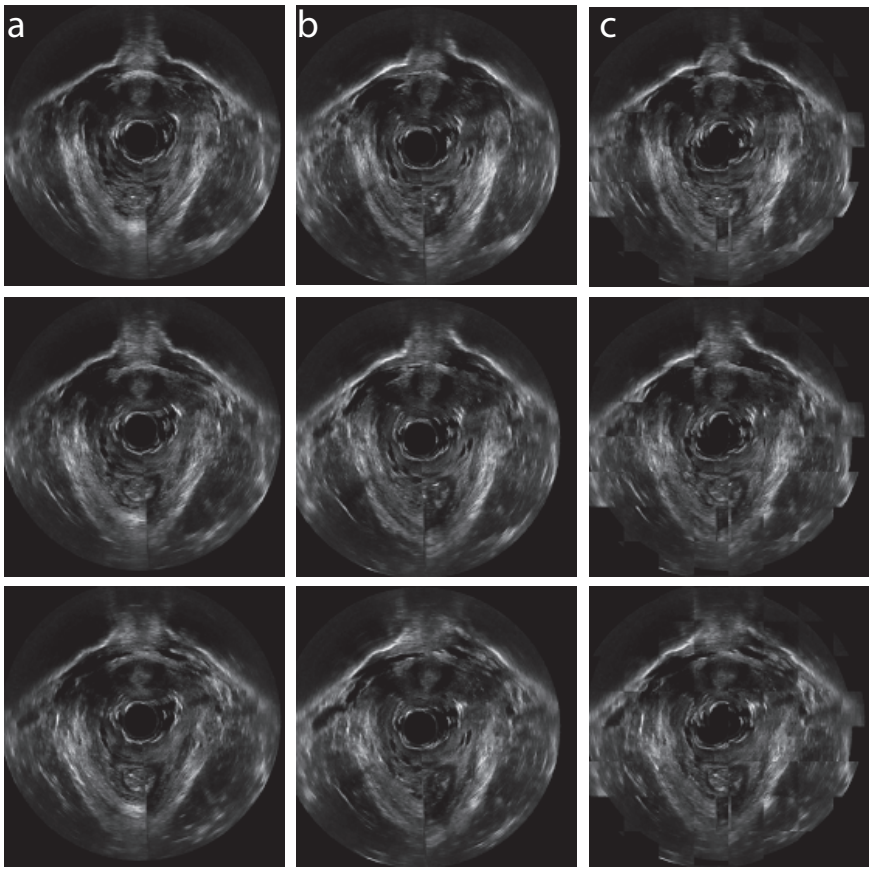

Figure 4.7: Checkerboard validation. (a) A sequence of fixed images in coronal view. (b) Moving images at the same imaging planes after 3D registration. (c) Checkerboard images of the two images on the corresponding rows, which show structure continuity and demonstrate effectiveness of M3VR.

(a) shows a sequence of image slices in the coronal view of the fixed image data. This includes the pubic bone and pelvic floor muscles at consecutive anatomical locations. Fig. 4.7 (b) shows the post-registration moving image at the same corresponding imaging planes. Comparing Fig. 4.7 (a) to Fig. 4.7 (b), I conclude that registration was able to transform the moving image to closely align with the fixed image. Fig. 4.7 (c) shows the checkerboard images generated from the corresponding fixed image slice and moving image slice in the same row. The smoothness of the checkerboard images further demonstrates the effective registration that results in good correspondence of anatomical structures in these two volumetric data. Boundaries of bone and muscle were continuous with minimal intensity

difference. For instance, the pubic bone in the synthetized images in Fig. 4.7 (c) appears to be spatially continuous. Checkerboard validation was performed on all datasets. These all show satisfying visual alignment.

4.4.2 Cross Validation of M3VR Accuracy

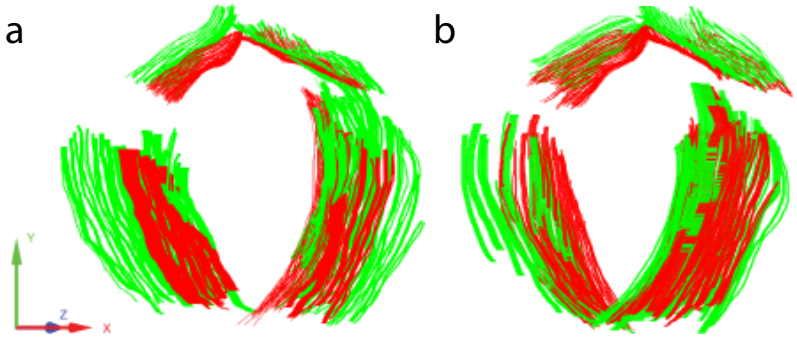

Figure 4.8: Comparison of pubic bone and levator ani muscles boundaries (a) before and (b) after applying M3VR. Green: boundaries from fixed ultrasound volume; red: boundaries from moving ultrasound volume.

I manually outlined boundaries of the pubic bone and levator ani muscle from the fixed and registered images (B_F and B_R) to quantitatively evaluate the registration accuracy. Close proximity of the two sets of boundaries indicates effective registration. I use the Mean Distance Error (MDE) to evaluate the boundary proximity. After manual segmentation of the boundaries, 3D boundary points were calculated based on the spatial resolution of the volumetric data (Fig. 4.8). For each boundary point belonging to the fixed image $p_F^i \in B_F$,$i = 1, 2, , m$, I computed its shortest distance to the registered boundary B_R. The proximity between the two sets of boundaries was then calculated as the mean shortest distance error averaged over all the m boundary points from the fixed image. A zero MDE means the two sets of boundaries overlap exactly and a large MDE indicates misalignment either translationally, rotationally, or both.

I validated the proposed method on the 3D endovaginal ultrasound data from 6 patients that showed traceable levator ani muscle boundaries. Every ultrasound volume was

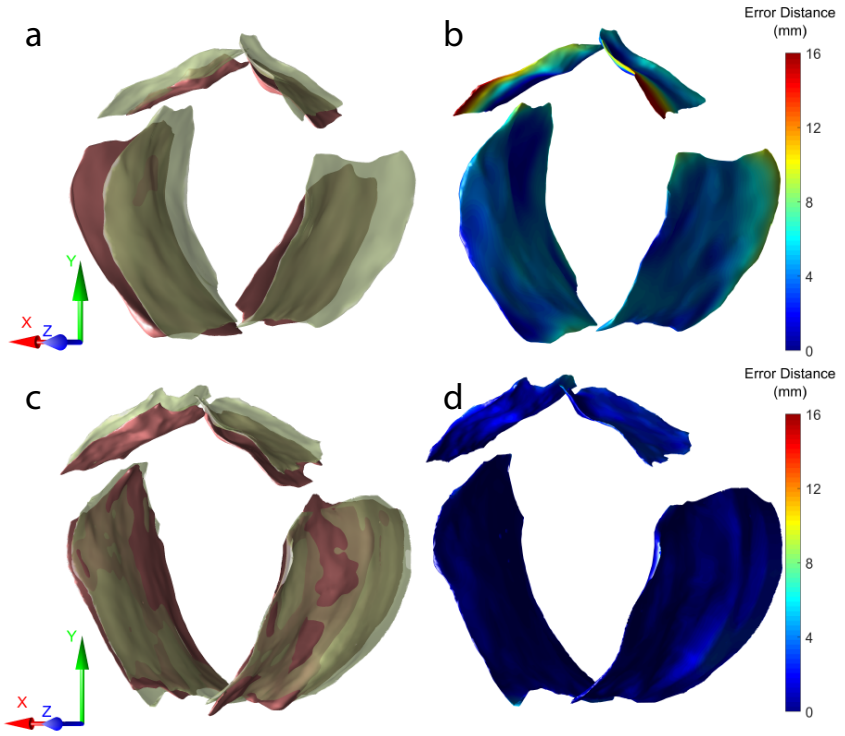

Figure 4.9: Comparison of the reconstructed pubic bone and levator ani muscle surfaces (a) before and (c) after applying M3VR. Red: surfaces reconstructed from fixed ultrasound volume; green: surfaces reconstructed from moving ultrasound volume. Visualization of one-sided error distances from the reconstructed moving surface (green) to reconstructed fixed surface (red) before (b) and after (d) applying M3VR. Error distances are visualized using a blue-green-red colormap with blue corresponding to smaller error and red to larger error.

converted into a sequence of 2D coronal images. Structural boundaries were outlined in ImageJ [120] and then remapped to 3D. Fig. 4.8 shows a visual comparison of one dataset. It can be seen that misalignment of both pubic bone and muscle boundaries (Fig. 4.8 (a)) were significantly corrected after registration. Whereas the muscle boundaries were nearly perfectly aligned, a small amount of misalignment of the bone boundary was observed in Fig. 4.8 (b). Such error resulted from the variable local deformation of the pelvic floor soft tissue in individual datasets caused by replacement of the probe. I chose to associate higher values with the muscle VOI weights because accurate alignment of the muscle region is more critical for subsequent study on examining levator ani muscle echo texture in correlation

with biopsy analysis.

Table 4.1: Cross validation results on the registration accuracy. MDE-Mean Distance Error

Sub.	**MDE of levator ani muscle (mm)**				**MDE of pubic bone (mm)**			
	Before		**After**		Before		**After**	
1	14.07	11.27	**0.78**	**0.36**	39.06	2.58	**0.30**	**0.23**
2	23.75	10.81	**0.61**	**0.39**	16.04	4.10	**0.44**	**0.29**
3	53.91	8.10	**0.71**	**0.42**	34.16	4.02	**0.43**	**0.29**
4	3.87	2.31	**0.69**	**0.35**	2.90	2.06	**0.99**	**0.33**
5	14.53	9.49	**0.76**	**0.38**	10.90	2.90	**0.76**	**0.39**
6	28.31	10.13	**0.83**	**0.37**	24.43	3.94	**0.50**	**0.34**

Table 4.1 summarizes the quantitative cross validation results on data from 6 patients. The Mean Distance Errors of the public bone and levator ani muscle are presented. The Mean Distance Errors of the pubic bone and levator ani muscles all decreased dramatically after applying M3VR. The results demonstrated the necessity of registration to accurately locate the biopsied tissue, as well as the effectiveness of the proposed approach. The maximum boundary distance error is less than 1 mm, showing the tight upper bound of the registration accuracy.

I used the shortest distance map [121] which quantitatively measures the surface proximity to evaluate the spatial distribution of misalignment. Surfaces of the pubic bone and the levator ani muscle were first reconstructed from the 3D positions of the boundary points (Fig. 4.9). I defined the one-sided error distance between a point p_M on the moving surface S_M (Fig. 4.9 - green) to the fixed surface S_F (Fig. 4.9 - red) as $d(p_M, S_F)$:

$$d(p_M, S_F) = \min_{p_F \in S_F} E(p_M, p_F),\ p_M \in S_M \tag{4.6}$$

where p_F is the point on S_F that is closest to p_M. $E(p_M, p_F)$ is the Euclidean distance

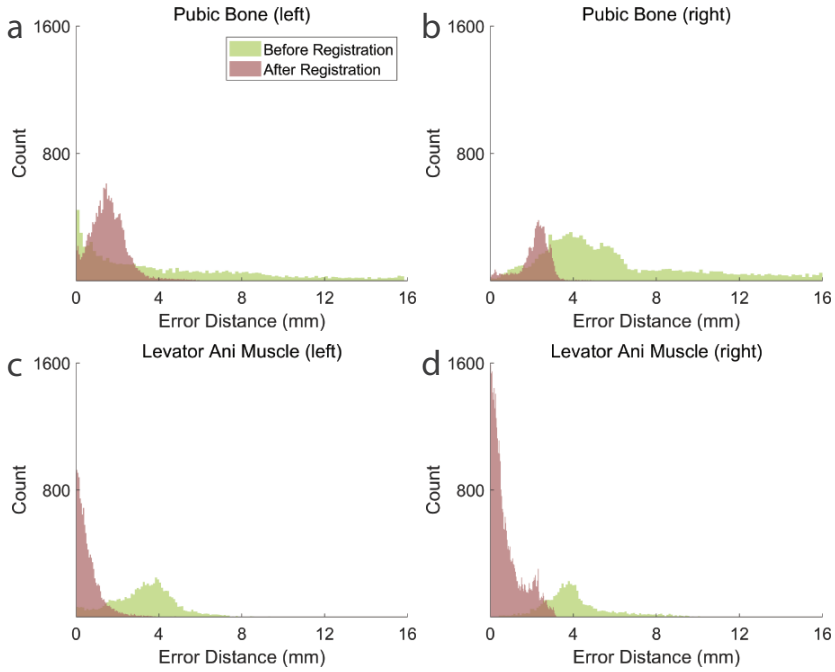

Figure 4.10: Comparing histograms of error distance of (a) left and (b) right pubic bones and (a) left and (b) right levator ani muscles surface distances before (green) and after (red) applying M3VR.

between points p_M and p_F. The shortest distance map of a surface encodes the one-sided errors of all points on it. A shortest distance map associated with small values indicates the closeness of two surfaces whereas a shortest distance map with large values reflects greater misalignment. Fig. 4.9 compares the shortest distance maps of one dataset before and after registration. Both pubic bone and levator ani muscle were misaligned before registration (Fig. 4.9 (a)), shown by the blue-green-red colormap (Fig. 4.9 (b)). The pubic bone had larger error compared to the levator ani muscle before registration. After applying M3VR, the two surfaces were much closer to each other (Fig. 4.9 (c)) as shown by the bluer shortest distance map (Fig. 4.9 (d)). I also compared the histograms of the one-sided error distance before and after registration to further analyze the corrected misalignment (Fig. 4.10). The error distances of the pubic bone and levator ani muscle significantly decreased after applying M3VR.

Table 4.2 shows the mean error of each anatomical structure. Levator ani muscles have

smaller mean error distance compared to the pubic bones. This indicates that M3VR was able to effectively improve the alignment in the levator ani muscle regions as well as reduce the overall misalignment at different spatial regions.

Table 4.2: Comparison of mean SDM on the registration accuracy

Region		**Before**	**After**
Pubic bone (mm)	Left	4.47 4.14	**1.58 0.88**
	Right	5.96 3.69	**2.16 0.74**
Levator ani muscle (mm)	Left	3.28 1.49	**0.61 0.62**
	Right	4.07 1.61	**0.78 0.75**

4.4.3 Assessment of Similarity Metrics

Different volume intensity similarity metrics including mean squares error, normalized Cross Correlation, and mutual informastion have been applied in different medical image analysis tasks. As mentioned earlier, I chose normalized cross correlation to measure similarity of the fixed image and the moving image. The decision was made after systematically examining the influence of different metrics on the registration results. Table 4.3 summarizes the analyses. These will be potentially informative for future studies on volumetric ultrasound registration. Similarity between the fixed image and the moving image measured by each of the metric before and after registration was calculated from all datasets. Consistent with the cross validation results on boundary proximity, registration using any of these similarity metrics in the objective function was able to effectively improve alignment of two volumetric data sets.

Fig. 4.11 compares mean and standard deviation of the registration accuracy in Table 4.3. Mean square error score deceased from 22.10 ± 11.62 to 6.69 ± 5.33 ($p < .001$) after registration. Normalized cross correlation score increased from 0.77 ± 0.07 to 0.96 ± 0.01 ($p < .0001$) and mutual information score increases from 0.89 ± 0.37 to 2.27 ± 0.05 ($p <$

Table 4.3: Quantitative analysis of the registration results using volume intensity similarity. Mean Square Error (MSE), Normalized Cross Correlation (NCC), and Mututal Information (MI).

Sub.	MSE		NCC		MI	
	Before	**After**	**Before**	**After**	**Before**	**After**
1	2.52	0.69	0.85	0.98	1.38	2.28
2	14.35	4.99	0.80	0.96	0.96	2.31
3	26.96	8.62	0.81	0.96	1.26	2.21
4	12.41	1.85	0.71	0.95	0.83	2.21
5	28.93	2.22	0.63	0.95	0.72	2.32
6	37.69	16.35	0.70	0.94	0.34	2.24
7	18.28	6.06	0.83	0.95	1.31	2.22
8	36.72	13.53	0.81	0.96	0.63	2.30
9	20.93	5.95	0.77	0.95	0.56	2.30

0.0001). All three scores show statistically significant improvement.

4.4.4 Computational Time Analysis

The computational time of M3VR is mainly affected by sizes of the VOIs and quality of the initial registration. The closer the two volumes are after the initial registration, the less time it takes to converge to the minimum in the second step. The overall registration time of M3VR on the night datasets included in the study took between 234.20 to 1243.73 seconds of CPU time on a Dell T7600 workstation (Fig. 4.12).

4.5 Discussion and Conclusion

In this study, I developed and validated M3VR, a volumetric image registration approach to optimally align multiple ultrasound data sets containing anatomical differences. The main contribution is that the method is able to optimally align volumetric datasets that are subject to significant variation at multiple locations. The results on 3D endovaginal ultrasound

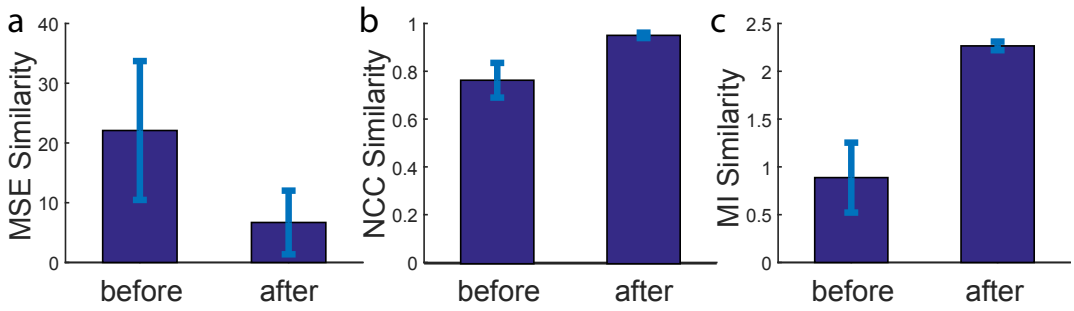

Figure 4.11: Comparison of intensity similarity measurement of the three metrics before and after registration. (a) MSE. (b) NCC. (c) MI.

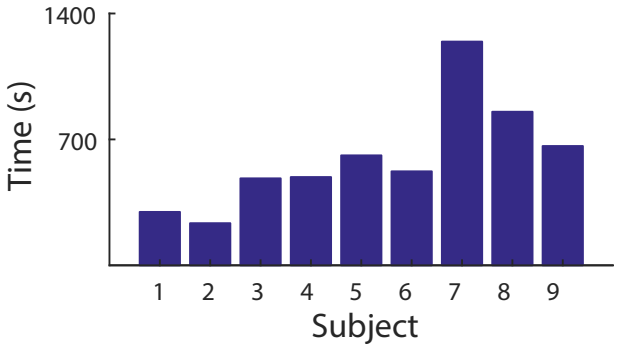

Figure 4.12: Computational time of M3VR.

data from women undergoing surgical biopsy demonstrated the feasibility and effectiveness of the proposed method. With minor modification on the similarity measurement, M3VR can be applied on registering 3D or 2D data of other medical imaging modalities, such as MRI and CT. 3D to 3D, 2D to 2D, 2D to 3D or 3D to 2D registrations can all be formulated in the proposed framework. Furthermore, M3VR can perform inter-imaging modality registration and inter-subject registration.

M3VR does not require any image intensity threshold to be specified but relies on the raw intensity values to find the optimal alignment. The only user inputs are size and location of each VOI. From the literature and the experiment, these parameters play an important role

in the registration performance. Therefore, similar to many other registration approaches, parameter tuning is a necessary step to ensure the best results. What I found was that the optimal parameter values were fairly consistent across different datasets. Therefore, there is no need to fine-tune VOI parameters for every dataset but only for one or a few representatives. Furthermore, the process can be automated by systematically varying the parameter values within a reasonable range in the computer program while saving the registration accuracy for each case for offline analysis. The program can be set to test all feasible parameter sets in one run. Then the optimal parameter values associated with the smallest error can be identified and used for all other datasets.

M3VR was designed as an intensity-based registration method that uses image intensity directly. The main reason of using image intensities and not features was that it was difficult to robustly and automatically extract features from ultrasound data of the pelvic floor. The advantage is that potential error or parameters involved in feature extraction are avoided. The limitation is that many intensity-based similarity metrics such as mean square error and the adopted normalized cross correlation, implicitly assume pixel-to-pixel intensity value correspondence. This may not hold even in the optimal alignment of medical image data [122]. Although the proposed study showed that non-pixel-wise similarity metrics such as mutual information did not lead to better results, future studies may consider other similarity metrics suitable to compare texture characteristics in the proposed framework. For instance, histograms of the pixel intensity values emphasize the high level structural property of the VOI rather than low level individual pixel intensity values and can be used in the objective function to describe underlying structures [123].

As mentioned earlier, the pelvic floor volume being scanned was completely rigid mainly due to removal and reposition of the ultrasound probe. However, the proposed method did assume rigid relationships among the multiple VOIs, which unavoidably introduced error in similarity measurement. Future work may consider a hybrid approach that allows affine transformation between any two VOIs while assuming rigidity of each VOI. Spatial relationships of the VOIs can be used as priors to initialize and constrain their relative

transformation to avoid overfitting if all VOIs are registered independently.

Implemented in C++, M3VR took up to 21 minutes to register two high resolution volumetric datasets (800×800×650). Although it is not as fast as some of the existing volumetric registration algorithms that are able to complete in seconds or a few minutes [79, 83, 110], it is still practical for many offline analysis applications. Future work on improving the computational efficiency of M3VR will be focused on reducing irrelevant volume for processing and utilizing the paralleling computing advantage of GPU [72, 83] and more powerful computer workstations. This will significantly reduce the computational time to determine model parameters and produce optimal alignment for each dataset and maintain the same accuracy, even if the computations are not in real time. With further improvement, M3VR can potentially become a useful advanced registration algorithm for many biomedical applications.

Chapter 5: Zebrafish Larvae Heartbeat Detection from Body Deformation in Low Resolution and Low Frequency Video

The work presented in this chapter has been published in [124].

5.1 Introduction

Over the past two decades, the zebrafish has emerged as a crucial vertebrate model for research in many fields such as genetics, developmental neurobiology, cardiovascular disease, and epilepsy. Advantages of using zebrafish in research include high fecundity rate, fully sequenced genome, 70% homology with human genes, and optical transparency of the larva's body [125–127]. These advantages, along with the low cost of larvae maintenance and rearing, make zebrafish an excellent model for high-throughput screening and imaging [125, 128, 129].

Because of its many advantages, zebrafish is recognized for modeling human diseases, including cardiac diseases [130]. The heart of a zebrafish larva is located posterior and inferior to the head and consists of two main components, an atrium and a ventricle [131]. Although there are anatomical differences to the human heart, zebrafish presents many parallels regarding heart function and genetically-driven cellular patterns [130–132]. Cardiac disease studies have investigated heart development in several zebrafish genetic mutants [130–132]. However, previous studies have not thoroughly investigated the heartbeat pattern of zebrafish larvae under stress conditions. This is in part due to the inefficiency of applying existing heartbeat detection methods in zebrafish larvae including performing electrocardiograms on the larvae, laser doppler microscope technique, and manual counting by experts via slow-motion replay of video recordings [129, 133]. These methods are labor-intensive, time-consuming, and often require special training. In order to reduce the

workload and preparation required for cardiac investigation, as well as reducing investigator bias and increasing repeatability, studies have developed automated image analysis software to track and analyze larva heartbeats. These programs are able to determine larva heart rate and other cardiac parameters such as beat-to-beat intervals, heart rhythmicity, and heartbeat regularity [129, 134, 135]. Heartbeat detection is typically performed by applying pixel intensity analysis over a region of interest using segmentation operations and morphological transformations [127, 129, 130].

To track the subtle motions of the larva heart, several different experimental setups and imaging techniques have been used in previous studies to improve image resolution, contrast and quality. De Luca et al. employed a confocal resonant scanner to acquire high-resolution images [129]. They also simplified motion tracking through implementation of fluorescent tags in the zebrafish larvae to express green fluorescent protein (GFP) around cardiac chamber walls and red fluorescent protein (DsRED) in red blood cells [129]. Pylatiuk et al. acquired high-resolution images of the larva's front quarter through the use of a 20 x inverted microscope in conjunction with a digital camera with high recording resolution (1392 x 1040 pixels) [135]. In their study, in order to eliminate intensity influence in acquired images, images were converted from the RGB color space to the CIE 1976 color space [135]. Chan et al. imaged blood circulation in the larva caudal vein using a stereo-microscope at 48 x magnification in conjunction with a color CCD camera [134]. While the existing methods were shown to produce satisfying results, experimental setups are often complex, requiring powerful microscopes and high-end cameras or fluorescent tags. In addition, they require observation of the larva from the lateral or ventral view to directly detect the heart's contraction, relaxation, and blood flow in order to perform cardiac analysis. However, from the dorsal view (looking down on the larva positioned ventrally, Fig. 5.2) the larva's heart components are entirely obscured, preventing direct observation of the heart. This presents a challenge for automated heartbeat detection in studies utilizing electrophysiological recordings, in which the larva is positioned upright due to the electrode being positioned in the midbrain tectum opticum.

In computer vision research, Balakrishnan et al. used a featured-based method for human heartbeat detection from videos [136]. The heartbeat frequency and beat lengths were extracted by measuring movement of the head in the video frames. Motivated by this study, I propose a robust multi-resolution motion tracking approach for automated detection of heartbeat movement of a single immobilized zebrafish larva in the ventral position using low resolution and low frame rate camera configuration. This setup is much cheaper and affordable to most research labs. The proposed method Z-HRAM was tested on larvae during electrophysiological recordings and simultaneous video acquisition with frame rates between 3 and 4 fps. Accuracy was evaluated through comparison to the electrocardiogram (EKG) signals corresponding to recorded videos and to manual heartbeat tracking results.

5.2 Method

5.2.1 Animals and Maintenance

All the animal procedures were authorized by the Ethics Committee on the Use of Animals (CEUA # 4660-1 and #4785-1) of UNICAMP, Campinas, SP, Brazil. Zebrafish tanks were kept in a temperature-controlled room at 23 C, with an automated photoperiod, being 14 hours of light cycle and 10 hours of dark cycle. The animals were raised in glass aquarium with density of 2 to 3 fish/liter under controlled water conditions [137]. TetraMin flocked feed was given three times a day with automatic dispensing and supplemented with artemia and dried Mysis shrimp (First Bite Aquarium Foods, Lincolnshire, UK) once per day. Fertilized eggs were collected, placed in Petri dishes and kept in an incubator with the same light cycle and temperature settings as for adults. Larvae were fed with paramecium once per day. The developmental stage was determined and recorded as a function of days post fertilization (dpf) [138].

Because zebrafish is a valuable translational model for epilepsy research, I decided to use the pentylenetetrazole (PTZ) induced-seizure model. All chemicals were acquired from Sigma Aldrich. Electrophysiological recording of larvae was carried out in developmental

ages between 5 and 16 dpf using stainless steel electrodes with 125 μm diameter. In order to allow manipulation, all animals were anesthetized in 0.002% tricaine and 10 μM d-tubocurarine, then immobilized on 1.2% concentration low-melting agarose and positioned ventrally in a Petri dish, so that the dorsal side of the animal is facing upward. The electrode positioning was performed with the aid of a binocular loupe and a triaxial micro-manipulator setup, always installing the electrode in the tectum opticum of the larvae.

Pentylenetetrazole (PTZ) was applied at 30 mM concentration to the bath and each animal was kept up to 30 minutes exposed to this convulsing agent. I obtained data (video and electrophysiology) from a total of 20 larvae.

5.2.2 Electrophysiology and Videotaping

The electrical signal was pre-amplified (C3313/RHD2216, Intan Technologies LLC) and filtered from 1 to 1000 Hz; the data were then amplified by a commercially available C3100/RHD2000 Evaluation System (Intan Technologies LLC), to a final gain of 1000. Recordings were performed in one channel with samplerate set at 10k samples per second.

Video was acquired simultaneously with the electrophysiological recordings by an Opticam attached to the microscope (see Fig. 5.1 for picture of the setup and schematic). Video resolution was 1024 x 768 and frame rate was around 3.7 frames per second. The frame rate varied between 3 and 4 frames per second, which was determined through hardware and could not be controlled by the software.

Electrophysiological recordings were analyzed using Matlab (Mathworks, Natick, MA) by subsampling raw data to 1 kHz (down from 10 kHz), filtering from 1 to 50 Hz, and visualizing signals over time. Synchronization with the video was performed manually by recording the last second of the file for the video and the electrophysiological signals. The Intan recording software includes timestamps on the electrophysiological recordings that were taken from the computer's operating system. The video files were also recorded by the same computer, and thus provided timestamps which were within 0.5 sec of the Intan file timestamps. I therefore report here signals (video and electrophysiology) that were

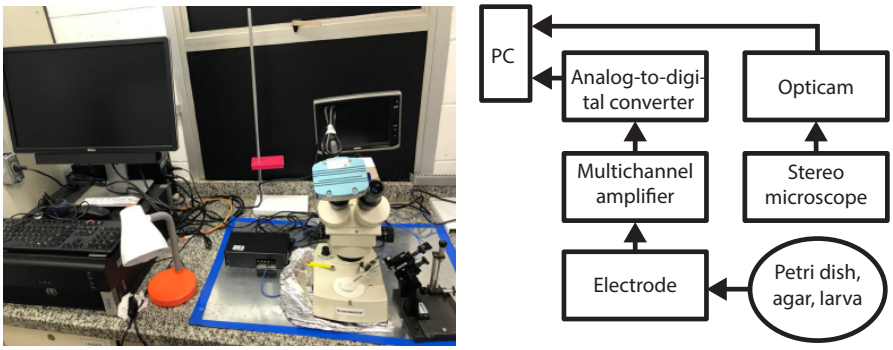

Figure 5.1: Experiment setup. (a) Setup for electrophysiology and image acquisition. (b) Flowchart of the data recording setup.

synchronized to be within 0.5 sec.

The average heart rate for a control zebrafish larva is 2 to 3 beats per second [127], whereas the average heart rate of an animal treated with drugs may increase or decrease depending on the drug used [129]. In the proposed experiments, the mean heart rate for the treated zebrafish embryos was about 1.2 beats per second, as validated by electrocardiographic data. According to the Nyquist sampling theorem, the signal must be sampled at least twice the highest frequency contained within the signal to avoid aliasing. In our case, the minimal video capture frequency must be at least 2.4 Hz. The video frequency met this requirement and was sufficient for capturing the expansion and contraction motion of the heartbeat. One advantage of collecting video at a relatively low temporal frame rate is that redundant frames are avoided and processing time is reduced because only key frames of body deformation correlated with heart expansion and contraction were recorded.

5.2.3 Z-HRAM Algorithm and ROI Selection

The flowchart of the proposed low-cost heart rate detection method is presented in Fig. 5.2. The Z-HRAM algorithm mainly consists of four steps: 1) Given input zebrafish image sequence, region of interest is identified around the larva's body in the input image sequence. 2) For two continuous image frames (previous and current frames), a multi-resolution dense

optical flow method is applied to estimate the dense motions. 3) The estimated motions are then mapped to zebrafish body expansion and contraction movements, which are correlated with heartbeats. 4) The principle deformation and heartbeats are determined through principal component analysis. To validate the proposed method, I compared its results with EKG measurements. I also compare its accuracy and performance with manual tracking and one published method on automatic detection of zebrafish heartbeat [135].

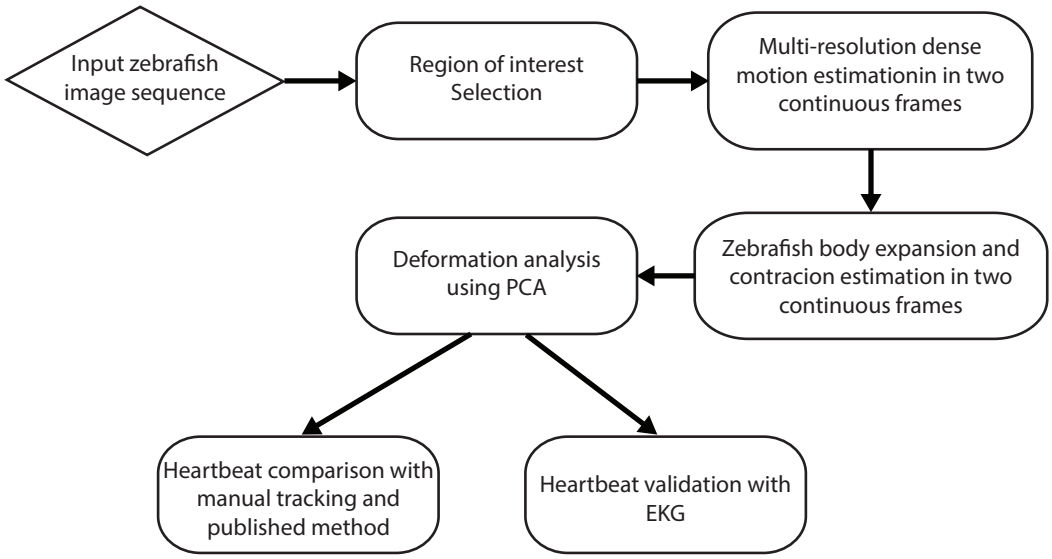

Figure 5.2: Flowchart of the Z-HRAM algorithm.

There are two major steps (Algorithm 1). One is the tracking of the local deformation determined by comparing two consecutive frames by the Farneback method [139]. This step estimates dense optical flow with high accuracy. The second step is on applying principal component analysis to identify the main deformation direction.

The challenges of heartbeat detection from tracking zebrafish larvae body motion include small motion magnitude and low signal-to-noise ratio (see Fig. 5.3). Electrophysiological recordings are often performed on the larvae in studies using the seizure-induced model [125, 128, 140]. As mentioned previously, during these recordings, the larvae can only be positioned upright due to the electrophysiological recording requirements. Because direct

Algorithm 1: Zebrafish heart rate automatic method (Z-HRAM)

```
Select region of interest (ROI)
Compute and visualize local deformation on ROI using multi-resolution
dense optical flow
for t = 1 to N - 1 // iterate all video frames
    Compute multi-resolution images using Gaussian pyramid
    for l = L, L-1, ... , 1, 0 // iterate multi-resolution levels
        Compute motion vector d_t^l between image I_t^l and I_{t+Δt}^l at
        multi-resolution level l
        Propagate the d_t^l to level l - 1
    end
end
Detect heart rate using principal component analysis (PCA)
```

observation of heart movement cannot be performed when the larva is positioned ventrally, I propose that indirect heartbeat observation can be performed through detection of the larva's body deformation.

Based on observation of the collected larva recordings and analysis of zebrafish anatomy, I identified a region consistently displaying periodic movement of the larva's body. The deformation is located near the edge of the swim bladder, a region with a vascular network that includes the posterior aorta [141, 142]. By comparison of the visual deformation with corresponding electrophysiology data, I conclude that epithelium deformation is a consequence of the larva heartbeat and can be used as a robust biomarker to infer heartbeat. The motion of the region of interest was determined semi-automatically. I first identified the swim bladder region which resembles an ellipse from the dorsal view. Ellipse fitting [143] was applied to identify the initial elliptical region (red curve in Fig. 5.3). The bounding box around the ellipse was then calculated (yellow in Fig. 5.3). Based on zebrafish anatomy and observation, the consistently periodic movement mainly happens around the lower boundary of the swim bladder. The final regions of interest were as two rectangles subdivided from the bounding box (purple and cyan regions in Fig. 5.3) inside the swim bladder. For the few recordings from larvae whose swim bladders did not closely resemble an ellipse, I defined

the region of interest manually.

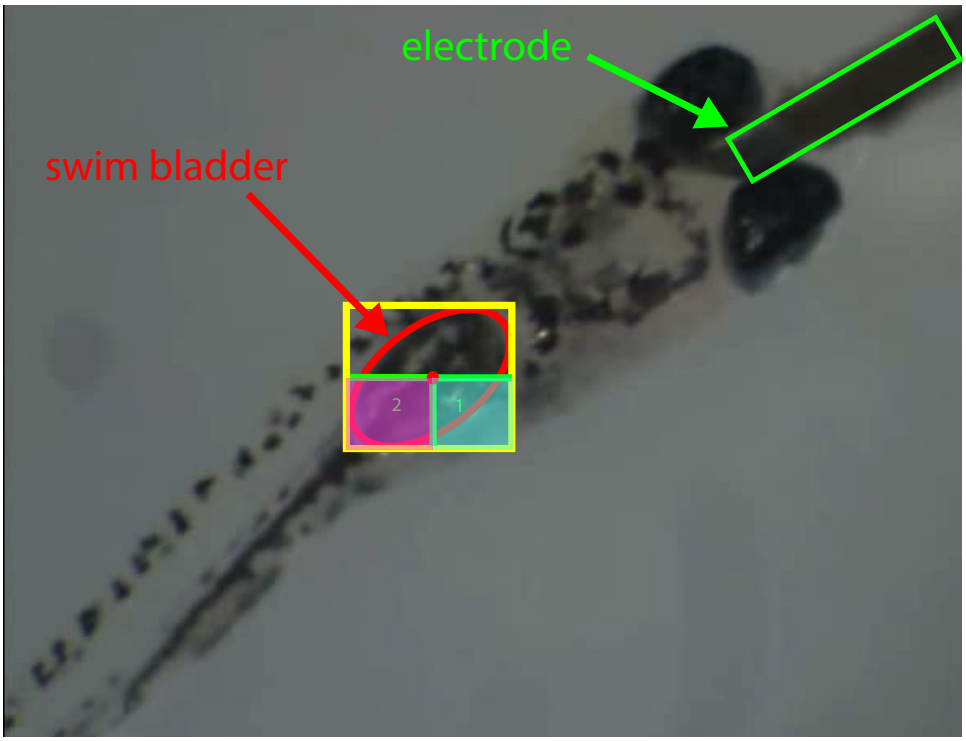

Figure 5.3: In the first frame of the video, the regions of interest that encode motion were determined near the swim bladder. The electrode was positioned on the top right. Larva was ventrally positioned for electrophysiological recording. Yellow rectangle indicates the bounding box. Red ellipse outlined the swim bladder. Cyan and pink rectangles are the automatically selected regions of interests.

5.2.4 Body Deformation Detection and Visualization

The contraction and expansion movements of the larva heart were tracked by measuring the deformation in the zebrafish body by applying the dense optical flow method [139]. Dense optical flow is a technique that can estimate motion of an object from two image frames recorded at consecutive timestamps. It has been widely used in motion detection, object tracking and depth estimation. The dense optical flow method first approximates the intensity of each pixel by its neighborhood Ω with a quadratic function and computes its coefficients between frames. The size of the pixel neighborhood Ω determines smoothness of

the image. Large Ω yields smoother motion. Let $f_t(\mu)$ be an intensity of pixel at coordinate $\mu = (\mu_x, \mu_y)$ at frame t. Then $f_t(\mu)$ is approximated by solving a weighted least-squares fit to a quadratic function of the neighbor pixel intensities:

$$f_t(\mu) = \mu^T A_t \mu + b_t^T \mu + c_t \tag{5.1}$$

where A_t is a symmetric matrix, b_t is a vector, and c_t is a scalar. These coefficients are estimated from the weighted least squares fit to the pixel value in the neighborhood. Let d be a motion vector between frame t and $t + \Delta t$. Then the relationship between intensity $f_t(\mu)$ and intensity $f_{t+\Delta t}(\mu)$ can be expressed as:

$$\begin{aligned} f_t(\mu) &= f_{t+\Delta t}(\mu + d) \\ &= (\mu + d)^T A_{t+\Delta t}(\mu + d) + b_{t+\Delta t}^T(\mu + d) + c_{t+\Delta t} \\ &= \mu^T A_{t+\Delta t}\mu + (b_{t+\Delta t} + 2A_{t+\Delta t}d)^T \mu + d^T A_{t+\Delta t} d + b_{t+\Delta t}^T d + c_{t+\Delta t} \end{aligned} \tag{5.2}$$

The coefficients of the quadratic functions in Equations 5.1 and 5.2 are equated:

$$A_t = A_{t+\Delta t} \tag{5.3}$$

$$b_t = b_{t+\Delta t} + 2A_{t+\Delta t}d \tag{5.4}$$

$$c_t = d^T A_{t+\Delta t} d + b_{t+\Delta t}^T d + c_{t+\Delta t} \tag{5.5}$$

The motion vector can be expressed as a function of the coefficients by rearranging terms in Equation 5.4:

$$d = -\frac{1}{2} A_t^{-1}(b_{t+\Delta t} - b_t) \tag{5.6}$$

Since the locally approximated intensities in the neighborhood are not the exactly the same between frames t and $t + \Delta t$ due to local deformation, Equation 5.3 does not always hold in practice. The average of A_t and $A_{t+\Delta t}$, $\hat{A}_t$ can be used to approximate the mean intensity of these two image frames:

$$\hat{A}_t = \frac{A_t + A_{t+\Delta t}}{2} \tag{5.7}$$

Then Equation 5.7 can be rewritten as:

$$\hat{A}_t d = \Delta b_t \tag{5.8}$$

where $\Delta b_t = -\frac{1}{2}(b_{t+\Delta t} - b_t)$.

In theory, I can apply Equation 5.8 to estimate the motion vector d for each pixel, but the motion vectors were shown to be too small and noisy due to inconsistent correspondence found for each pixel. Therefore, I take advantage of the fact that the motion vectors vary gradually and smoothly across the small neighborhood Ω of each pixel and integrate local motion vectors over the neighborhood region Ω for each pixel. Specifically, I would like to estimate a motion vector d which is smooth over Ω for each pixel through minimizing the following energy function:

$$E(d) = \sum_{\Delta\mu \in \Omega} w_{\Delta\mu} ||\hat{A}_t(\mu + \Delta\mu)d - \Delta b(\mu + \Delta\mu)||^2 \tag{5.9}$$

where $w_{\Delta\mu}$ is a weight function of pixel μ in the neighborhood. Fig. 5.4 demonstrates the influence of the neighborhood size $\Omega = 1, 2, 4, 8, 16$ on the estimated motion vector d. Within pixelwise motion vector estimation $\Omega = 1$ (Fig. 5.4 (a) left), the motion vector turns to be too small and noisy (Fig. 5.4 (a) right). The motion vectors get smoother when Ω increases (Fig. 5.4 (b)-(e)), demonstrating the advantage of introducing the additional energy function.

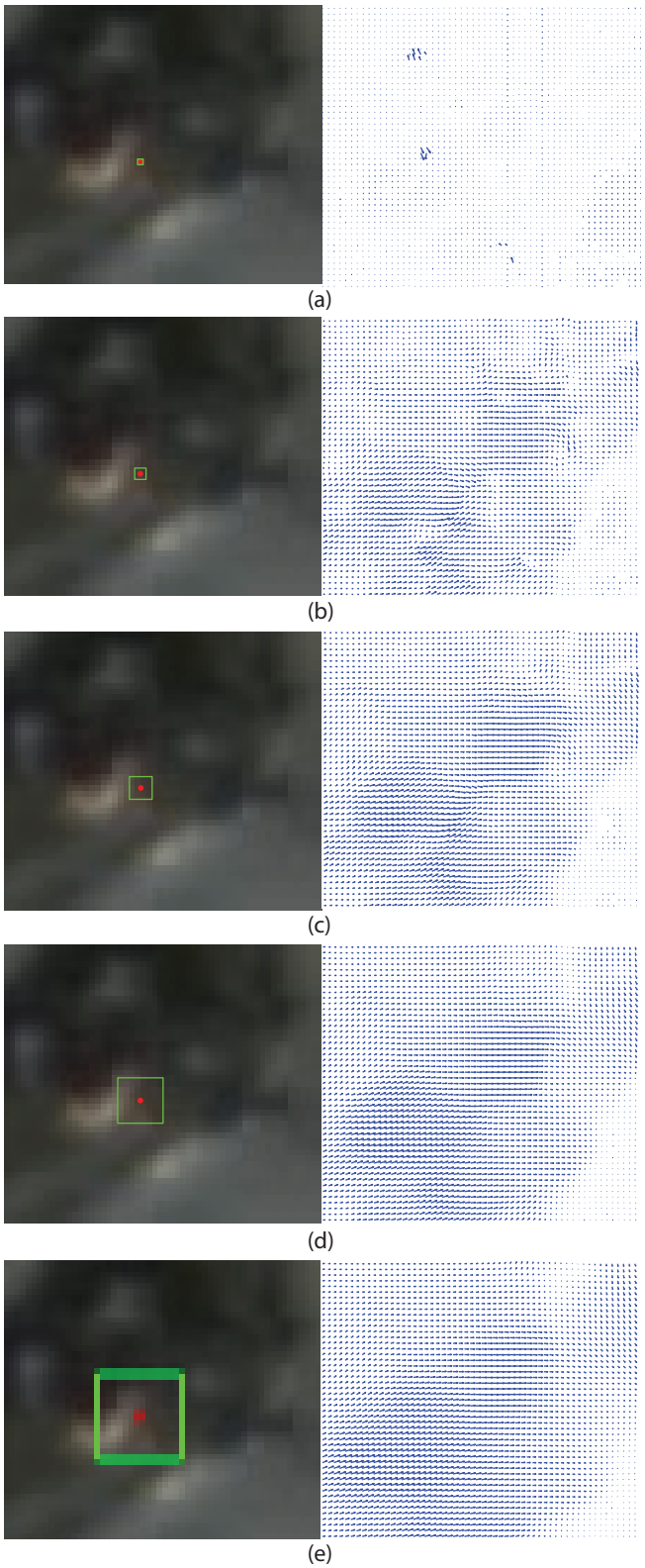

Figure 5.4: Motion vectors estimation with different neighborhood size Ω. (a) $\Omega = 1$, (b) $\Omega = 2$, (c) $\Omega = 4$, (d) $\Omega = 8$, (e) $\Omega = 16$. The motion vectors tend to be small and noisy when Ω is small and become smoother as Ω increases.

To increase the accuracy and robustness of motion estimation, multiscale analysis technique has been widely applied in problems dealing with image processing [144]. Here I applied the pyramidal optical flow method [145], which uses dense optimal flow in a multi-resolution scheme. In each step, the image was down sampled by half in resolution, which also reduced each pixel displacement by half. In order to overcome the artificial edges during image down sampling, Gaussian kernel was applied and a Gaussian pyramid was built for each image frame I_t at timestamp t (Fig. 5.5). The number of levels of resolution can be specified for the desired motion magnitude. In our study, two levels of resolution were sufficient for dense optical flow tracking. Further down sampling would be redundant as the image resolution at the top level would be very low. The original image data served as the lowest level in the pyramid and was denoted as I_t^0 . The image in each level l was the sub-sampled image of the adjacent lower level image $l-1$:

$$\begin{aligned} I_t^l(\mu_x,\mu_y) = \frac{1}{4}I_t^{l-1}(2\mu_x,2\mu_y) + \frac{1}{8}(I_t^{l-1}(2\mu_x-1,2\mu_y) + I_t^{l-1}(2\mu_x+1,2\mu_y)+ \\ I_t^{l-1}(2\mu_x,2\mu_y-1) + I_t^{l-1}(2\mu_x,2\mu_y+1)) + \frac{1}{16}(I_t^{l-1}(2\mu_x-1,2\mu_y-1)+ \\ I_t^{l-1}(2\mu_x+1,2\mu_y+1) + I_t^{l-1}(2\mu_x-1,2\mu_y-1) + I_t^{l-1}(2\mu_x+1,2\mu_y+1)) \end{aligned} \tag{5.10}$$

A top-down dense optical flow motion tracking was performed on the image pyramid. For each pyramid level $l = 1, ..., L$, define the corresponding position μ^l for a point μ^0 in the pyramidal image I_t^l. μ^0 is point in image I_t^0. Based on the pyramid representation, vector μ^l on level l is computed as follows:

$$\mu^l = \mu^0/2^l \tag{5.11}$$

Motion tracking started from the highest level L. A motion vector d^L can be computed from I_t^L and $I_{t+\Delta t}^L$ using dense optical flow. d^L was then projected onto the finer image I_t^{L-1}

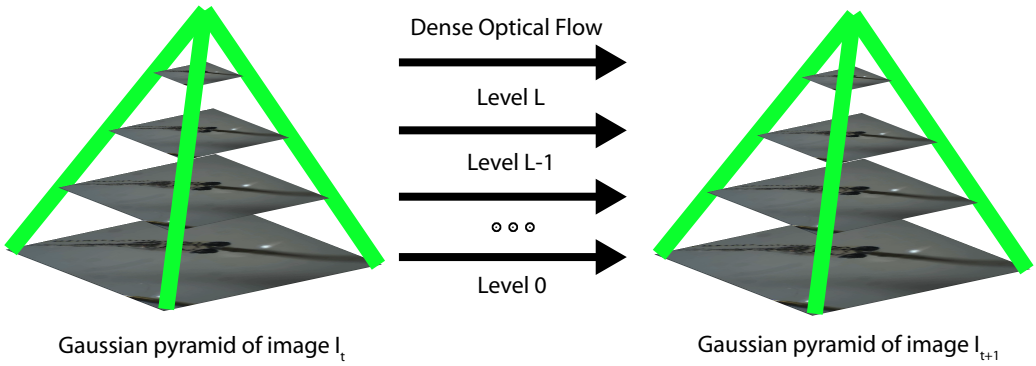

Figure 5.5: Multi-resolution dense motion estimation using Gaussian pyramid. Each level in the pyramid is a sub-sampled image of the lower level. The dense optical flow between the top level images I_t^L and I_{t+1}^L is computed. Then, the coarse-level dense optical flow is projected onto the lower finer pyramidal level image and continue this at each level until the original image level (level 0) is reached.

as an initial pixel displacement in the lower level $L-1$. Dense optimal flow was applied between pyramidal images I_t^{L-1} and $I_{t+\Delta t}^{L-1}$ on level $L-1$ to refine motion vectors d^{L-1} on this level. d^{L-1} was then propagated to image level $L-2$ and so on, until the original image I_t^0 was reached. To visualize contraction and expansion deformation in the body region, I computed the dense motion vectors for all pixels in the region of interest using the approach described above. The motion vectors were then mapped to the RGB color space (Fig. 5.6 and Fig. 5.7). Motion image in Fig. 5.6 (d) demonstrated body expansion between two continuous frames in Fig. 5.6 (a) and (b). The motion vectors that have similar motion direction and magnitude in Fig. 5.6 (c) were associated with similar colors in the motion image in Fig. 5.6 (d), implying pixels of similar color underwent similar deformation. Similarly, Fig. 5.6 (g) and (h) illustrated the body contraction motion vectors and color image between two continuous frames in Fig. 5.6 (e) and (f). Having the same spatial resolution as the images in the video recordings, the motion images were able to clearly visualize expansion and contraction of the body. After computing pixel-wise motion images of all images in the video recording, zebrafish body deformation frequency can be

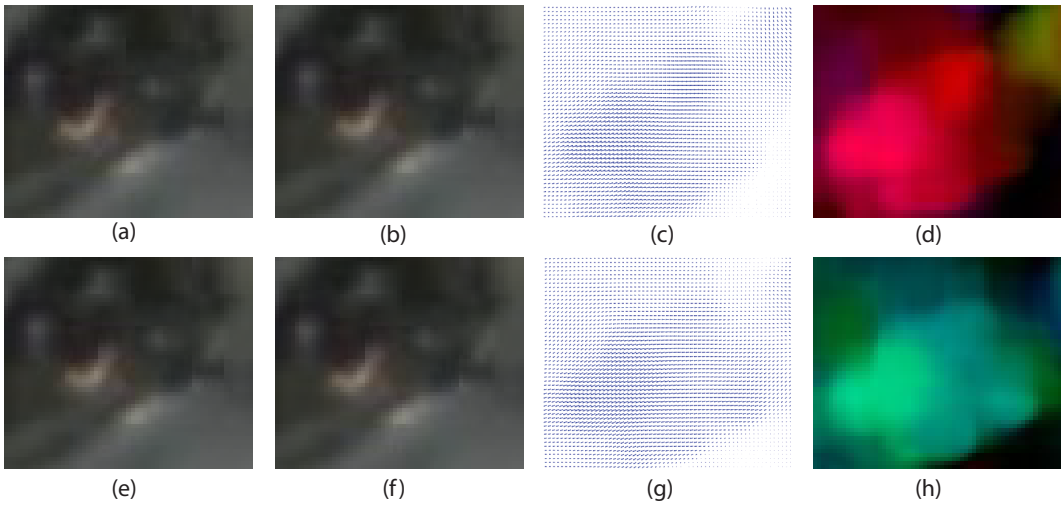

Figure 5.6: Illustration of dense optical field. (a), (b) zebrafish body expansion in two continuous frames. (e), (f) zebrafish body contraction. (c), (g) and (d), (h) are two different ways to visualize the dense optical flow fields. In (c) and (g) expansion and contraction motion fields are visualized as motion vectors on the dense grid. For deformation with large magnitude it is hard to visualize. In (d) and (h), expansion and contraction deformation is visualized via the color-coding method as in Fig. 5.7.

associated with the heartbeat.

5.2.5 Heart Rate Detection using Principal Component Analysis

As described previously, the localized deformation of the zebrafish body is a consequence of the heartbeat. The heart motion calculated from dense optical flow has many local variations in different orientations and magnitudes (Fig. 5.6 (d) (h)). Possible reasons for these local variations include low image resolution, low imaging frequency and the lack of texture features. In order to properly assess the deformation in relation to heartbeat, the main direction of tissue deformation inside the region of interest needs to be determined. To achieve this goal, I first converted motion vectors from the Cartesian coordinate system into the polar coordinate system (Fig. 5.8 (a)) so that the motion vectors can be directly characterized by their orientations and magnitudes. The orientation and magnitude components represent distinct information of deformation, which implies expansion (Fig. 5.6 (d) and Fig. 5.8 (a)) and contraction (Fig. 5.6 (h) and Fig. 5.8 (b)) of the zebrafish body. Next,

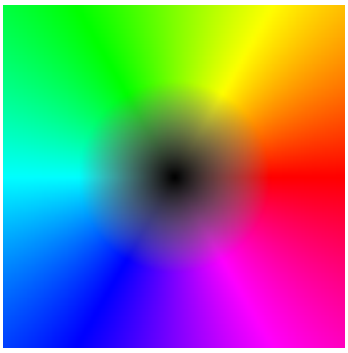

Figure 5.7: Color scheme used to represent the optical flows. The orientation of each motion vector is mapped to hue and the magnitude is mapped to saturation. It is the standard scheme in dense optical flow visualization that enables visualization of the local deformation for all pixels in the image.

I apply principal component analysis (PCA) to find the major deformation direction while ignoring local deformation caused by suboptimal image quality (Fig. 5.8 (b)). PCA is a commonly used method for dimensionality reduction. It applies orthogonal transformation to map the original data onto principle components, which are linearly uncorrelated to each other. The first principal component with the maximum eigenvalue captures the majority of the variation.

For m motion vectors d_i, $i = 1, ..., m$ converted in the polar coordinate system p_i (Fig. 5.8 (a)), the covariance matrix is formulated as:

$$\Sigma = \frac{1}{m}\sum_{i=1}^{m}(p_i - \bar{p})(p_i - \bar{p})^T \tag{5.12}$$

where $\bar{p}$ is the mean motion polar coordinate. Two eigenvalues (λ_1, λ_2) and the corresponding eigenvector (v_1, v_2) were calculated using Singular Value Decomposition. The main deformation direction was identified by finding the eigenvector with the larger eigenvalue. Fig. 5.8 (b) demonstrates eigenvectors during body expansion and contraction. The main deformation direction was the one with the long axis. If the two eigenvectors have opposite main deformation directions (angle between the two directions larger than 90°),

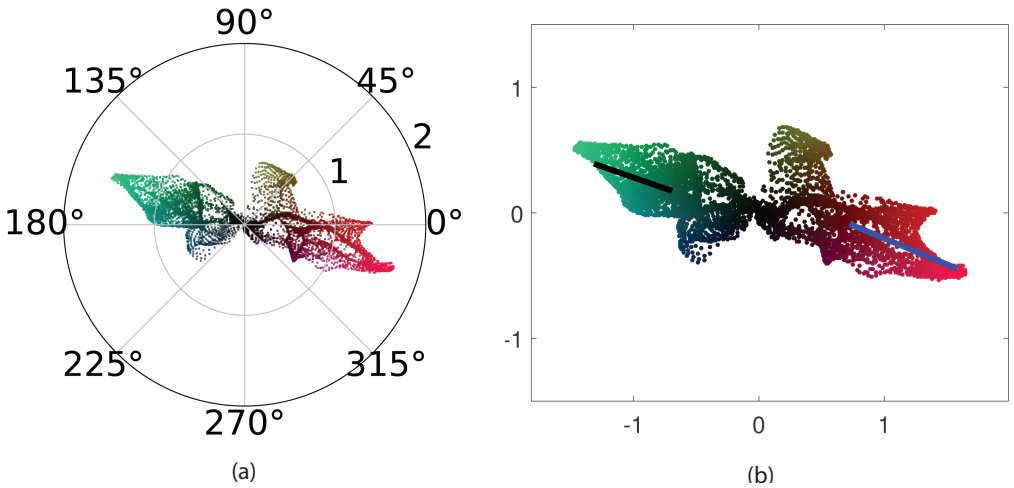

Figure 5.8: Deformation analysis in continous frames. (a) Expansion (as in Fig. 5.6 (d)) and contraction (as in Fig. 5.6 (h)) deformation fields are represented in the polar coordinate system for two continuous frames. (b) Main deformation fields (blue and black axes) were detected for the expansion and contraction deformation fields respectively using PCA.

this indicates one heartbeat (a pair of expansion and contraction). Otherwise if the deformation continues along one general direction (angle between the two directions smaller than 90°), this indicates a continuation of one expansion or contraction movement. Given the main deformation direction for each frame, the heart rate was calculated by counting the number of eigenvector pairs with opposite main deformation direction in the continuous frames. Fig. 5.9 demonstrates continuous expansion and contraction deformation in the region of interest over 2 seconds.

The proposed Z-HRAM can identify the larva body as ROI and track localized larva body deformation. This deformation is highly correlated with heart movement. Multi-resolution dense optical flow-based motion tracking guarantees a smooth motion vector estimation over small region. Principal component analysis identifies expansion and contraction pattern that is used to determine heartbeats. Z-HRAM can detect and track the heartbeats of immobilized, ventrally-positioned zebrafish larvae without direct larva heart observation. Another advantage of Z-HRAM is well suited for the analysis of low resolution and low frequency image data.

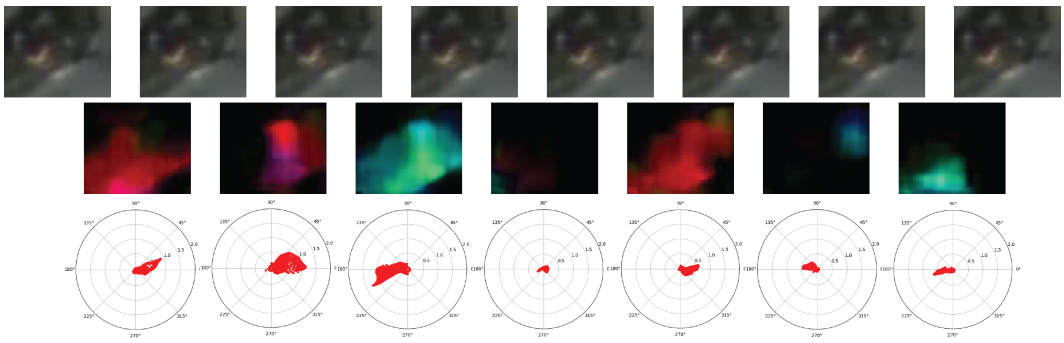

Figure 5.9: Continuous expansion and contraction deformation in the regions of interest over continuous frames.

5.3 Results and Validation

In order to validate the proposed heartbeat tracking method, I compared results from Z-HRAM to a previously published automatic zebrafish heartbeat detection method by Pylatiuk et al. [135] and two manual tracking results in a number of video segments. A custom Matlab program with Graphic User Interface (GUI) was implemented to allow for manual tracking, frame-by-frame, of the deformation. Two unbiased researchers tracked the deformation using the Matlab program, and their results were then compared to the automated detection results.

By correlating the electrocardiographic (EKG) signal to the manual tracking results, I confirmed that the examined motion corresponds to the contraction and relaxation of the heart and that swim bladder tracking is a feasible method to infer heartbeats from the dorsal view. It should be noted that this method (visualization of periodic movement of the swim bladder) is also traditionally used in laboratory settings during experimental sessions to ascertain that the animal is alive.

In Fig. 5.10, I show an example of the heartbeat detected by EKG and Z-HRAM over 10 seconds. Six heartbeats were detected from both the EKG signal and Z-HRAM applied to the video signal acquired simultaneously with the EKG. Fig. 5.10 also shows that the heartbeats were detected by both methods at similar time instances, with a maximum error

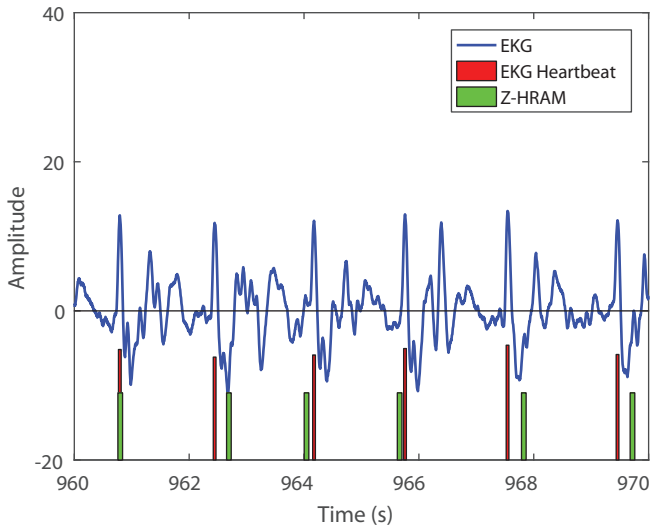

Figure 5.10: Comparison of the timing in heartbeat over 10 seconds using EKG (red) and Z-HRAM (green).

of 0.28 seconds. It should be noted that the amplitudes shown by the green and red bars do not mean any physical quantity (they are arbitrary units). Here I are concerned mainly with the time stamps for each heartbeat, and not with the size of the beat, as this is unrealistic to expect only from the swim bladder vascular movement. Table 5.1 presents heartbeats detected from EKG and Z-HRAM on three different trials of different durations (20, 10, and 8 seconds respectively). In each trial, the number of heart beats estimated by Z-HRAM was consistent with the EKG data, demonstrating accuracy of Z-HRAM.

Table 5.1: Comparison of number of heartbeats measured from EKG and Z-HRAM

Trial	EKG	Z-HRAM
1	10	10
2	6	6
3	5	5

The heartbeat counts from 20 video trials were analyzed. Fig. 5.11 shows comparison of

results from researchers (Manual 1 and Manual 2), method by Pylatiuk et al. [135], and Z-HRAM. Results from Z-HRAM were mostly consistent to the manual tracking results. The mean error between Z-HRAM and manual tracking is 1.3 heartbeats in 20 trials over 545 seconds in total. The mean error between the results from method by Pylatiuk et al. [135] and the manual tracking is 7.78 heartbeats in 20 trials. The detection rate of Z-HRAM is 99% over 545 seconds. Pearson's correlation coefficient between manual and Z-HRAM results, and between manual and Pylatiuk et al. results were 0.99 and 0.79 respectively. A linear regression was performed between the results from the two automatic methods and two manual tracking results. As shown in Fig. 5.12 and Table 5.2, a high linear correlation between Z-HRAM and two manual results are obtained ($R^2_{Z-HRAM_{Manual}} = R^2_{Z-HRAM_{Manual2}} = 0.99$). The correlation between the results from the method by Pylatiuk et al. and two manual results are much lower ($R^2_{PIVM_{Manual}} = 0.66, R^2_{PIVM_{Manua2}} = 0.63$). In summary, Z-HRAM outperforms the other automatic heartbeat detection method by Pylatiuk et al. in terms of heartbeat detection accuracy. The main reason is that method developed by Pylatiuk et al. counts the heartbeat by calculating the local intensity variation of the heart region in lateral view, which allows for visualization of the heart movement directly. The images (from that paper and with that method) show significant intensity variation during heart expansion and contraction. However, from the dorsal view (Fig. 5.2), the larva's heart components are entirely obscured, preventing direct observation of the heart, and local intensity variation is the smaller than that in direct heart observation. Moreover, the method by Pylatiuk et al. leverages local maxima detection method on the periodic heartbeat curve to the count the number of heartbeats. The recorded video for such method therefore needs to be acquired in high frequency (30 frames per second). Given the low sample rate (i.e. lower than 5 frames per second), I expect many of the previously published methods [129, 134, 135] for heartrate detection to either not be applicable or to underperform when tested under the dorsal view constraints.

I compared the computational time of Z-HRAM to manual tracking and to the previously

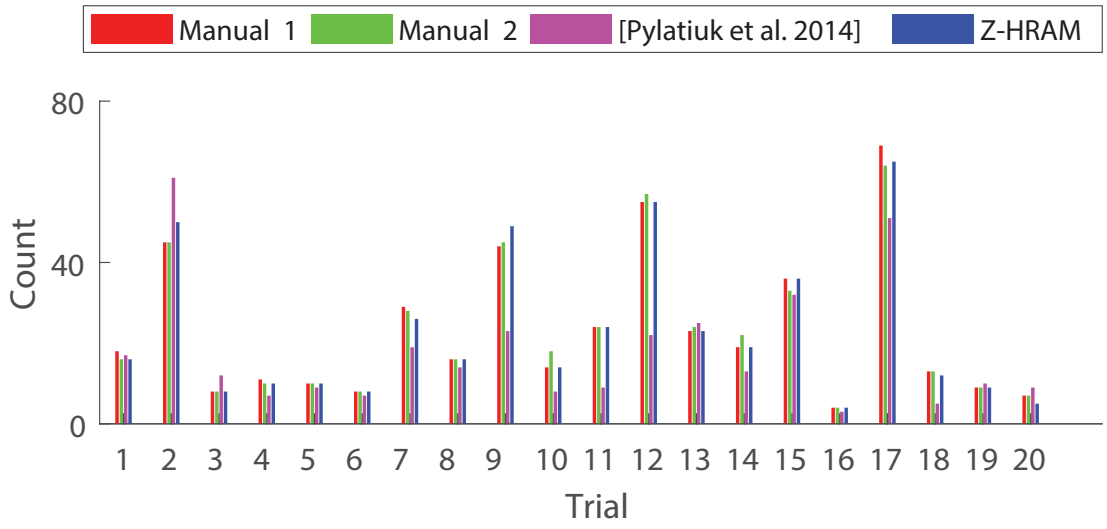

Figure 5.11: Comparison of correlations of the two heartbeat detection methods, Z-HRAM and the method by Pylatiuk et al., to the two manual tracking results.

Table 5.2: Comparison of linear correlation between algorithm and manual results

Algorithm vs. Manual	Linear coefficient	R^2 score
Pylatiuk et al. 2014 vs. Manual1	$y = 0.69x + 1.96$	0.66
Z-HRAM vs. Manual1	$y = 1.01x - 0.44$	0.99
Pylatiuk et al. 2014 vs. Manual2	$y = 0.69x + 1.93$	0.63
Z-HRAM vs. Manual2	$y = 1.04x - 1.12$	0.99

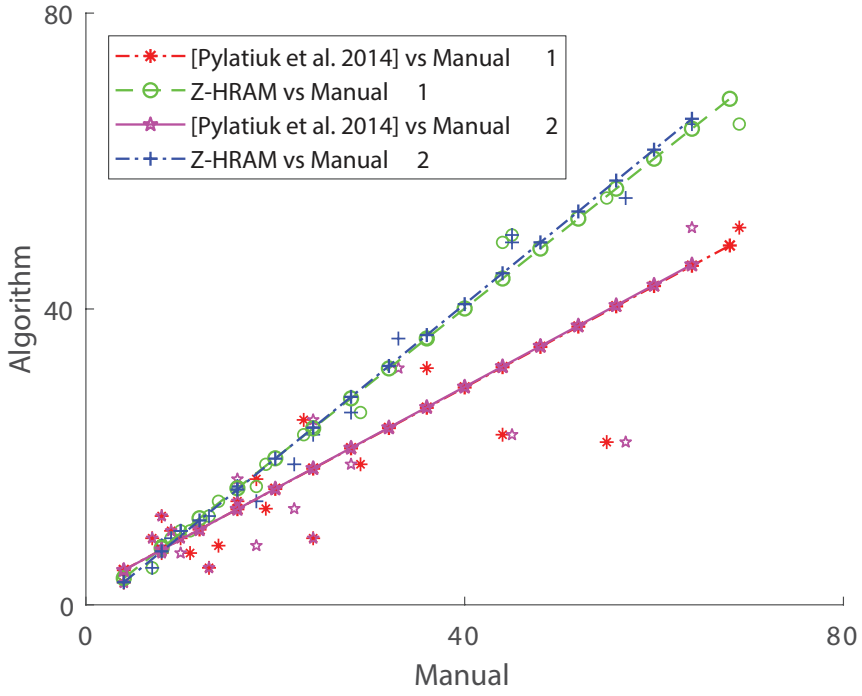

Figure 5.12: Heartbeat count comparison among manual tracking, Z-HRAM, and the method by Pylatiuk et al. X axis represents number of heartbeats counted using manual tracking through 20 video trials. Y axis represents number of heartbeats measured through proposed method Z-HRAM and method by Pylatiuk et al. for the corresponding trial.

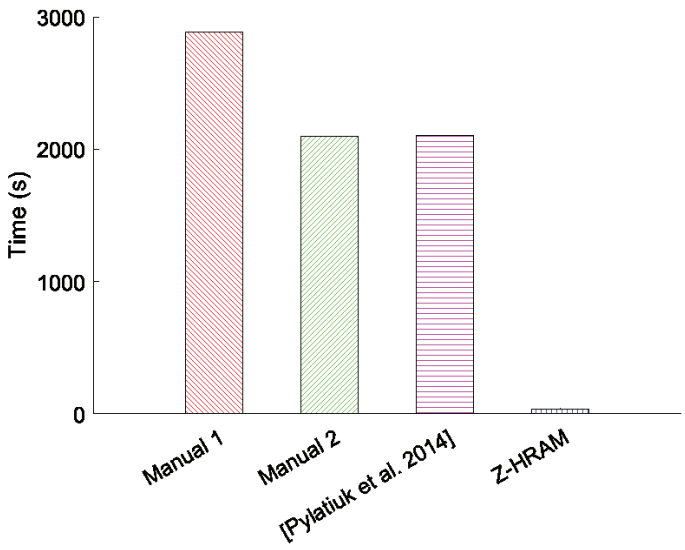

Figure 5.13: Computation time of manual heartbeat tracking, Z-HRAM and the automatic tracking method by Pylatiuk et al. Z-HRAM is 80 times faster than the first researcher (manual 1) and 60 times faster than the second researcher (manual 2) and previous work by Pylatiuk et al.

published method [135], as I consider these the state-of-the-art for heartbeat detection in zebrafish. As Fig. 5.13 shows, Z-HRAM is at least 60 times faster than manual tracking and the method by [135], which demonstrates Z-HRAM's advantage in significantly reducing processing time on similar video data.

5.4 Discussion

Given the high correlation for the three methods of heartbeat detection (EKG, manual heartbeat tracking, and Z-HRAM), I have demonstrated a robust method to automatic zebrafish heartbeat detection in ventrally-positioned larvae without performing direct observation of the larva heart. The multi-resolution dense optical flow motion tracking approach is able to adequately capture even minimal local expansion and contraction of a zebrafish body deformation when applied on low resolution and low frame rate (3-4 fps) video data.

Thus, Z-HRAM is capable of supplementing experiments that utilize low-cost camera configurations, making it an accessible tool for most labs. In regards to efficiency, Z-HRAM is many times faster than manual video analysis and then the method described in [135]. Z-HRAM requires minimal input from the user for cases when automatic region of interest identification is not feasible.

The most prominent limitation of Z-HRAM is the need for visible deformation. This limitation is common in video analysis: if there is a video with no deformation visible, then no heartrate will be detected (even manually by researchers). In periods where no deformation is visible, no algorithm will be able to detect any heart movement or heartrate. The larvae used in this study were between 5 and 16 days post fertilization. I believe this age range is reasonable for any research involving individual larvae. I are aware, however, of the need for experiments with younger animals. In the future I intend to adapt Z-HRAM to such larvae, in which the swim bladder is not fully developed and the blood vessel deformation may be different. The accuracy of the proposed algorithm in determining the beat-to-beat intervals depends directly on the frame rate. In the 3 to 4 fps videos that were tested, the max beat-to-beat interval error was 0.27 seconds, as expected. Lastly, the proposed algorithm is currently limited to detecting heart rate and beat-to-beat intervals. While other methods require the lateral or ventral view, they are able to perform more exhaustive analyses of larva cardiac function since they can directly observe the deformation of the heart chambers.

The motion region of interest located on the larva's body. Considering the priori anatomy knowledge of the larva's body, I outlined the ROI semi-automatically. To improve efficiency, an automatic method for ROI extraction could be integrated through image segmentation. The spectral method constrained by Bayesian inference was widely used for noisy medical image segmentation. This method could outline boundary over image with noisy and incomplete information among different modalities and tissues [146–148]. Bayesian inference could be introduced to estimate initial edge map of swim bladder [146–148]. The real boundary would be smoothed and refined through spectral method using probability

estimation. Finally, the current Gaussian pyramid based multiscale optical flow motion tracking method can successfully detect local motion vectors over swim bladder region, and this motion pattern is highly correlated with heartbeats. Through Gaussian pyramid and Equation 5.9, the estimated motion vectors vary gradually and smoothly across the small neighborhood of each pixel. To further understand various heartbeat behavior and movement characteristic when applying different drugs on zebrafish, I will integrate the multiscale wavelet decomposition method [146, 147] in future work, which would help us better understand how the heartbeat responding to different drugs.

5.5 Conclusion

As Z-HRAM produces a whole range of results such as indirect detection of the heart contraction and expansion, I anticipate its applicability to cardiac function and heartbeat pattern research in animal models where the heart chambers are not easily visible (through a stereoscope) or that cannot be recorded easily via any two-dimensional or three-dimensional imaging techniques.

I have combined two imaging algorithms and have demonstrated that the results can be readily validated on a subset of the signals acquired. For manual tracking of heartbeats, a researcher would need to invest roughly 137 seconds for each 30 seconds of video analyzed. It would not be feasible to fully analyze video recordings from 20 experiments (30 minutes each) without automation. Z-HRAM allows for unassisted detection of region of interest in video signals, tracking of even subtle motion direction (contraction/expansion), and automated counting of heartbeats, thus enabling analysis of heartbeat dynamics over longer experiments.

Chapter 6: A Real Time Haptic Simulator of Spine Surgery

The work presented in this chapter has been published in [149, 150].

6.1 Introduction

Spinal surgeries are volume complex and high-risk procedures [151]. The success rate of spine surgeries mainly depends on the skill of the surgeon. Computer-assisted systems used in operating rooms such as the surgical navigation system using 2D fluoroscopy [152] have been developed. However, the accuracy is very sensitive to various system errors and does not fundamentally improve skills of surgeons. Traditional spinal surgical training involves gaining knowledge through didactic sessions [153] and cadaveric dissection and practice. However, the high cost and shortage of cadavers prevent their frequent usage.

I present a real time haptic spine surgical simulator that will be used to train residents, fellows and spine surgeons in a hospital training program. It provides a realistic environment for the trainees to practice spine surgeries and has the advantages of being interactive, low-cost, representative, and repeatable over conventional training approaches. Haptic Phantom offers the users force feedback, differentiating the proposed system from other screenbased training systems. Computational efficiency was achieved by developing advanced graphical rendering methods. The volumetric data was classified into surface voxel cloud and inner voxel cloud by the adjacency graph which stored the relationship among voxels. To speed up the collision detection and real time rendering between the virtual surgical tools and the lumbar model, Octree-based algorithms and GPU technique were applied. To enhance the physical realism, three dimensional lumbar vertebrae models were reconstructed from CT images and associated with non-homogeneous bone density such that the rendered model best represents the spine anatomy and mechanics. I demonstrate system performance by

conducting pedicle screw insertion.

6.2 Related Work

Surgical training using virtual reality (VR) or augmented reality (AR) systems becomes commonly used to reinforce traditional training. For instance, studies showed that VR-based laparoscopic surgical training can improve the operative the performance of surgical trainees compared to no supplementary training and box-trainer training and reduce the actual operation time by 17-50% after training [154]. Training on a realistic VR-based arthroscopic knee surgical system resulted in a higher skill level in the operation room compared with the standard training [155]. Moreover, integrating a haptic device with a virtual simulator was successfully applied in training surgeons to conduct arthroscopic surgery [156] and neurosurgery [157] which were both shown to be effective and economical. Trainees learn and advance specific surgical skills through repeated interaction with the virtual anatomy and physically realistic biomechanical environment; training is no longer limited by cadaver resource.

Despite the development of many AR or VR-based surgical training systems, I were not able to find a suitable simulator for the proposed spine surgical training program. VR-based pedicle screw insertion simulators [158] provided visual feedback only so the users had no tactile feedback. Other haptic enhanced system is the ImmersiveTough system which does not incorporate bone mechanics and is lack of system validation [159, 160]. Here I present an interactive physically-based spine surgical simulator collaboratively developed by researchers, engineers and orthopedic surgeons. It provides a realistic virtual surgical environment augmented by instantaneous sense of touch of tool manipulation through haptics. The contributions of this paper are as follows:

- 3D anatomical model of the lumbar spine was automatically reconstructed from CT images. Local bone material density was derived from CT images to realistically model the inhomogeneity of lumbar vertebra mechanics and calculate haptic force feedback.

- Rather than a surface model, voxel-based model was applied to represent the lumbar vertebrae, which is physically more accurate for modeling heterogeneous lumbar properties and simulating surgical tool and tissue interaction.
- To achieve real-time simulation, I implemented surface reconstruction after collision detection on GPU.
- A data-driven nonlinear bone drilling force model was proposed, which more sensibly simulates the interaction between the surgical tool and the lumbar vertebrae.
- Patient-specific spine model reconstruction and surgery simulation can be achieved.

I demonstrate the performance of the proposed simulator through pedicle screw insertion shown in Fig. 6.1, which is a common spine surgery procedure associated with highly unpredicted perforation rate and malplacement rate [161]. The results show that the system is interactive, realistic and scalable. With more modules being developed, I envision the simulator not only to be used for training in the medical center in a few months but also for surgical planning and preoperative simulation, making an impact in improving spine surgical outcomes.

6.3 Method

6.3.1 Image Preprocessing and 3D Model Reconstruction

The 3D surface models of the lumbar vertebrae were first reconstructed from CT images (image size of 512 x 512 and pixel resolution of 1mm) in the Visible Female dataset [162]. The lumbar vertebrae were automatically segmented using thresholding and region growing algorithms (see Fig. 6.2(a)). A 3D model was built from the segmented regions. Due to imperfect image segmentation, structures other than the lumbar vertebra were present in the 3D model. The noisy points were removed by performing a statistical analysis on each points distance to its neighbors. Assuming a Gaussian distribution on the mean distances, points with distance greater or less than the global mean distance plus 0.5 times the standard

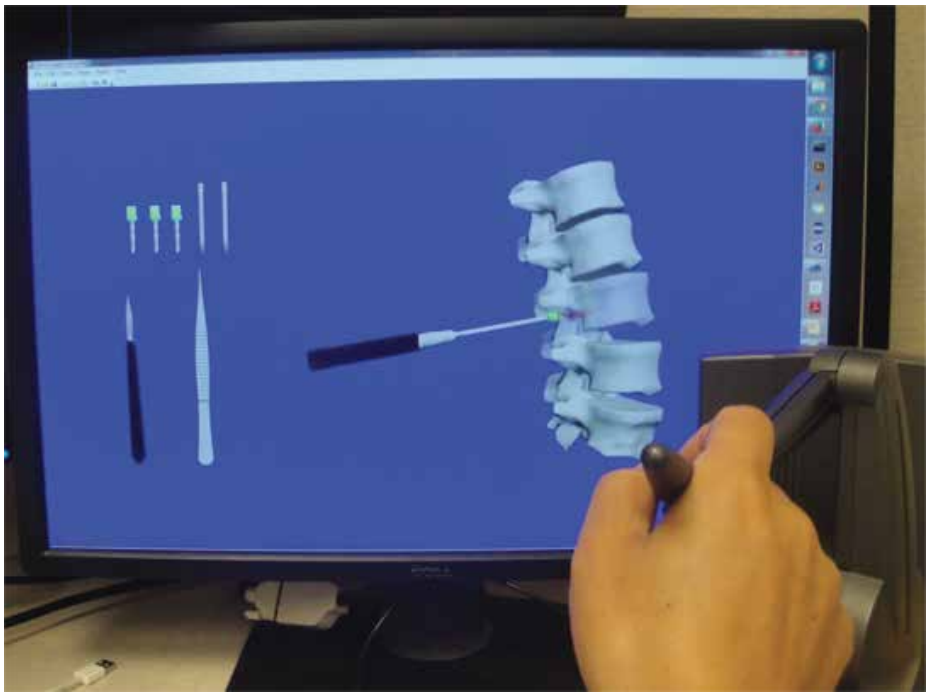

Figure 6.1: Through manipulating the Phantom, a user performs pedicle screw insertion and gets real time feedback.

deviation were identified as outliers and removed. Finally, a 3D polygonal surface model of each lumbar vertebra was reconstructed from the filtered lumbar point cloud using Marching Cube method (Fig. 6.2(b)).

6.3.2 Voxelization and Hybrid Data Structure

The bottleneck of an interactive surgical simulator is the computationally intensive physically-based simulation of tissue-tool interaction. Therefore, how to represent anatomical structures efficiently and how to simulate the physics behind virtual surgical procedures become the two primary technical challenges. I built a hybrid data structure that combines surface model shown as the grey outer surface and volumetric model shown as the blue cubes (Fig. 6.3(a)). The surface model shown in Fig. 6.2(b) was voxelized by applying the voxelization algorithm [163] (Fig. 6.3(b)). This structure guarantees the realism of continuous haptic interaction on the volumetric data (Fig. 6.3(a)) while maintaining the efficiency

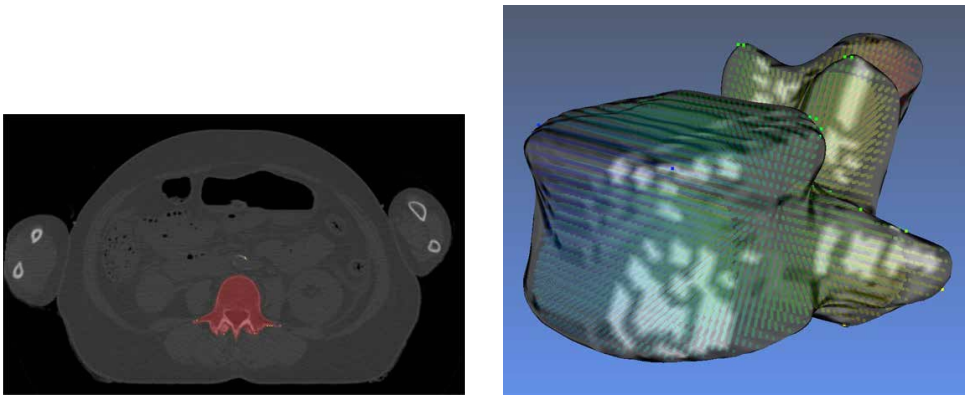

(a) (b)

Figure 6.2: (a) A lumbar vertebra shown in red segmented from CT images. (b) 3D surface model reconstructed from point cloud data.

and quality of surface rendering [164]. In order to provide accurate force feedback, the heterogeneity of bone mechanics in the lumbar vertebra was modeled in the simulator. Since significant correlation was found between CT image intensity and bone mineral density [165], I associated each voxel with the bone stiffness obtained from the corresponding image pixel, which clearly showed heterogeneity (Fig. 6.3(c)). Such geometric biomechanical modeling permits the generation of nonlinear mechanical force feedback as the haptic interacts with the model which was physically more realistic.

6.3.3 Adjacency Graph for Volumetric Data

Adjacency graph describes the relationship among voxels to ensure the efficiency and correctness in segmenting the volumetric data. I applied 26-adjacency graph which gives the highest accuracy (Fig. 6.4(a)). Voxel centers defined the surface point cloud and the inner point cloud shown in blue and red respectively in Fig. 6.4(b). These two sets of point clouds were used in surface reconstruction in each simulation step.

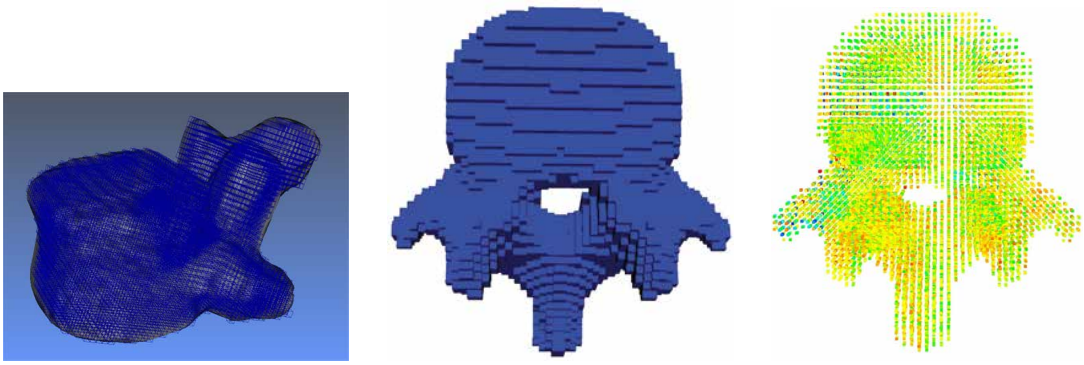

(a) (b) (c)

Figure 6.3: (a) Hybrid data structure consisting of volumetric data and surface mesh; (b) voxelied lumbar vertebra model; (c) nonhomogeneous bone mineral density.

6.3.4 Collision Detection

To detect collision between the surgical tool and the lumbar model, a computationally efficient octree-based algorithm was employed. The model was partitioned and organized into a 3D voxel space through recursive subdivision. Octree-based collision detection is widely used in simulation, because of its efficiency for voxel localization and neighbor search. Fig. 6.5(a) shows a lumbar vertebra embedded in an octree grid. The multi-resolution and hierarchical grid can be clearly seen. Depending on the contact location between the surgical tool and the lumbar, the leaf voxels were removed from the volumetric data shown in Fig. 6.5(b). The adjacency graphs of all the voxels that were neighbors of the contact voxels were updated for surface reconstruction.

6.3.5 Real Time Surface Reconstruction and Updating

To provide smooth visual feedback of drilling effect, the lumbar vertebra surface model needs to be reconstructed and updated in real-time from the post-collision voxel data. Directly applying Marching Cubes reconstruction from surface point cloud (blue points in Fig. 6.4(b)) generated a significantly large number of triangles. In addition, it led to surfaces with overlapped triangles and multiple layers because of the redundant surface

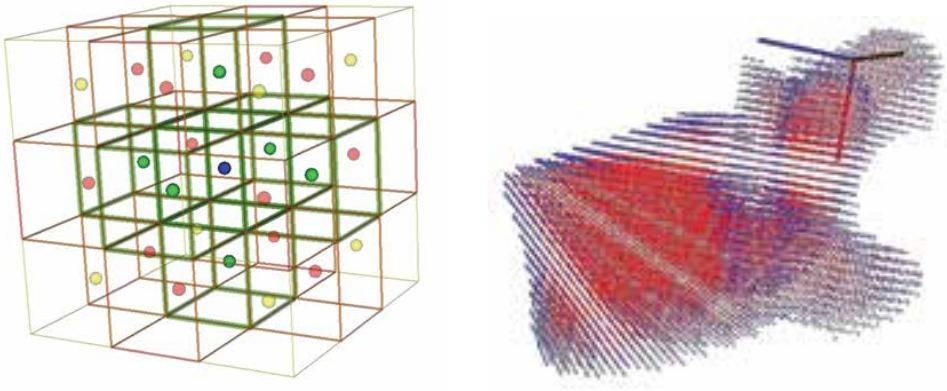

(a) (b)

Figure 6.4: (a) Adjacency graph of a pixel in blue; (b) surface point cloud in blue and inner point cloud in red.

voxels defined by the adjacency graph (see Fig. 6.6(a)).

In a 2D illustration in Fig. 6.6(b), Marching Cubes generated two layers, one connecting point from v1 to v8 and one connecting v9 to v17. To overcome this problem, I used an algorithm presented in [166] to extract a single surface from the duplicate triangle surfaces (see Fig. 6.6(c)). Fig. 6.7 shows the reconstructed surface after tool drilling shown in Fig. 6.5(b). The surface updating algorithm was implemented on GPU to take advantage of its parallel processing capacity.

6.3.6 Force Feedback Computation

To calculate the tool force, I extended the voxel grid based haptic force feedback approach in [164]. A voxel grid was defined based on the geometry of the surgical tool. At each simulation step, the simulator checked collision between the voxel grid of the tool with the lumbar vertebras volumetric model stored in the octree structure. Each grid voxel inside the tool contributed a unit force vector to the overall haptic force vector that tends to push this voxel towards the tool center, shown by the black arrows plotted on the red voxels in Fig. 6.8(a). In addition, I added forces produced by the contact voxels shown in green in Fig. 6.8(a). These voxels were also penetrated by the tool and generated forces towards the

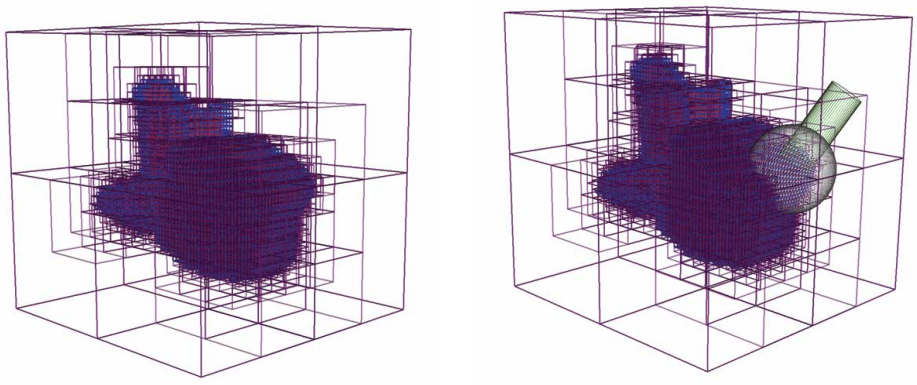

(a) (b)

Figure 6.5: The octree-based algorithm was used to represent and detect collision between the surgical tool (illustrated by the grey sphere) and the lumbar vertebra in real time.

drill center. Moreover, the area of the contact surface between the bone and the lumbar vertebra shown as the yellow curve in Fig. 6.8(a) was also taken into account. The contact area is computed as the accumulation of area from the contact voxels. In summary, in each simulation step such as Fig. 6.8(b), the overall penetration depth was calculated based on the number of inside voxels, contact voxels and the area of contact surface. The force feedback $\vec{F}_T$ provided to the haptic tool was calculated according to Eq. 6.1. $\vec{F}_{vin}$ is the force contributed by each inside voxel. $\vec{F}_{vs}$ is the force produced by each surface voxel. A_s is the contact area ratio of the surgical tool. It is calculated as the ratio of the contact area and the whole surface area of the surgical tool. The $\vec{F}_{vin}$ and $\vec{F}_{vs}$ for each voxel was calculated from Eq. 6.2, where $k = 2.5$ is the friction coefficient between the lumbar vertebra and the drill. D is the bone density of the voxel. $\vec{V}$ is the unit vector from the collided voxel to the drill center. θ is the angle between $\vec{V}$ and the drill axis.

$$\vec{F}_T = \sum_{1}^{n} \vec{F}_{vin} + \sum_{1}^{m} \vec{F}_{vs} * (1 + A_s) \tag{6.1}$$

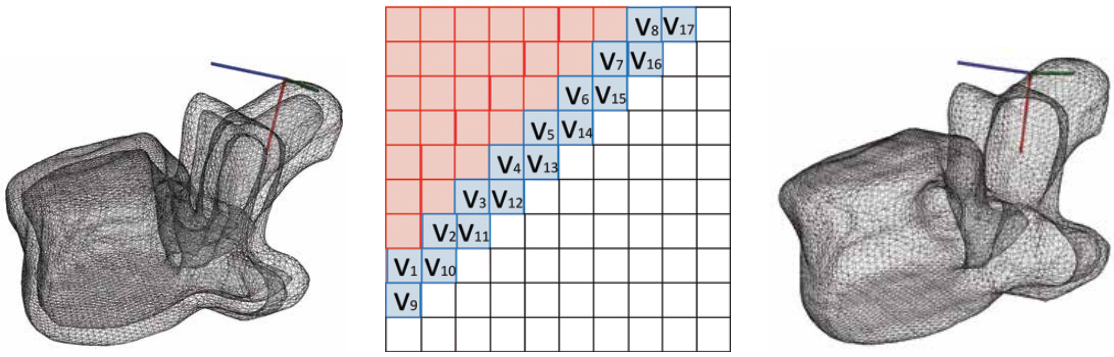

(a) (b) (c)

Figure 6.6: (a) Multiple level surface; (b) 2D adjacency graph; the proposed simulator produced smooth and realistic surface model shown in (c).

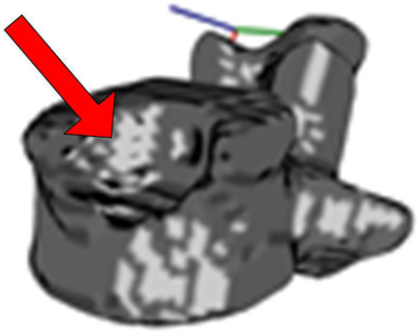

Figure 6.7: The reconstructed surface shows the dent after simulated bone drilling.

$$\vec{F}_{vin}(\vec{F}_{vs}) = k * D * \vec{V} * \cos(\theta) \tag{6.2}$$

6.4 Results

The implementation was conducted on the following platform: Windows 7 operation system with 64-bit Intel Core 2 Duo 3.0 GHz and NVIDIA GTX470 graphics card; The PHANTOM desktop 6DOF haptic device is used as the force feedback device. To run the real time visual and haptic spine surgery simulator, a multi-thread computation environment is

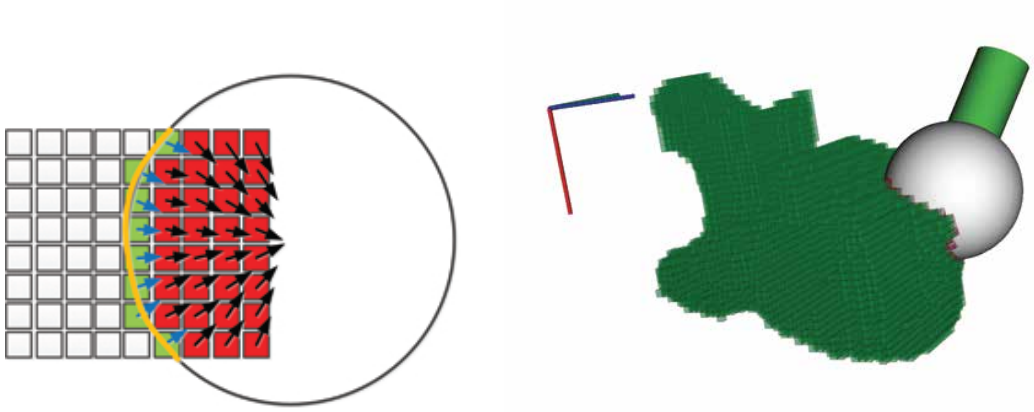

(a) (b)

Figure 6.8: The penetrated and contact voxels applied forces opposite to the force applied by the tool to the lumbar vertebra.

implemented. This gives us the capability to maintain update rates of 1000Hz for haptic rendering and 45 Hz for graphic rendering. Fig. 6.9(a) and 6.9(b) show the simulated pedicle screw insertion which interactively provided realistic visual rendering as well as force feedback through haptics to the user. I systematically analyzed the computational expense of the simulator. The number of voxels along each dimension is 256 x 256 x 256 in the finest octree level. Table 6.1 compares the computational cost of collision detection using two iterative octree traversal methods and the leaf node traversal method in simulating bone drilling surgical procedure.

It shows that the iterative depth first collision detection is the most efficient algorithm for the simulation. In each simulation step, collision detection which is the most computationally expensive operation only took 0.001 second. I experimented with various voxel resolutions, which led to nearly constant computational cost, showing the scalability of the proposed simulator. In the experiment, the voxel resolution was chosen to be 1.02 mm. The depth first traversal method is more efficient than the other two. The proposed simulation time analysis shows that interactivity can be achieved by the optimized simulator and suggests that more complex spine surgical procedures can be developed in the future.

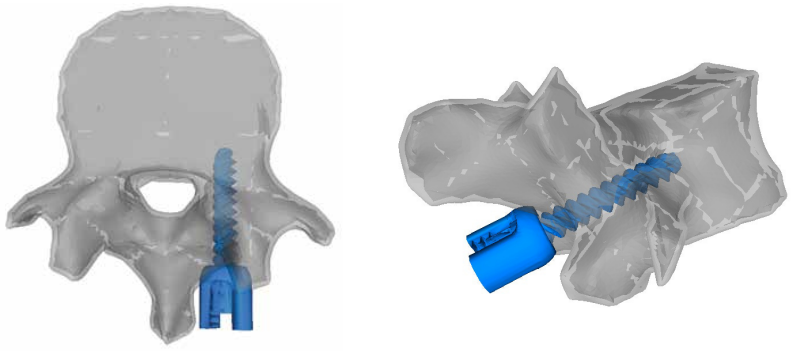

(a) (b)

Figure 6.9: The user performed a virtual pedicle screw insertion operation.

Table 6.1: Computational time (in seconds) of applying three collision detection methods.

	Computational time (s) with different voxel resolution (mm)			
Method	**0.0051**	**0.0026**	**0.0017**	**0.00102**
Depth first	0.0009	0.001	0.001	0.001
Breadth first	0.003	0.003	0.003	0.003
Leaf iterator	0.002	0.002	0.002	0.002

Fig. 6.10 shows nonlinear force feedback during surgery simulation. It computes force as function of number of voxels removed during intersection between surgical tool and bone voxels. The proposed simulator was able to simulate force increment smoothly. Integrating accurate mechanical properties of the lumbar vertebra is important to provide a realistic and meaningful training environment such that the experience gained from using the simulator can be more easily translated to the actual operations.

6.5 Conclusion

I described a spine surgical simulator which provided interactive 3D visualization and haptic force feedback. The results show that the simulator provides a real time and realistic haptic interaction system to perform virtual pedicle screw insertions. Spine surgeries are clinically

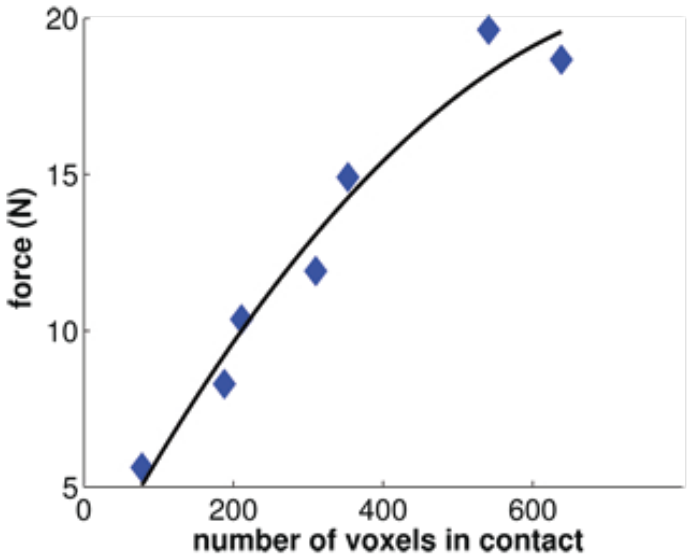

Figure 6.10: Calculated nonlinear force during pedicle screw insertion.

challenging and typically require a steep learning curve. Using a realistic 3D virtual spine surgical simulator such as the proposed system has the potential to effectively train spine surgeons and residents to enhance their surgical skills. It also has the advantage of being safe, repeatable and low-cost, making it suitable to be included in training curriculum in medical school.

I would like to improve the force feedback model. I could measure reaction force from cadaver spines during the drilling [167–169]. The validation of reaction force will be quantitatively analyzed and compared to published results [170]. The proposal force feedback computation model can generate force feedback in opposite direction towards to surgical tools handle, perpendicular to the bone surface. The torque acting on the surgical tool considered during drilling and screwing simulation. To generate more realistic environment, the drilling speed will also be considered in the computation of feedback force.

Chapter 7: Conclusion & Future Work

In this dissertation, I investigated the computational approaches to address medical image analysis problems. I presented five representative topics of analyzing extraocular muscle shape and deformation, eyeball shape, pelvic floor muscle injury, zebrafish heartbeat, and spine surgery simulation. The images used in this dissertation are acquired from different modalities (MRI, Ultrasound, Microscope Imaging and CT).

In the extraocular muscle analysis, I have developed automatic method to segment extraocular muscles and orbital structures from MR images by using super-pixel and normalized cuts method. This method could produce accurate and reproducible eye muscle segmentation and assist the evaluation of extraocular muscle enlargement. I also developed automatic methods to segment and reconstruct accurate human eyeballs from MR images. The 3D eyeball shape is quantified and evaluated through the proposed metrics. This method serves as an important diagnosis tool for people afflicted with eyeball diseases like myopia. In the extraocular muscles deformation measurement, to better understand the functions for the extraocular muscles in generating different kinds of eye movement. I designed and developed non-invasive approach to collect and study extraocular muscle kinematics during eye movement in *vivo*. In the pelvic floor muscle injury analysis, I have shown that spatially weighted multiple volume of interests 3D registration method can optimally register volumetric ultrasound image data containing significant and local anatomical differences. In the zebrafish heartbeat detection, an automatic method based on dense optical flow motion tracking and principle component analysis is introduced to detect and track the heartbeats of zebrafish larvae. The method could be applied to estimate heart rate from low resolution and low frame zebrafish video recordings. This method is computationally efficient, and easily applicable tool for studying larva cardiac function in general laboratory conditions. In spine surgery simulation, I presented a real time interactive haptic spine

surgical simulator that can be used to train residents, fellows and spine surgeons in a hospital training program. I demonstrated system performance by conducting pedicle screw insertion.

There are several ways to extend the proposed approaches in this dissertation. For extraocular muscle deformation analysis, my current work analyzes local deformation of the medial rectus muscle during eye movement. It would be valuable to explore dynamic features of six extraocular muscles during eye movement at different patterns and speed, since understanding the mechanisms of eye movement is difficult without a realistic dynamic analysis of the extraocular muscles. New feature-based motion tracking algorithms could be designed for tracking the local deformations on each extraocular muscle. The extraocular muscle strain could be analyzed during different types (smooth pursue and saccadic) eye movements. These results will help the clinician to examine whether there exists differential movement between the two layers in each rectus muscle. Answer to such question can advance our understanding on the role of the ocular mechanics in the coordination of eye movement.

For the pelvic floor muscle injury analyze, although the proposed two-step multiple VOIs 3D registration could help to identify the needle tip position in the muscle intact 3D ultrasound volume, how to accurately segment the soft tissues such as levator ani muscle from 3D ultrasound volume is still an unsolved problem due to the fact that ultrasound imaging has lower SNR. Most clinical applications are achieved by applying CNNs on MRI and CT image segmentation. Such segmentation is obtained by only considering similarity of local intensity. Therefore, it fails in other modalities such as ultrasound, where image SNR is lower and intrinsic noise is associated with image. Prior knowledge about 3D shape of the tissue can provide additional features for guidance, and can improve the accuracy of ultrasound image segmentation.

Bibliography

Bibliography

[1] A. Sotiras, C. Davatzikos, and N. Paragios, "Deformable medical image registration: A survey," *IEEE Trans. Med. Imaging.*, vol. 32, no. 7, pp. 1153–1190, Jul. 2013.

[2] W. R. Bijlsma and M. P. Mourits, "Radiologic measurement of extraocular muscle volumes in patients with graves' orbitopathy: a review and guideline," vol. 25, no. 2, pp. 83–91.

[3] G. J. Ben Simon, H. M. Syed, R. Douglas, J. D. McCann, and R. A. Goldberg, "Extraocular muscle enlargement with tendon involvement in thyroid-associated orbitopathy." vol. 137, no. 6, pp. 1145–1147.

[4] A. J. Dal Canto, S. Crowe, J. D. Perry, and E. I. Traboulsi, "Intraoperative relaxed muscle positioning technique for strabismus repair in thyroid eye disease," vol. 113, no. 12, pp. 2324–2330.

[5] A. Gupta, P. B. Sadeghi, and E. K. Akpek, "Occult thyroid eye disease in patients presenting with dry eye symptoms," vol. 147, no. 5, pp. 919–923.

[6] X. Qi, L. Yifan, W. Brendan, D. Joseph, L., and W. Qi, "Automatic segmentation of extraocular muscles using superpixel and normalized cut," in *In Proceeding of the 11th International Symposium on Visual Computing*, 2015.

[7] X. Qi, S. Siddhartha, and W. Qi, "Measurement of extraocular muscle deformation using ultrasound imaging," in *American Society of Biomechanics*, 2016.

[8] R. Kono, V. Poukens, and J. L. Demer, "Quantitative analysis of the structure of the human extraocular muscle pulley system," vol. 43, no. 9, pp. 2923–2932.

[9] Z. Chaudhuri and J. L. Demer, "Sagging eye syndrome: connective tissue involution as a cause of horizontal and vertical strabismus in older patients," vol. 131, no. 5, pp. 619–625, 2013.

[10] M. J. Firbank and A. Coulthard, "Evaluation of a technique for estimation of extraocular muscle volume using 2d MRI." vol. 73, no. 876, pp. 1282–1289.

[11] M. J. Firbank, R. M. Harrison, E. D. Williams, and A. Coulthard, "Measuring extraocular muscle volume using dynamic contours," vol. 19, no. 2, pp. 257–265.

[12] A. D. A. Souza, E. E. S. Ruiz, and A. A. V. Cruz, "Extraocular muscle quantification using mathematical morphology: A semi-automatic method for analyzing muscle enlargement in orbital diseases," vol. 31, no. 1, pp. 39–45.

[13] Z. Szucs-Farkas, J. Toth, E. Balazs, L. Galuska, K. D. Burman, Z. Karanyi, A. Leovey, and E. V. Nagy, "Using morphologic parameters of extraocular muscles for diagnosis and follow-up of graves' ophthalmopathy: diameters, areas, or volumes?" vol. 179, no. 4, pp. 1005–1010.

[14] B. Lv, T. N. Wu, K. Lu, and Y. Xie, "Automatic segmentation of extraocular muscle using level sets methods with shape prior," in *IFMBE*. Springer Berlin Heidelberg, pp. 904–907.

[15] R. Achanta, A. Shaji, K. Smith, A. Lucchi, P. Fua, and S. Ssstrunk, "SLIC superpixels compared to state-of-the-art superpixel methods," vol. 34, no. 11, pp. 2274–2282.

[16] X. Ren and J. Malik, "Learning a classification model for segmentation," in *ICCV*, pp. 10–17.

[17] B. Fulkerson, A. Vedaldi, and S. Soatto, "Class segmentation and object localization with superpixel neighborhoods," in *ICCV*, pp. 670–677.

[18] A. Levinshtein, C. Sminchisescu, and S. Dickinson, "Optimal contour closure by superpixel grouping," in *Computer Vision ECCV 2010*. Springer Berlin Heidelberg, pp. 480–493.

[19] T. Chan and L. Vese, "Active contours without edges," vol. 10, no. 2, pp. 266–277.

[20] M. Kass, A. Witkin, and D. Terzopoulos, "Snakes: active contour models," vol. 1, no. 4, pp. 321–331.

[21] A. D. A. Souza, E. E. S. Ruiz, and A. A. V. Cruz, "Extraocular muscle quantification using mathematical morphology: A semi-automatic method for analyzing muscle enlargement in orbital diseases," vol. 31, no. 1, pp. 39–45, 2007-01.

[22] A. Souza and E. Ruiz, "Fast and accurate detection of extraocular muscle borders using mathematical morphology," in *IEMBS*, pp. 1779–1782.

[23] Q. Wei, S. Sueda, J. Miller, J. Demer, and D. Pai, "Template-based reconstruction of human extraocular muscles from magnetic resonance images," in *IEEE International Symposium on Biomedical Imaging: From Nano to Macro, 2009. ISBI '09*, pp. 105–108.

[24] P. F. Felzenszwalb and D. P. Huttenlocher, "Efficient graph-based image segmentation," vol. 59, no. 2, pp. 167–181.

[25] A. Vedaldi and S. Soatto, "Quick shift and kernel methods for mode seeking," in *Computer Vision ECCV 2008*. Springer Berlin Heidelberg, pp. 705–718.

[26] C. Conrad, M. Mertz, and R. Mester, "Contour-relaxed superpixels," in *EMMCVPR*. Springer Berlin Heidelberg, pp. 280–293.

[27] S. Gould, J. Rodgers, D. Cohen, G. Elidan, and D. Koller, "Multi-class segmentation with relative location prior," vol. 80, no. 3, pp. 300–316.

[28] A. Tremeau and P. Colantoni, "Regions adjacency graph applied to color image segmentation," vol. 9, no. 4, pp. 735–744.

[29] J. Shi and J. Malik, "Normalized cuts and image segmentation," vol. 22, no. 8, pp. 888–905.

[30] M. Sharifi, M. Fathy, and M. Tayefeh Mahmoudi, "A classified and comparative study of edge detection algorithms," in *ITCC*, pp. 117–120.

[31] R. L. Thorndike, "Who belongs in the family?" vol. 18, no. 4, pp. 267–276.

[32] R. Tibshirani, G. Walther, and T. Hastie, "Estimating the number of clusters in a data set via the gap statistic," vol. 63, no. 2, pp. 411–423.

[33] M. Meila, "Comparing clusterings: an axiomatic view," ser. ICML, pp. 577–584.

[34] W. M. Rand, "Objective criteria for the evaluation of clustering methods," vol. 66, no. 336, pp. 846–850.

[35] T. Malisiewicz and A. A. Efros, "Improving spatial support for objects via multiple segmentations," in *BMVC*, pp. 1–10.

[36] P. Arbelaez, M. Maire, C. Fowlkes, and J. Malik, "Contour detection and hierarchical image segmentation," vol. 33, no. 5, pp. 898–916.

[37] M. Piccirelli, R. Luechinger, A. K. Rutz, P. Boesiger, and O. Bergamin, "Extraocular muscle deformation assessed by motion-encoded MRI during eye movement in healthy subjects," *Journal of Vision*, vol. 7, no. 14, p. 5, Nov. 2007.

[38] M. Piccirelli, R. Luechinger, V. Sturm, P. Boesiger, K. Landau, and O. Bergamin, "Local deformation of extraocular muscles during eye movement," *Investigative Ophthalmology & Visual Science*, vol. 50, no. 11, pp. 5189–5196, Nov. 2009.

[39] "Tagged MRI of ocular tissues at 3t and 7t." [Online]. Available: http://www.healthcare.siemens.com

[40] J. L. Demer, S. Y. Oh, and V. Poukens, "Evidence for active control of rectus extraocular muscle pulleys," *Investigative Ophthalmology & Visual Science*, vol. 41, no. 6, pp. 1280–1290, May 2000.

[41] D. G. Lowe, "Distinctive image features from scale-invariant keypoints," *Int. J. Comput. Vision*, vol. 60, no. 2, pp. 91–110, Nov. 2004.

[42] X. Zhong, F. H. Epstein, B. S. Spottiswoode, P. A. Helm, and S. S. Blemker, "Imaging two-dimensional displacements and strains in skeletal muscle during joint motion by cine DENSE MR," *Journal of Biomechanics*, vol. 41, no. 3, pp. 532–540, 2008.

[43] X. Qi and W. Qi, "Human eyeball model reconstruction and quantitative analysis," in *36th Annual International Conference of the IEEE Engineering in Medicine and Biology Society*, 2014.

[44] S.-W. Cheung and P. Cho, "Validity of axial length measurements for monitoring myopic progression in orthokeratology," vol. 54, no. 3, pp. 1613–1615.

[45] L. Llorente, S. Barbero, D. Cano, C. Dorronsoro, and S. Marcos, "Myopic versus hyperopic eyes: axial length, corneal shape and optical aberrations," vol. 4, no. 4, p. 5.

[46] D. O. Mutti, J. R. Hayes, G. L. Mitchell, L. A. Jones, M. L. Moeschberger, S. A. Cotter, R. N. Kleinstein, R. E. Manny, J. D. Twelker, K. Zadnik, and CLEERE Study Group, "Refractive error, axial length, and relative peripheral refractive error before and after the onset of myopia," vol. 48, no. 6, pp. 2510–2519.

[47] D. A. Atchison, C. E. Jones, K. L. Schmid, N. Pritchard, J. M. Pope, W. E. Strugnell, and R. A. Riley, "Eye shape in emmetropia and myopia," vol. 45, no. 10, pp. 3380–3386.

[48] K. Ishii, H. Iwata, and T. Oshika, "Quantitative evaluation of changes in eyeball shape in emmetropization and myopic changes based on elliptic fourier descriptors," vol. 52, no. 12, pp. 8585–8591.

[49] D. A. Atchison, N. Pritchard, K. L. Schmid, D. H. Scott, C. E. Jones, and J. M. Pope, "Shape of the retinal surface in emmetropia and myopia," vol. 46, no. 8, pp. 2698–2707.

[50] K. D. Singh, N. S. Logan, and B. Gilmartin, "Three-dimensional modeling of the human eye based on magnetic resonance imaging," vol. 47, no. 6, pp. 2272–2279.

[51] M. Moriyama, K. Ohno-Matsui, K. Hayashi, N. Shimada, T. Yoshida, T. Tokoro, and I. Morita, "Topographic analyses of shape of eyes with pathologic myopia by high-resolution three-dimensional magnetic resonance imaging," vol. 118, no. 8, pp. 1626–1637.

[52] Q. Wei, S. Sueda, J. Miller, J. Demer, and D. Pai, "Template-based reconstruction of human extraocular muscles from magnetic resonance images," in *ISBI*, pp. 105–108.

[53] J. Canny, "A computational approach to edge detection," vol. 8, no. 6, pp. 679–698.

[54] Z. Zhang, *Iterative point matching for registration of free-form curves.*

[55] M. Eck, "Automatic reconstruction of b-spline surfaces of arbitrary topological type," in *SIGGRAPH'96*, pp. 325–334.

[56] Q. Wei and D. K. Pai, "Physically consistent registration of extraocular muscle models from MRI," in *2008 30th Annual International Conference of the IEEE Engineering in Medicine and Biology Society*, pp. 2237–2241.

[57] I. R. Porteous, *Geometric differentiation: for the intelligence of curves and surfaces.* Cambridge University Press.

[58] W. Kuhnel and B. Hunt, *Differential geometry: curves - surfaces - manifolds.* American Mathematical Society.

[59] T. Cover and P. Hart, "Nearest neighbor pattern classification," vol. 13, no. 1, pp. 21–27.

[60] M. A. Fischler and R. C. Bolles, "Random sample consensus: a paradigm for model fitting with applications to image analysis and automated cartography," vol. 24, no. 6, pp. 381–395.

[61] W. Qi, X. Qi, S. Connor, C. Parag, S. Siddhartha, R. Ghazaleh, and A. S. Seyed, "3d ultrasound imaging of pelvic floor muscle injury," in *Ultrasonic Imaging Tissue Characterization*, 2017.

[62] W. Qi, X. Qi, C. Parag, S. Siddhartha, and A. S. Seyed, "Quantitative analysis of 3d ultrasound images for assessing pelvic floor muscle injury," in *Ultrasonic Imaging and Tissue Characterization*, 2018.

[63] F. P. Oliveira and J. M. R. Tavares, "Medical image registration: a review," *Comput. Method. Biomec.*, vol. 17, no. 2, pp. 73–93, 2014.

[64] J. G. Rosenman and et al., "Image registration: an essential part of radiation therapy treatment planning," *Int. J. Radiat. Oncol. Biol. Phys.*, vol. 40, no. 1, pp. 197 – 205, 1998.

[65] A. Bardera, M. Feixas, I. Boada, J. Rigau, and M. Sbert, "Registration-based segmentation using the information bottleneck method," in *Pattern Recognition and Image Analysis*, ser. Lecture Notes in Computer Science. Springer, Berlin, Heidelberg, Jun. 2007, pp. 130–137.

[66] F. Sauer, "Image registration: enabling technology for image guided surgery and therapy," in *In Proc. IEEE 27th Eng. Med. Biol. Soc.*, Shanghai, China, Jan. 2005, pp. 7242–7245.

[67] A. Gooya and et al., "An EM algorithm for brain tumor image registration: A tumor growth modeling based approach," in *In Proc. IEEE Comput. Soc. Conf. Comput. Vis. Pattern. Recognit.*, San Francisco, CA, Jun. 2010, pp. 39–46.

[68] J. B. A. Maintz and M. A. Viergever, *An overview of medical image registration methods*. Oxford Univeristy Press, 1998.

[69] B. Glocker and et al., "Deformable medical image registration: setting the state of the art with discrete methods," *Annu. Rev. Biomed. Eng.*, vol. 13, no. 1, pp. 219–244, Jul. 2011.

[70] E. Ferrante and N. Paragios, "Slice-to-volume medical image registration: A survey," *Med. Image. Anal.*, vol. 39, pp. 101–123, Jul. 2017.

[71] S. Klein, M. Staring, K. Murphy, M. A. Viergever, and J. P. W. Pluim, "elastix: A toolbox for intensity-based medical image registration," *IEEE Trans. Med. Imaging.*, vol. 29, no. 1, pp. 196–205, Jan. 2010.

[72] R. Shams, P. Sadeghi, R. A. Kennedy, and R. I. Hartley, "A survey of medical image registration on multicore and the GPU," *IEEE Signal Process. Mag.*, vol. 27, no. 2, pp. 50–60, Mar. 2010.

[73] A. M. Loening and S. S. Gambhir, "AMIDE: A free software tool for multimodality medical image analysis," *Mol. Imaging*, vol. 2, no. 3, pp. 131–137, Jul. 2003.

[74] C. Che and et al., "Ultrasound registration: A review," *Methods*, vol. 115, pp. 128–143, Feb. 2017.

[75] M. L. Oelze and J. Mamou, "Review of quantitative ultrasound: envelope statistics and backscatter coefficient imaging and contributions to diagnostic ultrasound," *IEEE Transactions on Ultrasonics, Ferroelectrics, and Frequency Control*, vol. 63, no. 2, pp. 336–351, Feb. 2016.

[76] M. L. Oelze, "Quantitative ultrasound techniques and improvements to diagnostic ultrasonic imaging," in *2012 IEEE International Ultrasonics Symposium*, Oct. 2012, pp. 232–239.

[77] G. Low and E. Leen, *Clinical ultrasound (Third Edition)*. Edinburgh: Churchill Livingstone, 2011, ch. 10.

[78] L. F. Smith, R. Henry-Tillman, S. Harms, T. Hronas, A. T. Mancino, K. C. Westbrook, S. Korourian, M. P. Jones, and V. S. Klimberg, "Hematoma-directed ultrasound-guided breast biopsy," *Ann. Surg.*, vol. 233, no. 5, pp. 669–675, May 2001.

[79] B. Rister and et al., "Volumetric image registration from invariant keypoints," *IEEE Trans. Image Process.*, vol. 26, no. 10, pp. 4900–4910, Oct. 2017.

[80] B. Zitov and J. Flusser, "Image registration methods: a survey," *Image Vis. Comput.*, vol. 21, no. 11, pp. 977–1000, Oct. 2003.

[81] W. R. Crum and et al., "Non-rigid image registration: theory and practice," *Br. J. Radiol.*, vol. 77, no. 2, pp. S140–S153, Dec. 2004.

[82] M. A. Viergever, J. B. A. Maintz, S. Klein, K. Murphy, M. Staring, and J. P. W. Pluim, "A survey of medical image registration," *Med. Image Anal.*, vol. 33, pp. 140–144, Oct. 2016.

[83] J. Banerjee, C. Klink, E. D. Peters, W. J. Niessen, A. Moelker, and T. van Walsum, "Fast and robust 3d ultrasound registration Block and game theoretic matching," *Medical Image Analysis*, vol. 20, no. 1, pp. 173–183, Feb. 2015.

[84] R. J. Schneider, D. P. Perrin, N. V. Vasilyev, G. R. Marx, P. J. del Nido, and R. D. Howe, "Real-time image-based rigid registration of three-dimensional ultrasound," *Med. Image Anal.*, vol. 16, no. 2, pp. 402–414, Feb. 2012.

[85] D. Zikic and et al., "Fast deformable registration of 3d-ultrasound data using a variational approach," in *In Proc. Med. Image Comput. Comput. Assist. Interv.*, ser. Lecture Notes in Computer Science. Springer, Berlin, Heidelberg, Oct. 2006, pp. 915–923.

[86] J. O. DeLancey, "The hidden epidemic of pelvic floor dysfunction: Achievable goals for improved prevention and treatment," *Am. J. Obstet. Gynecol.*, vol. 192, no. 5, pp. 1488 – 1495, 2005.

[87] L. L. Subak, L. E. Waetjen, S. van den Eeden, D. H. Thom, E. Vittinghoff, and J. S. Brown, "Cost of pelvic organ prolapse surgery in the united states," *Obstet. Gynecol.*, vol. 98, no. 4, pp. 646–651, Oct. 2001.

[88] J. O. L. DeLancey, D. M. Morgan, D. E. Fenner, R. Kearney, K. Guire, J. M. Miller, H. Hussain, W. Umek, Y. Hsu, and J. A. Ashton-Miller, "Comparison of levator ani muscle defects and function in women with and without pelvic organ prolapse," *Obstet. Gynecol.*, vol. 109, no. 2 Pt 1, pp. 295–302, Feb. 2007.

[89] A. Shobeiri, Ed., *Practical pelvic floor ultrasonography: a multicompartmental approach to 2D/3D/4D ultrasonography of the pelvic floor*, 2nd ed. Springer International Publishing, 2017.

[90] G. Rostaminia, D. E. White, L. H. Quiroz, and S. A. Shobeiri, "Levator plate descent correlates with levator ani muscle deficiency," *Neurourol. Urodyn.*, vol. 34, no. 1, pp. 55–59, Jan. 2015.

[91] J. A. AshtonMiller and J. O. L. DeLANCEY, "Functional anatomy of the female pelvic floor," *Ann. N. Y. Acad. Sci.*, vol. 1101, no. 1, pp. 266–296, Apr. 2007.

[92] J. O. L. DeLancey, R. Kearney, Q. Chou, S. Speights, and S. Binno, "The appearance of levator ani muscle abnormalities in magnetic resonance images after vaginal delivery," *Obstetrics and gynecology*, vol. 101, no. 1, pp. 46–53, Jan. 2003.

[93] G. A. Santoro, A. P. Wieczorek, H. P. Dietz, A. Mellgren, A. H. Sultan, S. A. Shobeiri, A. Stankiewicz, and C. Bartram, "State of the art: an integrated approach to pelvic floor ultrasonography," *Ultrasound in Obstetrics & Gynecology*, vol. 37, no. 4, pp. 381–396, Apr. 2011.

[94] S. A. Shobeiri and et al., "Use of ultrasound imaging in pelvic organ prolapse: an overview," *Curr. Obstet. Gynecol. Rep.*, vol. 4, no. 2, pp. 109–114, Jun. 2015.

[95] Q. Wei, S. Sikdar, P. Chitnis, G. Rostaminia, and S. Abbas Shobeiri, *Patient-specific studies of pelvic floor biomechanics using imaging.* Cham: Springer International Publishing, 2017, pp. 337–344.

[96] P. Javadian, D. O'Leary, G. Rostaminia, J. North, J. Wagner, L. H. Quiroz, and S. A. Shobeiri, "How does 3d endovaginal ultrasound compare to magnetic resonance imaging in the evaluation of levator ani anatomy?" *Neurourol. Urodyn.*, vol. 36, no. 2, pp. 409–413, 2017.

[97] D. Mattes, D. R. Haynor, H. Vesselle, T. K. Lewellyn, and W. Eubank, "Nonrigid multimodality image registration," vol. 4322, 2001, pp. 1609–1620.

[98] R. W. K. So and et al., "Non-rigid image registration of brain magnetic resonance images using graph-cuts," *Pattern Recognit.*, vol. 44, no. 10, pp. 2450–2467, Oct. 2011.

[99] J. Woo, B.-W. Hong, C.-H. Hu, K. K. Shung, C.-C. J. Kuo, and P. J. Slomka, "Non-rigid ultrasound image registration based on intensity and local phase information," *J. Signal Process. Syst.*, vol. 54, no. 1-3, pp. 33–43, Jan. 2009.

[100] S. G. Schalk and et al., "3d surface-based registration of ultrasound and histology in prostate cancer imaging," *Comput. Med. Imaging Graph.*, vol. 47, pp. 29–39, Jan. 2016.

[101] R. Shekhar and et al., "Registration of real-time 3-d ultrasound images of the heart for novel 3-D stress echocardiography," *IEEE Trans. Med. Imaging*, vol. 23, no. 9, pp. 1141–1149, Sep. 2004.

[102] R. Francois and et al., "Robust statistical registration of 3d ultrasound images using texture information," in *In Proc. Int. Conf. Image Process.*, vol. 1, Barcelona, Spain, Sep. 2003, pp. I581–I584.

[103] I. Hacihaliloghlu, A. Rasoulian, R. N. Rohling, and P. Abolmaesumi, "Statistical shape model to 3d ultrasound registration for spine interventions using enhanced local phase features," *Med. Image Comput. Comput. Assist. Interv.*, vol. 16, no. 2, pp. 361–368, 2013.

[104] W. Zhang, J. A. Noble, and J. M. Brady, "Adaptive non-rigid registration of real time 3d ultrasound to cardiovascular MR images," in *Inf. Process. Med. Imaging*, ser. Lecture Notes in Computer Science. Springer, Berlin, Heidelberg, Jul. 2007, pp. 50–61.

[105] C. R. Meyer, J. L. Boes, B. Kim, P. H. Bland, G. L. Lecarpentier, J. B. Fowlkes, M. A. Roubidoux, and P. L. Carson, "Semiautomatic registration of volumetric ultrasound scans," *Ultrasound Med. Biol.*, vol. 25, no. 3, pp. 339–347, Mar. 1999.

[106] J. A. Panza, "Real-time three-dimensional echocardiography: an overview," *Int. J. Cardiovasc. Imaging*, vol. 17, no. 3, pp. 227–235, Jun. 2001.

[107] R. Shekhar and et al., "Mutual information-based rigid and nonrigid registration of ultrasound volumes," *IEEE Trans. Med. Imaging*, vol. 21, no. 1, pp. 9–22, Jan. 2002.

[108] X. Papademetris and et al., "Integrated intensity and point-feature nonrigid registration," *Med. Image. Comput. Comput. Assist. Interv.*, vol. 3216, no. 2004, pp. 763–770, Sep. 2001.

[109] M. Abdel-Basset and et al., "Feature and intensity based medical image registration using particle swarm optimization," *J. Med. Syst.*, vol. 41, no. 12, p. 197, Nov. 2017.

[110] H. Song and P. Qiu, "A parametric intensity-based 3d image registration method for magnetic resonance imaging," *Signal Image Video P.*, vol. 11, no. 3, pp. 455–462, Mar. 2017.

[111] G. Rostaminia and et al., "Characteristics associated with pelvic organ prolapse in women with significant levator ani muscle deficiency," *Int. Urogynecol. J.*, vol. 27, no. 2, pp. 261–267, Feb. 2016.

[112] P. Busacchi, R. D. Giorgio, D. Santini, E. Bellavia, T. Perri, C. Oliverio, R. Paradisi, R. Corinaldesi, and C. Flamigni, "A histological and immunohistochemical study of neuropeptide containing somatic nerves in the levator animuscle of women with genitourinary prolapse," *Acta Obstet. Gynecol. Scand.*, vol. 78, no. 1, pp. 2–5, Jan. 1999.

[113] J. Cabrera and et al., "Unbiased estimation of ellipses by bootstrapping," *IEEE Trans. Pattern Anal. Mach. Intell.*, vol. 18, no. 7, pp. 752–756, Jul. 1996.

[114] J. J. Hans and et al., *The ITK Software Guide: Introduction and Development Guidelines*, 4th ed. Kitware Inc., 2015.

[115] Z. Wang, G. Slabaugh, G. Unal, and T. Fang, "Registration of ultrasound images using an information-theoretic feature detector," in *In Proc. 4th IEEE Int. Symp. Biomed. Imaging*, Arlington, VA, Apr. 2007, pp. 736–739.

[116] J. Wang, S. Horvath, G. Stetten, M. Siegel, and J. Galeotti, "Real-time registration of video with ultrasound using stereo disparity," in *In SPIE Med. imaging*. San Diego, CA: International Society for Optics and Photonics, Feb. 2012.

[117] G. Narayanasamy, G. L. LeCarpentier, M. Roubidoux, J. B. Fowlkes, A. F. Schott, and P. L. Carson, "Spatial registration of temporally separated whole breast 3d ultrasound images," *Med. Phys.*, vol. 36, no. 9, pp. 4288–4300, Sep. 2009.

[118] T. D. Silva, A. Uneri, X. Zhang, M. Ketcha, R. Han, M. Jacobson, N. Sheth, S. Vogt, G. Kleinszig, A. Belzberg, D. M. Sciubba, and J. H. Siewerdsen, "Real-time image-based 3d-2d registration for ultrasound-guided spinal interventions," in *In SPIE: Med. Imaging*, vol. 10576. Houston, Texas: International Society for Optics and Photonics, Mar. 2018, p. 105760E.

[119] Y. N. Dwith Chenna, P. Ghassemi, T. J. Pfefer, J. Casamento, and Q. Wang, "Free-form deformation approach for registration of visible and infrared facial images in fever screening," *Sensors (Basel)*, vol. 18, no. 1, p. E25, Jan. 2018.

[120] C. A. Schneider and et al., "NIH image to ImageJ: 25 years of image analysis," *Nat. Methods*, vol. 9, no. 7, pp. 671–675, Jul. 2012.

[121] M. Berger and et al., "A benchmark for surface reconstruction," *ACM Trans. Graph.*, vol. 32, no. 2, pp. 20:1–20:17, Apr. 2013.

[122] Y. Ou and et al., "DRAMMS: deformable registration via attribute matching and mutual-saliency weighting," *Med. Image. Anal.*, vol. 15, no. 4, pp. 622–639, Aug. 2011.

[123] D. Shen, "Image registration by local histogram matching," *Pattern Recognit.*, vol. 40, no. 4, pp. 1161–1172, Apr. 2007.

[124] X. Qi, H. Victor, W. Qi, P. Thales, Guimaraes, M.-M. Claudia, and P. Nathalia, "Zebrafish larvae heartbeat detection from body deformation in low resolution and low frequency video," *Medical & Biological Engineering & Computing*, 2018.

[125] T. Afrikanova, A.-S. K. Serruys, O. E. M. Buenafe, R. Clinckers, I. Smolders, P. A. M. de Witte, A. D. Crawford, and C. V. Esguerra, "Validation of the zebrafish pentylenetetrazol seizure model: locomotor versus electrographic responses to antiepileptic drugs," *PLoS ONE*, vol. 8, no. 1, Jan. 2013.

[126] K. Howe, M. D. Clark, C. F. Torroja, J. Torrance, C. Berthelot, M. Muffato, J. E. Collins, and e. a. Humphray, "The zebrafish reference genome sequence and its relationship to the human genome," *Nature*, vol. 496, no. 7446, p. nature12111, Apr. 2013.

[127] G. J. Lieschke and P. D. Currie, "Animal models of human disease: zebrafish swim into view," *Nature Reviews Genetics*, vol. 8, no. 5, p. nrg2091, May 2007.

[128] S. C. Baraban, M. R. Taylor, P. A. Castro, and H. Baier, "Pentylenetetrazole induced changes in zebrafish behavior, neural activity and c-fos expression," *Neuroscience*, vol. 131, no. 3, pp. 759–768, Jan. 2005.

[129] E. De Luca, G. M. Zaccaria, M. Hadhoud, G. Rizzo, R. Ponzini, U. Morbiducci, and M. M. Santoro, "ZebraBeat: a flexible platform for the analysis of the cardiac rate in zebrafish embryos," *Scientific Reports*, vol. 4, May 2014.

[130] R. N. Wilkinson, C. Jopling, and F. J. M. van Eeden, "Zebrafish as a model of cardiac disease," in *Progress in Molecular Biology and Translational Science*, ser. Genetics of Cardiovascular Disease, T. J. A. Chico, Ed. Academic Press, Jan. 2014, vol. 124, pp. 65–91.

[131] C. Singleman and N. G. Holtzman, "Analysis of post-embryonic heart development and maturation in the zebrafish, danio rerio," *Developmental dynamics : an official publication of the American Association of Anatomists*, vol. 241, no. 12, pp. 1993–2004, Dec. 2012.

[132] J. Bakkers, "Zebrafish as a model to study cardiac development and human cardiac disease," *Cardiovascular Research*, vol. 91, no. 2, pp. 279–288, Jul. 2011.

[133] D. J. Milan, I. L. Jones, P. T. Ellinor, and C. A. MacRae, "In vivo recording of adult zebrafish electrocardiogram and assessment of drug-induced QT prolongation," *American Journal of Physiology - Heart and Circulatory Physiology*, vol. 291, no. 1, pp. H269–H273, Jul. 2006.

[134] P. K. Chan, C. C. Lin, and S. H. Cheng, "Noninvasive technique for measurement of heartbeat regularity in zebrafish (Danio rerio) embryos," *BMC Biotechnology*, vol. 9, p. 11, Feb. 2009.

[135] C. Pylatiuk, D. Sanchez, R. Mikut, R. Alshut, M. Reischl, S. Hirth, W. Rottbauer, and S. Just, "Automatic zebrafish heartbeat detection and analysis for zebrafish embryos," *Zebrafish*, vol. 11, no. 4, pp. 379–383, Aug. 2014.

[136] G. Balakrishnan, F. Durand, and J. Guttag, "Detecting pulse from head motions in video," in *2013 IEEE Conference on Computer Vision and Pattern Recognition*, Jun. 2013, pp. 3430–3437.

[137] M. Westerfield, *The zebrafish book: a guide for the laboratory use of zebrafish (Danio rerio)*, 2007.

[138] C. B. Kimmel, W. W. Ballard, S. R. Kimmel, B. Ullmann, and T. F. Schilling, "Stages of embryonic development of the zebrafish," *Developmental Dynamics*, vol. 203, no. 3, pp. 253–310, Jul. 1995.

[139] G. Farnebck, "Two-frame motion estimation based on polynomial expansion," in *Image Analysis*, ser. Lecture Notes in Computer Science. Springer, Berlin, Heidelberg, Jun. 2003, pp. 363–370.

[140] S.-J. Cho, D. Byun, T.-S. Nam, S.-Y. Choi, B.-G. Lee, M.-K. Kim, and S. Kim, "Zebrafish as an animal model in epilepsy studies with multichannel EEG recordings," *Scientific Reports*, vol. 7, no. 1, p. 3099, Jun. 2017.

[141] G. N. Robertson, C. a. S. McGee, T. C. Dumbarton, R. P. Croll, and F. M. Smith, "Development of the swimbladder and its innervation in the zebrafish, Danio rerio," *Journal of Morphology*, vol. 268, no. 11, pp. 967–985, Nov. 2007.

[142] S. J. Lee, S. H. Park, J. F. Chung, W. Choi, and H. K. Huh, "Homocysteine-induced peripheral microcirculation dysfunction in zebrafish and its attenuation by L-arginine," *Oncotarget*, vol. 8, no. 35, pp. 58 264–58 271, Apr. 2017.

[143] J. Pu, B. Zheng, J. K. Leader, and D. Gur, "An ellipse-fitting based method for efficient registration of breast masses on two mammographic views," *Medical physics*, vol. 35, no. 2, pp. 487–494, Feb. 2008.

[144] T. Sotysiski, A. Rodatus, N. Golnik, and T. Pako, "Comparison of multiscale entropy of healthy and cancer tissue imaged by optical polarimeter," in *World Congress on Medical Physics and Biomedical Engineering 2006*, ser. IFMBE Proceedings. Springer, Berlin, Heidelberg, 2007, pp. 1291–1294.

[145] J.-y. Bouguet, "Pyramidal implementation of the Lucas Kanade feature tracker," *Intel Corporation, Microprocessor Research Labs*, 2000.

[146] T. Sotysiski, "Bayesian constrained spectral method for segmentation of noisy medical images theory and applications," in *Advanced Computational Intelligence Paradigms in Healthcare - 3*, ser. Studies in Computational Intelligence. Springer, Berlin, Heidelberg, 2008, pp. 181–206.

[147] T. Sotysiski and Kauynski, "Novel quantitative method for spleens morphometry in splenomegally," in *Artificial Intelligence and Soft Computing ICAISC 2008*, ser. Lecture Notes in Computer Science. Springer, Berlin, Heidelberg, Jun. 2008, pp. 981–991.

[148] T. Sotysiski, K. Kauynski, and T. Pako, "Cardiac ventricle contour reconstruction in ultrasonographic images using bayesian constrained spectral method," in *Artificial Intelligence and Soft Computing ICAISC 2006*, ser. Lecture Notes in Computer Science. Springer, Berlin, Heidelberg, Jun. 2006, pp. 988–997.

[149] X. Qi, X. C. Jim, L. Jihui, M. Ali, T. Mark, and W. Qi, "A real time haptic simulator of spine surgeries," in *In Proceeding of the 21th ACM Symposium on Virtual Reality Software and Technology*, 2015.

[150] X. Qi, L. Jihui, M. Ali, X. C. Jim, M. T. Mark, and W. Qi, "Physically-based haptics simulator for spine surgery simulation," in *7th World Congress of Biomechanics*, 2014.

[151] J. A. Gruskay, M. L. Webb, and J. N. Grauer, "Methods of evaluating lumbar and cervical fusion," *The Spine Journal*, vol. 14, no. 3, pp. 531–539, Mar. 2014.

[152] B. Ravi, A. Zahrai, and R. Rampersaud, "Clinical accuracy of computer-assisted two-dimensional fluoroscopy for the percutaneous placement of lumbosacral pedicle screws," *Spine*, vol. 36, no. 1, pp. 84–91, 2010.

[153] R. Chitale, G. M. Ghobrial, D. Lobel, and J. Harrop, "Simulated lumbar minimally invasive surgery educational model with didactic and technical components," *Neurosurgery*, vol. 73, pp. S107–S110, Oct. 2013.

[154] M. Nagendran, K. S. Gurusamy, R. Aggarwal, M. Loizidou, and B. R. Davidson, "Virtual reality training for surgical trainees in laparoscopic surgery," in *Cochrane Database of Systematic Reviews*. John Wiley & Sons, Ltd, Aug. 2013.

[155] W. D. Cannon, W. E. Garrett, R. E. Hunter, H. J. Sweeney, D. G. Eckhoff, G. T. Nicandri, M. R. Hutchinson, D. D. Johnson, L. J. Bisson, A. Bedi, J. A. Hill, J. L. Koh, and K. D. Reinig, "Improving residency training in arthroscopic knee surgery with use of a virtual-reality simulator," *The Journal of Bone & Joint Surgery*, vol. 96, no. 21, pp. 1798–1806, Nov. 2014.

[156] C. G. I. Alejandro, B. S. Picon, J. V. Martinez, S. R. Bescos, M. F. V. Casique, F. J. A. Hinojosa, J. P. Cuervo, A. S. Gonzalez, L. P. Prez, J. M. Fernandez-Arroyo, G. T. Barros, n. R. Bartolom, J. M. Guillermo, S. B. Beriso, M. J. G. Lorenzo, P. T. Rabasco, J. J. S. M. Lopez, O. D. R. Snchez, and C. A. M. Serrano, "Simulation system for arthroscopic surgery training," U.S. Patent US8 550 821 B2, Oct., 2013.

[157] N. Choudhury, N. Glinas-Phaneuf, S. Delorme, and R. Del Maestro, "Fundamentals of neurosurgery: virtual reality tasks for training and evaluation of technical skills," *World Neurosurgery*, vol. 80, no. 5, pp. e9–e19, Nov. 2013.

[158] S. Lu, Y. Q. Xu, Y. Z. Zhang, Y. B. Li, L. Xie, J. H. Shi, H. Guo, G. P. Chen, and Y. B. Chen, "A novel computer-assisted drill guide template for lumbar pedicle screw placement: a cadaveric and clinical study," *The International Journal of Medical Robotics and Computer Assisted Surgery*, vol. 5, no. 2, pp. 184–191, Jun. 2009.

[159] C. J. Luciano, P. P. Banerjee, J. M. Sorenson, K. T. Foley, S. A. Ansari, S. Rizzi, A. V. Germanwala, L. Kranzler, P. Chittiboina, and B. Z. Roitberg, "Percutaneous spinal fixation simulation with virtual reality and haptics:," *Neurosurgery*, vol. 72, pp. A89–A96, Jan. 2013.

[160] A. Alaraj, F. T. Charbel, D. Birk, M. Tobin, M. Tobin, C. Luciano, P. P. Banerjee, S. Rizzi, J. Sorenson, K. Foley, K. Slavin, and B. Roitberg, "Role of cranial and spinal virtual and augmented reality simulation using immersive touch modules in neurosurgical training," *Neurosurgery*, vol. 72 Suppl 1, pp. 115–123, Jan. 2013.

[161] M. S. Austin, A. R. Vaccaro, B. Brislin, R. Nachwalter, A. S. Hilibrand, and T. J. Albert, "Image-guided spine surgery: a cadaver study comparing conventional open laminoforaminotomy and two image-guided techniques for pedicle screw placement in posterolateral fusion and nonfusion models." *Spine November 15, 2002*, vol. 27, no. 22, pp. 2503–2508, 2002.

[162] A. Sergovich, M. Johnson, and T. D. Wilson, "Explorable three-dimensional digital model of the female pelvis, pelvic contents, and perineum for anatomical education," *Anatomical Sciences Education*, vol. 3, no. 3, 2010.

[163] F. S. Nooruddin and G. Turk, "Simplification and repair of polygonal models using volumetric techniques," *IEEE Transactions on Visualization and Computer Graphics*, vol. 9, pp. 191–205, 2003.

[164] D. Morris, C. Sewell, F. Barbagli, K. Salisbury, N. H. Blevins, and S. Girod, "Visuohaptic simulation of bone surgery for training and evaluation," *IEEE computer graphics and applications*, vol. 26, no. 6, pp. 48–57, Dec. 2006.

[165] D. Li, S. S. Mao, B. Khazai, J. A. Hyder, M. Allison, R. McClelland, I. de Boer, J. J. Carr, M. H. Criqui, Y. Gao, and M. J. Budoff, "Noncontrast cardiac computed tomography image-based vertebral bone mineral density: the multi-ethnic study of atherosclerosis (MESA)," *Academic radiology*, vol. 20, no. 5, pp. 621–627, May 2013.

[166] O. Meruvia-Pastor, M. Xiao, J. Soh, and C. W. Sensen, "Generation of connectivity-preserving surface models of multiple sclerosis lesions," *Studies in Health Technology and Informatics*, vol. 163, pp. 359–365, 2011.

[167] D. Berg, J. Berkley, S. Weghorst, G. Raugi, G. Turkiyyah, M. Ganter, F. Quintanilla, and P. Oppenheimer, "Issues in validation of a dermatologic surgery simulator," *Studies in Health Technology and Informatics*, vol. 81, pp. 60–65, 2001.

[168] A. M. Paisley, P. J. Baldwin, and S. Paterson-Brown, "Validity of surgical simulation for the assessment of operative skill," *British Journal of Surgery*, vol. 88, no. 11, pp. 1525–1532, Nov. 2001.

[169] P. Chiang, J. Zheng, Y. Yu, K. H. Mak, C. K. Chui, and Y. Cai, "A VR simulator for intracardiac intervention," *IEEE Computer Graphics and Applications*, vol. 33, no. 1, pp. 44–57, Jan. 2013.

[170] J. Gasco, A. Patel, J. Ortega-Barnett, D. Branch, S. Desai, Y. F. Kuo, C. Luciano, S. Rizzi, P. Kania, M. Matuyauskas, P. Banerjee, and B. Z. Roitberg, "Virtual reality spine surgery simulation: an empirical study of its usefulness," *Neurological Research*, vol. 36, no. 11, pp. 968–973, May 2014.

Curriculum Vitae

Qi Xing received his Master's Degree of Computer Science from Southwest Jiao Tong University in 2007. His research has focused on the intersection of computer vision and applied machine learning with applications to biomedical image analysis and image interpretation in particular areas of segmentation, registration, reconstruction etc. He has worked in Apple at California as intern in 2018.

PUBLICATIONS

1. **Qi Xing**, Parag chitnis, Siddhartha Sikdar, Jonia Alshiek S. Abbas Shobeiri and Qi Wei, A Multi-stage, Multi-resolution and Multi-volumes of-interest Volume Registration Method Applied to 3D Endovaginal Ultrasound, 2019
2. **Qi Xing**, Victor Huynh, Qi Wei, Thales Guimaraes Parolari, Claudia Maurer-Morelli and Nathalia Peixoto, Zebrafish Larvae Heartbeat Detection from Body Deformation in Low Resolution and Low Frequency video, *Medical & Biological Engineering & Computing*. Jul., 2018
3. Qi Wei, **Qi Xing**, Parag Chitnis, Siddhartha Sikdar, Seyed A. Shobeiri Quantitative analysis of 3D ultrasound images for assessing pelvic floor muscle injury, Ultrasonic Imaging and Tissue Characterization, Arlington, Virgina, Jun. 4-6, 2018
4. **Qi Xing**, Weiwei Zhou, Sang Hoon Yeo, Wilssan Joiner and Qi Wei, Kinematic Measurement and Analysis of Limb Movement during Motor Learning, *American Society of Biomechanics*, Boulder, Colorado, Aug. 8-11, 2017
5. Qi Wei, **Qi Xing**, Connor Strapp, Parag Chitnis, Siddhartha Sikdar, Ghazaleh Rostami and Seyed A. Shobeiri, 3D Ultrasound Imaging of Pelvic Floor Muscle

Injury, *Ultrasonic Imaging Tissue Characterization*, Arlington, Virgina, Jun. 5-7, 2017

6. **Qi Xing**, Siddhartha Sikdar and Qi Wei, Measurement of Extraocular Muscle Deformation Using Ultrasound Imaging, *American Society of Biomechanics*, Raleigh, North Carolina, Aug. 2-5, 2016
7. **Qi Xing**, Yifan Li, Brendan Wiggins, Joseph L. Demer, and Qi Wei, Automatic Segmentation of Extraocular Muscles Using Superpixel and Normalized Cut, *In Proceeding of the 11th International Symposium on Visual Computing*, Las Vegas, Nevada, Dec. 14-16, 2015
8. **Qi Xing**, Jim X. Chen, Jihui Li, Ali Moshirfar, Mark Theiss and Qi Wei, A Real Time Haptic Simulator of Spine Surgeries, *In Proceeding of the 21th ACM Symposium on Virtual Reality Software and Technology*, Beijing, China, Nov. 13-15, 2015
9. **Qi Xing**, Jihui Li, Ali Moshirfar, Jim X. Chen, Mark M. Theiss and Qi Wei, A Physically-based Haptics Simulator for Spine Surgery Simulation, *7th World Congress of Biomechanics*, Boston, Massachusetts, Jul. 6-11, 2014
10. **Qi Xing** and Qi Wei, Human Eyeball Model Reconstruction and Quantitative Analysis, *36th Annual International Conference of the IEEE Engineering in Medicine and Biology Society*, Chicago, Illinois, Aug. 26-30, 2014